Anomalous dispersion refinements in the range of absorption edges

Master's Thesis

as part of the Master's degree in
chemistry at the University of Regensburg

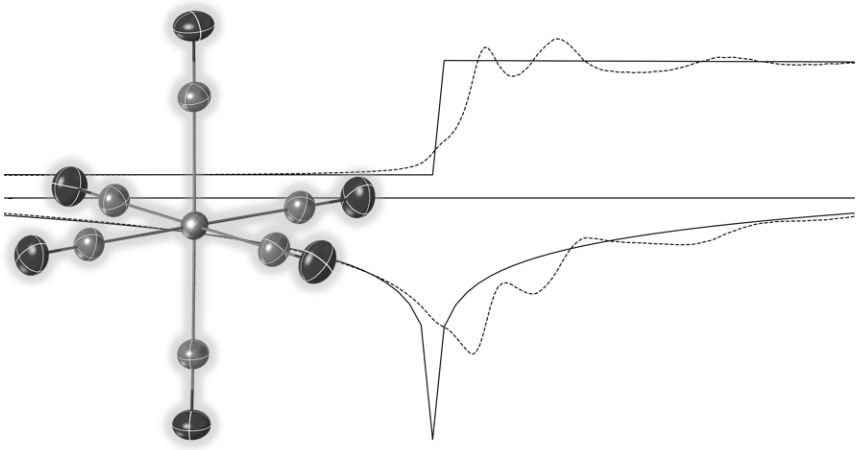

submitted by

Florian Meurer

of

Aschaffenburg

March, 2022

Erstgutachter: Prof. Dr. Nikolaus Korber

Zweitgutachter: Prof. Dr. Manfred Scheer

Danksagung

An dieser Stelle möchte ich meinen Dank an alle Personen richten, die mich direkt oder indirekt beim Anfertigen dieser Arbeit unterstützt haben.

Zuallererst gebührt mein Dank Herrn Professor Korber und Herrn Professor Scheer für das Begutachten dieser Arbeit.

Ganz besonders möchte ich meinem Betreuer, Herrn Doktor Michael Bodensteiner, danken, der diese Arbeit ermöglicht, und mich wissenschaftlich durch die verschiedenen Themen geleitet hat. Für die vielfältigen Erfahrungen, die ich auf dem Weg hierher machen durfte, sowie für die stets konstruktive Zusammenarbeit und Unterstützung Deinerseits möchte ich mich herzlichst bedanken.

Des Weiteren danke ich Herrn Doktor Christoph Hennig für seine exzellente Betreuung der Synchrotron Messungen sowie für wertvolle Einblicke in die Welt der Röntgen-Absorptionsspektroskopie.

Mein besonderer Dank gebührt Herrn Doktor Vedran Vukovic, Herrn Doktor Florian Kleemiß und Herrn Doktor Horst Puschmann für anregende Diskussionen zum Thema und für das Korrekturlesen der Arbeit.

Ich danke Herrn Doktor Oleg Dolomanov für die Umsetzung der Dispersionsverfeinerung in Olex2. Herrn Professor Norbert Peyerimmhoff möchte ich für anregende Diskussionen zu den mathematischen Hintergründen vielmals danken.

Außerdem bin ich meinen Kolleginnen, Frau Birgit Hischa und Frau Sabine Stempfhuber, zu großem Dank verpflichtet. Von euch durfte ich seit meinem ersten Tag in der Röntgenstrukturanalyse der Universität Regensburg viel zur Theorie und noch viel mehr zu den technischen Aspekten der Kristallographie lernen.

Abschließend möchte ich vor allem meinen Eltern, Daniela und Thomas, meinen Großeltern, Mechthild und Franz, sowie meiner Freundin Matilda, von ganzem Herzen danken. Eure Unterstützung, euer offenes Ohr und eure Geduld haben mich stets angetrieben und bekräftigt.

"You're really not going to like it," observed Deep Thought.
"Tell us!"
"All right," said Deep Thought. "The Answer to the Great Question..."
"Yes..!"
"Of Life, the Universe and Everything..." said Deep Thought.
"Yes...!"
"Is..." said Deep Thought, and paused.
"Yes...!!!...?"
"Forty-two," said Deep Thought, with infinite majesty and calm.
- Douglas Adams

Contents

1 Introduction

Since the foundations of X-ray diffraction structure determination were laid by the outstanding pioneering work of Wilhelm Conrad Röntgen, Max von Laue and the father–son duo William Henry and William Lawrence Bragg,[1, 2, 3] the entire field of crystallography has undergone a steady change. In addition to improving theory, algorithms and instrumentation, the method has benefited immensely from the great revolution in data processing.[4]

If we trace the history of modern X-ray crystallography back to the year 1912 with Laue's first experiment, it took another 17 years before the importance of resonant scattering was discovered — known in crystallography as anomalous dispersion. Friedel's law states that, if all atoms scatter identically also with respect to their phases, then the intensities $|F(hkl)|^2$ and $|F(\overline{hkl})|^2$ are identical.[5] Coster *et al.* showed in a remarkable experiment on zincblende (ZnS) that Friedel's law fails when the wavelength of the incident X-rays is close to the absorption edge of, in this case, zinc, but not sulphur.[6] Before this experiment, the intensities were only described as a function of the positions of the atoms contained in the unit cell and the respective type of atom - but not their dependence on a specific wavelength.

In modern single-crystal X-ray crystallography, anomalous dispersion is best known for its influence on the absolute structure: Bijvoet *et al.* described this phe-

nomenon that Friedel's law does not hold when comparing symmetry-equivalent reflections in non-centrosymmetric crystals.[7, 8, 9] By measuring and statistically evaluating the differences of these Friedel mates, one can reliably determine the absolute structure.[10]

Due to the effect of resonant scattering on the overall structure factor, a lot of effort was put towards a direct structure solution method by Pepinksy *et al.*, Ramachandran and Raman as well as Caticha-Ellis.[11, 12, 13, 14] The MAD (multi-wavelength anomalous dispersion) method uses the influence of anomalous dispersion on the structure factor to directly determine the crystal structure.[15] Further, extensive studies conducted by Lieselotte & David Templeton focused on the polarization anisotropy of anomalous dispersion and introduced an improved version of the MAD method.[16] In their work, they also reported on electronic differences at different sites of the same atomic type within the same crystal structure: In Well's salt ($Ce_2[Au(I)Cl_2][Au(III)Cl_4]$), they found differently polarized dispersion parameters for the position of Au(I) and Au(III), respectively.[17]

Einsle *et al.* were the first to show that the dispersion parameters can reliably give insight into electronic properties, which were previously exclusive to spectroscopic methods. This was impressively demonstrated by the oxidation state determination of the central atom in various metalloproteins – most prominently for the cofactor of the enzyme nitrogenase, FeMoco.[18, 19]

Today, anomalous dispersion has very little significance in the crystallography of small molecules except for absolute structure determination. Tabulated values, mostly based on calculations according to Cromer & Libermann are used to correct for resonant scattering.[20] Despite demonstrations by Templeton and Einsle of how much chemical information can be obtained from dispersion values, this information is generally not considered to be relevant in small-molecule X-ray crystallography.

1.1 X-ray diffraction

The first equations as developed by Laue describe the behavior of diffraction within a crystal in a general manner, but the well-known Bragg equation 1.1 serves as a more intuitive picture of this physical process. Unlike Laue's description, where every lattice point serves as scattering origin, Bragg describes the scattering from imaginary, so-called Miller planes, through the lattice points.[2, 3, 21]
Fig. 1.1 shows the condition for constructive interference of photons from such a

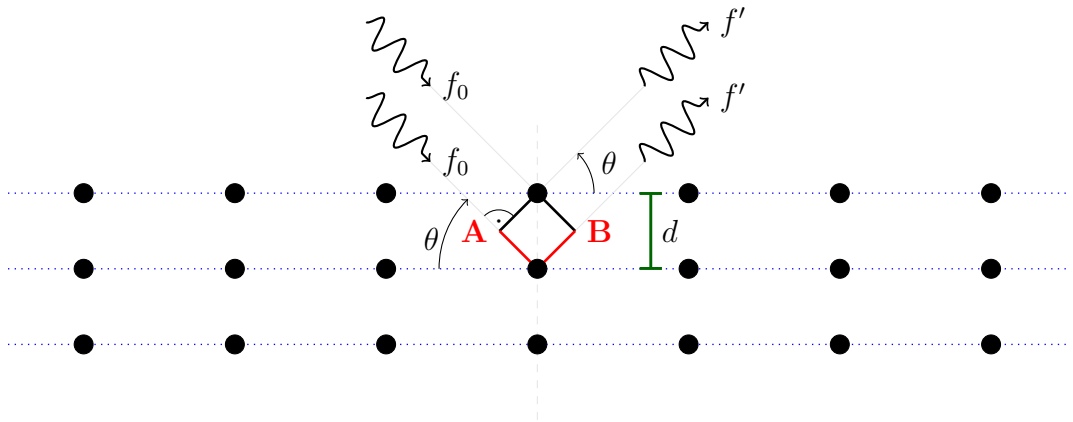

Figure 1.1: Diffraction of X-ray photon waves from a set of Miller planes (blue) with distance d (green)

plane through the crystal's lattice points. At a given wavelength λ, only the angle of incident θ determines, whether constructive interference occurs for a distance d between Miller planes that dissect the unit cell (hkl) times in each cell dimension (abc). This is the case when the incident angle is of such a magnitude that the combined distances **A** and **B** are exactly n times the wavelength. Every other condition, in which the phase is shifted by an $\frac{1}{n^{\text{th}}}$ fragment of the phases of two adjacent mirror planes, it undergoes destructive interference with the photon wave of the $n^{\text{th}}/2$ next mirror plane in the infinite crystal lattice. **A** and **B** can be described as opposite in a right-angled triangle between the normal of the mirror plane and the normal of the photon's path. Their length is dependent on θ and on the distance between the mirror planes by the trigonometric function $d\sin(\theta)$. Adding both together gives rise to the Bragg condition for X-ray diffraction:

$$n\lambda = 2d\sin(\theta) \tag{1.1}$$

Even though this equation tells us precisely at which angle θ one should look for a diffraction spot, it holds no information about the intensity that is expected for this reflection.

1.2 The crystallographic model

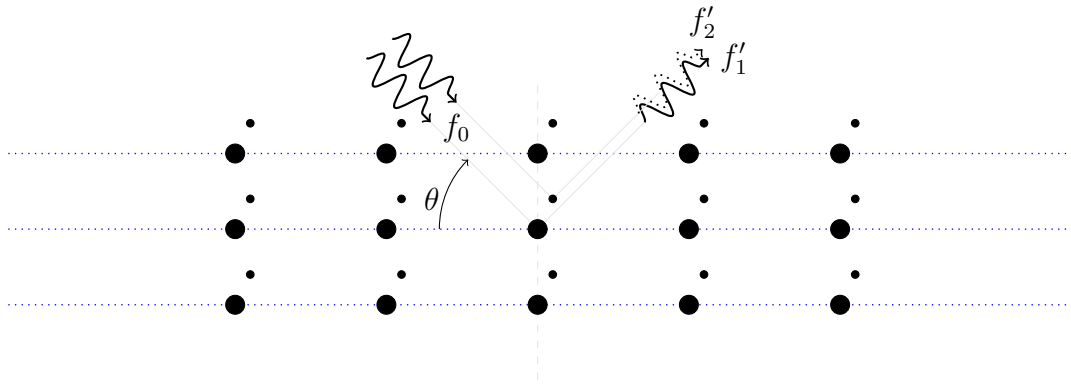

Figure 1.2: Diffraction of X-ray photon waves at multiple centres of scattering

The measured intensities of the Bragg reflections are the basis of structure solution and refinement. Therefore, good-quality observations of reflection intensities are needed, and their quality is assessed through various statistics.

The most important relationship linking the measured intensities of the individual reflections with the crystallographic model are the relations 1.2 and 1.3.[22, 23]

$$F(hkl) = \sum_{n=1}^{\mathrm{N}} f_n \, \mathrm{e}^{2\pi(hkl)\ \mathbf{r}_n} \ \mathrm{T}_n(hkl) \tag{1.2}$$

$$|F(hkl)|^2 \propto I(hkl) \tag{1.3}$$

These equations describe how the structure factor F for a given reflection with Miller indices (hkl) is obtained as a sum over all N atoms in the unit cell, where $\mathbf{r}_n$ denotes the location of the atom n in the unit cell and $\mathbf{T}_n$ its respective Debye-Waller factor with atomic displacement parameters. The absolute square of this complex structure factor is then directly proportional to the measured intensities. After the experimental intensities are scaled, corrected for systematic instrumental errors and absorption, the absolute square of the structure factor is equal to the measured intensities.

The structure factor is the Fourier transform of the electron density distribution. By Fourier synthesis, the respective electron density for this structure is obtained.[24]

$$\rho(hkl) = \frac{1}{V} \sum_{hkl} F(hkl)\ \mathrm{e}^{2\pi(hkl)\ \mathbf{r}_n} \tag{1.4}$$

The quality of the crystallographic model is evaluated by the indicators R_1 and wR_2, which compare the intensities measured and obtained from the current model according to equations 1.5 and 1.6.[†]

$$\mathrm{R}_1 = \frac{\sum |F_{obs}| - |F_{calc}|}{\sum |F_{obs}|} \tag{1.5}$$

$$\mathrm{wR}_2 = \sqrt{\frac{\sum w(|F_{obs}|^2 - |F_{calc}|^2)}{\sum w(|F_{obs}|)^2}} \tag{1.6}$$

There are usually multiple, inhomogeneous locations in the asymmetric unit or lattice points, where radiation is scattered. Since the intensities of measured reflections only depend on the amplitude of the structure factor, the actual phase of the structure factor is unknown due to superposition of the multiple waves of different origin, which however all fulfill the Bragg condition (Fig. 1.2). This is also known as the "phase-problem of crystallography". However, by making certain assumptions on the electron density distribution — that the electron density is positive everywhere and that it belongs to distinct atoms — direct methods are able to solve the phase problem and yield an initial description of electron density maxima.[25, 26]

1.2.1 The independent atom model

The independent atom model is based on considerations about the electron density distribution in crystals by Compton, which treat each atom in the crystal structure as distinct, separate entities.[27] This is also reflected in equation 1.2, as it describes a sum over multiple, separate atoms rather than an integral over the entire electron density of the unit cell. The electron density distribution in this model is described by four Gaussian distributions per atomic position and is based on their radial scattering factors with tabulated fitting coefficients a, b and c unique for each element according to:[28]

$$f(\mathbf{Q}) = \sum_{i=1}^{4} a_i \exp\left[-b_i \left(\frac{\mathbf{Q}}{4\pi}\right)^2\right] + c \tag{1.7}$$

[†]Throughout this work, the terms "(crystallographic) R-factors" are used to refer to these quality indicators to avoid confusion between them and other parameters.

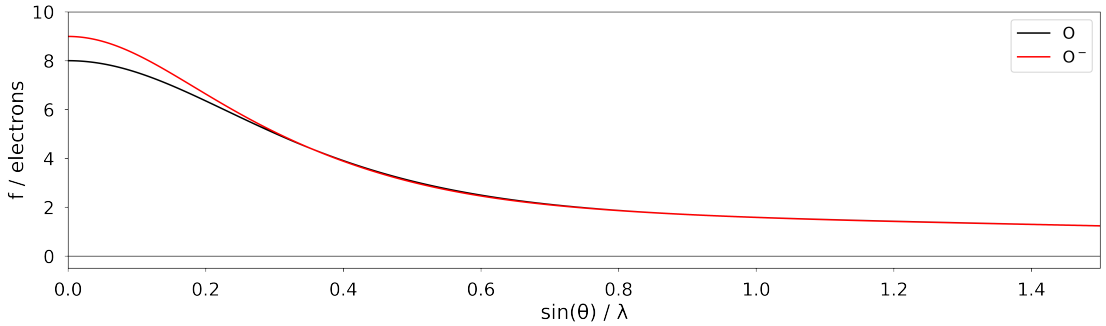

Figure 1.3: Radial scattering factors of O and O^-. Parameters for the radial form factor (equation 1.7) are from the Int. Tables for Crystallography.[29]

where $\mathbf{Q} = 4\pi \sin(\theta)/\lambda$ is the scattering vector, which is proportional to the resolution. Fig. 1.3 depicts an example radial atomic form factors for oxygen as well as monoanionic[†] oxygen. A large difference is observed between the neutral and monoanionic species only at low resolution.

These radial atomic form factors are connected to their spatial electron density distribution by *Fourier* transformation. The radial density in the independent atom model can be expressed as

$$\rho_n(r) = P_{\text{core}}\rho_{\text{core}}(r) + P_{\text{valence}}\rho_{\text{valence}}(r) \tag{1.8}$$

where ρ describes the radial electron density for the core and valence, respectively and P describes the respective population. ρ_{core} describes the averaged, spherical core electron density calculated from theoretical wave-functions of an isolated atom.[30] Similarly, ρ_{valence} describes the electron density of the valence shell normalised to one electron and P_{valence} the number of valence electrons.

In the independent atom model, interactions between the atoms are not considered. However, in order to also investigate the differences resulting from the different magnitudes of the dispersion correction, it is important to use a more precise approach to describe the measured electron density.

[†]The Int. Tables provide no values for the oxide ion (O^{2-})

1.2.2 Improvements to the independent atom model

When considering enhancements to the IAM, there are two important, fundamentally different approaches:

- The **multipolar model** is an experimental approach to introduce non-sphericity into the crystallographic model by parametrisation
- The **Hirshfeld-Atom-Refinement** derives individual atomic scattering factors from a structure-specific wave-function

Multipolar modelling

The approach to multipolar modelling (MM) used almost exclusively today is based on the Hansen-Coppens formalism of 1978.[31] It is a parametric approach to model the measured electron density using separate terms for core and valence populations and asphericity by the multipoles. These multipoles adapt the spherical harmonics from electrostatics and use them to describe the electron density. In their shapes, multipoles closely resemble atomic orbitals. However, while orbitals are based on a chemical understanding and describe the wave-like behavior of an electron in an atom, multipoles describe the electron density contained in a volume of space.

Multipolar modelling preserves the distinction of atomic contribution to the total electron density, but other than the IAM describes also non-spherical distribution. Therefore, the MM may be described as an extension of the independent atom model but follows the same basic principle of division into different, independent atoms. The density of an atom in the multipolar model is described as:

$$\rho_n(\mathbf{r}) = P_{\text{core}}\rho_{\text{core}}(r) + \kappa^3 P_{\text{valence}}\rho_{\text{valence}}(\kappa r) + \sum_{l=0}^{l_{\max}} \kappa'^3 R_l(\kappa' r) \sum_{m=-l}^{l} P_{lm} Y_{lm}(\theta, \phi) \quad (1.9)$$

The molecular electron density is the sum of all atomic densities and consists of three major terms: The first term describes the spherical core density, the second one the spherical valence density and the third term uses Slater-like radial density distributions and spherical harmonics to describe the deformation of valence electron density.[30]

The multipolar model relies on a large variety of parameters to fit the model to the observed charge density. For this purpose, charge density parameters from

a theoretical or experimental database are used. The multipolar contraction parameters κ, κ' as well as P_{valence} and P_{lm}s are then adjusted during the refinement process.

Its advantages are a better fit to the measured electron density and thus an accurate description of a structure with this model. Advantages for the description of anharmonic motion, charge transfer into valence shells as well as topological descriptions as the electrostatic potential and atomic polarization are found for the MM.[32]

Drawbacks of multipolar modelling are tendencies to over-fit the model to the available data and the enormous effort that is involved in modelling even the simplest of inorganic compounds. A useful MM refinement also requires high-quality data to a very high resolution to be able to distinguish multipoles and atomic displacement parameters as well as high redundancy.[30]

Hirshfeld atom refinement

The Hirshfeld atom refinement (HAR) is an *ab-initio* method.[33] It was established by Dittrich and Jayatilaka in 2008 and uses only the geometry of a structure from an arbitrary model (e.g. the IAM) and calculates a molecular wave-function with this input geometry.[33, 34] Using either Hartree-Fock, wave-function based Density Function Theory (DFT) or any different quantum computational method, a molecular wave-function is calculated.[35, 36, 37] This wave-function has to converge to a minimum in the self-consistent-field (SCF) iterative procedure.[38] The electron density distribution as described by the level of theory of the quantum mechanical computations is then obtained as the absolute square of the wave-function. The density is subsequently subdivided into atomic densities according to the Hirshfeld stockholder partitioning.[39] Based on these atomic densities new atomic form factors are calculated, which are then used in the standard refinement process, with subsequently updated parameters like atomic positions and anisotropic displacement parameters. The procedure is then performed iteratively with a new geometry until all parameters of the crystallographic model are converged.[40]

HAR adjusts the atomic form factor f_0 and describes the scattering power directionally. This way, non-spherical electron density described in the wave-function is taken into account and chemical bonds and lone pairs are modelled at the level of theory that was used in the wave-function calculation.

Advantages of HAR are its theoretical approach relying on “first principles” only and therefore its it is robust towards over-fitting. After all, the method only

considers the current crystallographic model with respect to the atomic positions, but not the experimental observations. The anisotropic description of hydrogen atoms and generally strongly improved X-H distances are possible by the application of HAR. Also, as the method requires a wave-function to be calculated, this wave-function can be used to describe the quantum chemical properties of this compound.

The primary issue with the method is the large computational effort that goes into the wave-function calculation. While this was a problem historically, modern computational advances and comfortable implementations in standard crystallographic software (especially `NoSpherA2`[41] for `Olex2`[42]) make HAR a very fast and easily applicable method.

1.3 Anomalous dispersion

In contrast to the phase shift of the incident radiation caused by different atomic positions (Fig. 1.2), the dispersion correction adjusts the atomic form factor for the phase shift that is *not* caused by atomic positions. Different resonance frequencies for the different atom types lead to the failure of Friedel's law. This phenomenon and the resulting difference in structure factors and intensities is called anomalous dispersion.[†] The reason for this phase-shift is resonant photon-electron scattering. The contribution of resonant scattering is mostly low as the excitation energy is usually far from the resonance frequency of the electron scatterers in each electron shell. However, when the excitation energy gets close to a resonance frequency, energy is "lost" for Bragg scattering as is exciting electronic modes rather than it is scattered elastically. An absorption edge is reached, where this effect becomes maximal.

The heavier an atom is, the higher in energy are its resonance energies from higher binding energies for the innermost shells, and the shorter is the wavelength of the corresponding absorption edge. If an emission wavelength of an anode material is slightly shorter than the absorption edge wavelength of an element, then strong resonant scattering and strong absorption is observed. Tab. 1.1 shows usual X-ray anode materials with Cr being the lightest and therefore exhibiting the longest excitation wavelength. Subsequently, significant resonant scattering

[†]Throughout this work, in the interest of linguistic diversity, the terms "anomalous dispersion parameters", "dispersion parameters", "dispersion correction" and "(anomalous) dispersion values" were used synonymously. When these terms are used, they mean the values of the parameters that correct the elastic atomic form factor for resonance effects.

Element	Absorption edges / Å				Emission lines / Å	
	K	L_1	L_2	L_3	K_α	K_β
24-Cr	2.07	17.8	21.2	21.6	2.29	2.09
26-Fe	1.74	14.7	17.2	17.5	1.94	1.76
27-Co	1.61	13.4	15.6	15.9	1.79	1.61
28-Ni	1.49	12.3	14.3	14.5	1.66	1.50
29-Cu	1.38	11.3	13.0	13.3	1.54	1.39
31-Ga	1.20	9.54	10.8	11.1	1.34	1.21
42-Mo	0.619	4.33	4.72	4.92	0.711	0.632
47-Ag	0.486	3.26	3.52	3.70	0.562	0.497
79-Au	0.154	0.834	0.903	1.04	0.183	0.159
80-Hg	0.149	0.825	0.873	1.01	0.177	0.154

Table 1.1: Examples for K and L absorption edges and resulting Kα and Kβ emission lines. Values calculated from references [43, 44].

effects are only observed for heavier elements in X-ray diffraction experiments. For example, Co strongly absorbs Cu Kα radiation, while Ni is absorbing Cu Kβ.

The connection between resonant scattering and absorption can be explained by a classical approach to the dipole oscillator according to R. J. James and Caticha-Ellis provides a comprehensive insight into anomalous dispersion.[44, 45]

A dipole scattering factor is described as:

$$f = \frac{\omega^2}{\omega^2 - \omega_s^2 - ik\omega} = f' + if'' \tag{1.10}$$

where ω is the excitation frequency of a photon, ω_s the oscillation frequency of an electron and k the damping factor. f' and f'' are the real and imaginary part of the scattering factor, respectively. The refractive index n is complex for a medium containing N dipoles per unit volume and can be written as

$$n = 1 - \frac{2\pi N e^2}{m_e \omega^2} f = 1 - \alpha - i\beta \tag{1.11}$$

where e is the elementary charge, m_e the mass of an electron and α and β the real and imaginary part of the refractive index. The absorption results from the complexity of n – especially, when ω approaches ω_s. The linear absorption coefficient can therefore be expressed as a function of f'':

$$\mu = \frac{4\pi\beta}{\lambda} = \frac{2\omega\beta}{c} = \frac{4\pi N e^2}{mc\omega} f''(\omega) \tag{1.12}$$

This relationship is very important as it shows a linear correlation between the absorption coefficient μ and the imaginary part of the anomalous dispersion correction f''. Hence, how f'' can be extracted from experimental data by X-ray absorption spectroscopy (XAS).

Using the Kramers-Kronig relationship, one can calculate f' directly from f'' using the Cauchy integral around the pole $\omega' = \omega$

$$f'(\omega) = \frac{2}{\pi} \int_{\omega_K}^{\infty} \frac{\omega' f''(\omega')}{\omega^2 - \omega'^2} \, \mathrm{d}\omega' \tag{1.13}$$

where ω is the excitation frequency and $\omega' \rightarrow \frac{f''(\omega')}{\omega - \omega'}$ the running variable of the integral.[46] This way, both f'' and f' can be extracted from an absorption spectrum for a given element near its absorption edge.

1.3.1 Dispersion correction in X-ray crystallography

To account for these resonant effects, each atomic form factor in the crystallographic model is corrected according to equation 1.14.

$$f_n = f_{n,0} + f' + if'' \tag{1.14}$$

$f_{n,0}$ denotes the ideal, the fully elastic atomic form factor of the atom n in the unit cell, and f' and f'' are the real and imaginary parts of the dispersion correction. This formalism closely follows the description of the refractive index. Indeed anomalous dispersion can be explained as to how "prism-like" atoms behave at certain energies for X-rays.

The calculation of these resonant effects depends on the oscillator strengths, which is a measure for the probability of absorption in a transition between two defined energy levels. Multiple ways to calculate the correction from the respective oscillator strengths have been established: Hönl as well as Eisenlohr and Müller derived the oscillator strengths from hydrogen-like eigenfunctions.[47, 48, 49] Parratt and Heampstead relied on semi-empirical relations between the photoelectric cross-section and the dispersion parameters.[50] Cromer & Libermann calculated f' and f'' using Slater-Dirac wave-functions. [51]

Since the computing power was limited, pre-calculated tables were created. These were mostly based on the approach by Cromer & Libermann and are still used today. These dispersion corrections adjust each atomic form factor in equation 1.2 by the correctional terms stated in equation 1.14.

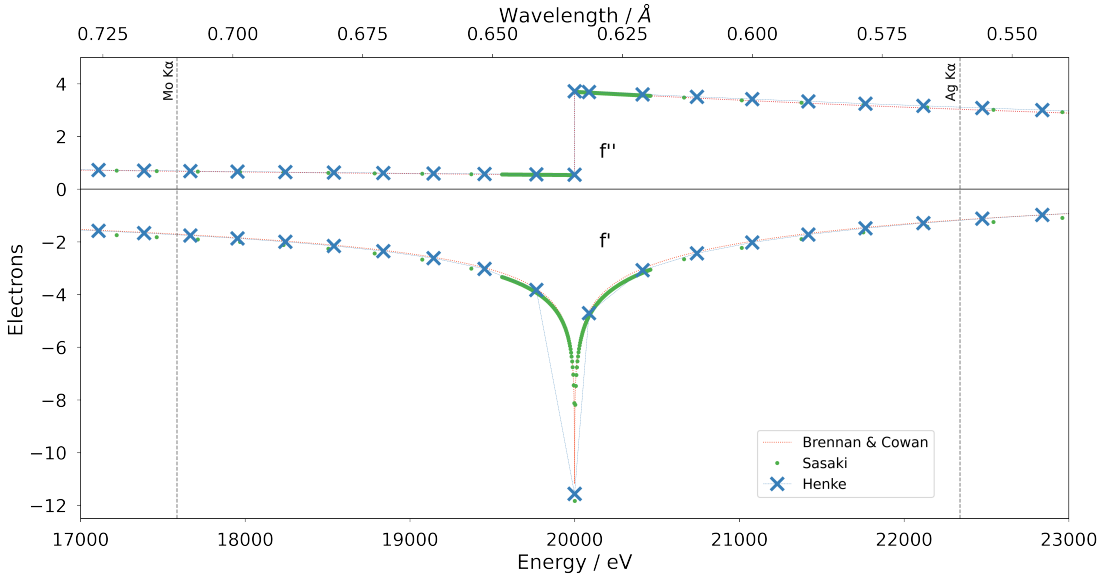

Figure 1.4: Tabulated dispersion correction values according to Brennan & Cowan[52], Sasaki[53] and Henke[54] for molybdenum between 17,000 eV and 23,000 eV.

The tables by Sasaki[53], Henke[54] and the table by Creagh *et al.*[55], which is found in the International Tables Vol. C as well as direct calculations from Brennan & Cowan[52] are commonly used to correct for anomalous dispersion in crystallographic software. These tables mostly differ in their coarseness of the values for f' and f'' at distinct energy values for each element. While Sasaki's values are particularly finely described at energies close to the absorption edges, the Henke table contains coarse, equidistant entries. The most coarsely tabulated values are found in the International Tables where only dispersion parameters for the common X-ray source anode materials can be found for each element. Therefore, this source for dispersion correction is not further considered in this work. Contrary to the three tables, the program by Brennan & Cowan calculates the exact dispersion values for a given element at a given energy. It is generally in good agreement with the data from Sasaki.

In Fig. 1.4 the progression of the tabulated dispersion correction is shown. f' possesses a small, negative value far from the absorption edges and theoretically approaches negative infinity asymptotically at the absorption edge. At energies above the absorption edge, the real part f' approaches zero asymptotically, but

even reach small values above zero far above an absorption edge. If the term reaches a positive value, resonance scattering seemingly amplifies the elastic signal observed in Bragg reflections rather than dampen it.

Contrary, the imaginary part f'' is always positive and decreases steadily to zero when approaching an absorption edge. At the edge f'' jumps to a higher value, then decreases again. Hereby, the decay behavior of f'' is exponentially. This progression is consistent with the direct proportionality to the linear absorption coefficient. The absorption of an element decreases with higher energy as the quantum efficiency of resonant modes of lower energy decreases. At the absorption edge, a resonant mode of higher energy can be excited leading to an instantaneous increase in f'' and therefore absorption.

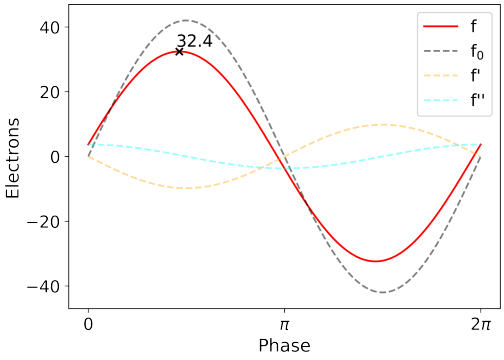

Figure 1.5: Visualisation of the phase-shifted dispersion correction for $f(000)$ of molybdenum at 20,000 eV

Fig. 1.5 shows how f' and f'' can be interpreted as in-phase and phase-shifted contributions to the atomic form factor. In the case of molybdenum at its K absorption edge at 20,000 eV this effect is especially drastic. The real part of the dispersion correction f' is in-phase with f_0 but exhibits the opposite amplitude and therefore directly subtracts from the actual scattering power. The imaginary part f'' is shifted by $\pi/2$ with respect to f_0 and therefore corrects the number of electrons phase dependently. The amplitude of f_0 for the reflection (000) for molybdenum is energy independent and corresponds only to the atomic number 42. Dispersion correction terms are both atom-type *and* energy dependent. At 20,000 eV they have values of –9.80 electrons for f' and 3.70 electrons for f'' for molybdenum according to Brennan & Cowan.[52] In total, the atomic form-factor is reduced from 42 to 32.4 electrons at the K absorption edge. This means that in a diffraction experiment performed at exactly 20,000 eV ($\lambda = 0.61992$ Å) for any reflection (hkl), molybdenum contributes up to 32.4 electrons as atomic form factor to the overall structure factor, as opposed to 42 electrons assuming pure elastic Thomson scattering. This can have a huge effect on the overall structure factor, especially when molybdenum is the heaviest atom present and therefore contributes the most to the structure factors.

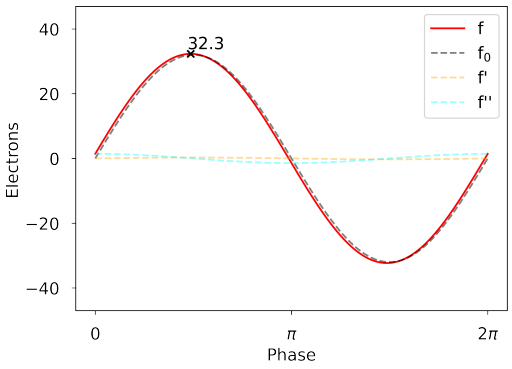

Figure 1.6: Visualisation of the phase-shifted dispersion correction for $f(000)$ of germanium at 20,000 eV

On the contrary, when a different element, germanium, is inspected at the same energy, the dispersion terms are comparably small. Fig. 1.6 shows how little the effect of resonant scattering is, when the excitation energy is far from an absorption edge. In this case, germanium with atomic number 32 has tabulated dispersion values of 0.279 and 1.43 electrons for f' and f'', respectively.[52] This results in an almost identical value for f of germanium and molybdenum at 20,000 eV of about 32 electrons for $f(000)$. From this perspective, it appears that molybdenum and germanium are in fact indistinguishable in a diffraction experiment performed at this wavelength using tabulated dispersion correction.

However, this is not exactly the case: Since the amplitudes mentioned above are only the maximum contribution of a single reflection to the structure factor but are completely neglecting the radial distribution of the atomic form factor.

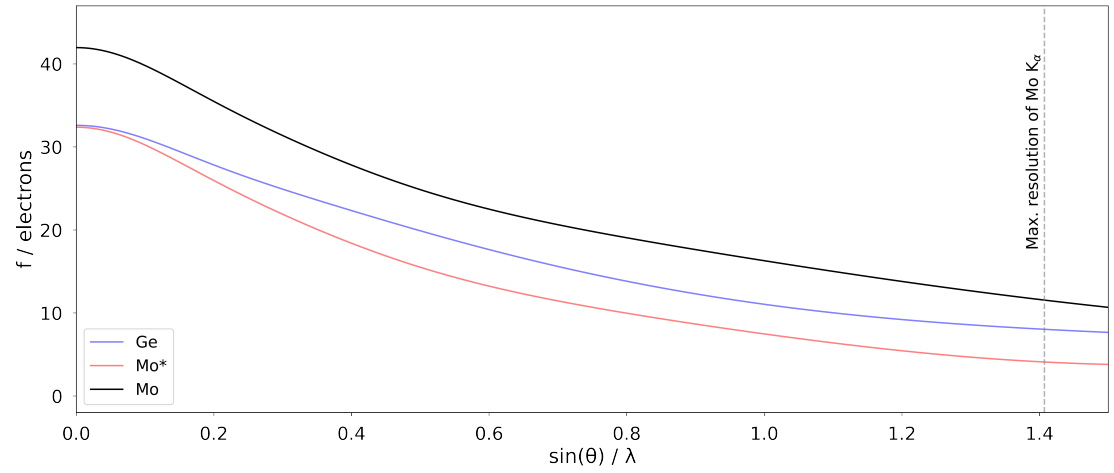

Figure 1.7: Radial atomic form factors before (black) and after (red) dispersion correction of Mo (*, according to Brennan & Cowan) compared to the dispersion corrected atomic form factor of germanium (blue) at 20,000 eV.[29]

Fig. 1.7 compares the radial atomic form factors of molybdenum and germanium. It is obvious that despite an almost identical value at very low resolution, the progression of the radial atomic form factor is vastly different. The resolution dependence of the anomalous dispersion correction depends only on the absolute values of f' and f'' and proceeds according to the modulus of a complex number as described in equation 1.15:

$$f_n(R) = \sqrt{(f_{n,0}(R) + f')^2 + (f'')^2} \tag{1.15}$$

In summary, the dispersion correction can have an enormous effect onto the crystallographic model, as resonant scattering influences the effective, measured electron density and therefore the intensities of the reflections observed. Especially in the energetic vicinity of absorption edges the amount of correction has immense importance for the agreement of experimental observations and crystallographic models. As tabulated dispersion values are pre-calculated for atoms in their elemental form, they do not consider the individual electronic configuration found in chemical compounds. However, there are methods to describe the particular effects of the chemical environment of an atom spectroscopically.

1.4 X-ray absorption spectroscopy

The physical basis of X-ray absorption spectroscopy (XAS) is the photoelectric effect, which describes an incident photon being absorbed by an electron in such a way that the excited electron is expelled. This effect occurs with the highest probability at the corresponding absorption edge for each atom. The absorbance A or transmission T of a material are functions of the relation between the initial flux ϕ_0, the output flux ϕ, the linear absorption coefficient μ, its thickness x and the frequency of the incoming radiation ω.[56]

$$A(\omega) = -\log_{10} T(\omega) = -\log_{10} \frac{\phi}{\phi_0} = \mu(\omega)x \tag{1.16}$$

The standard energy range for XAS is between 1–40 keV. Hence, typical wavelengths for X-ray absorption experiments are within the range of 0.3–12 Å.[57]

A spectrum is obtained by irradiation of the sample compound over the energetic range of interest. Ideally, the radiation source for these experiment is a synchrotron particle accelerator, which produces a continuous X-ray spectrum with a high photon flux. A typical setup for a beamline to perform XAS experiments is shown in Fig. 1.8.

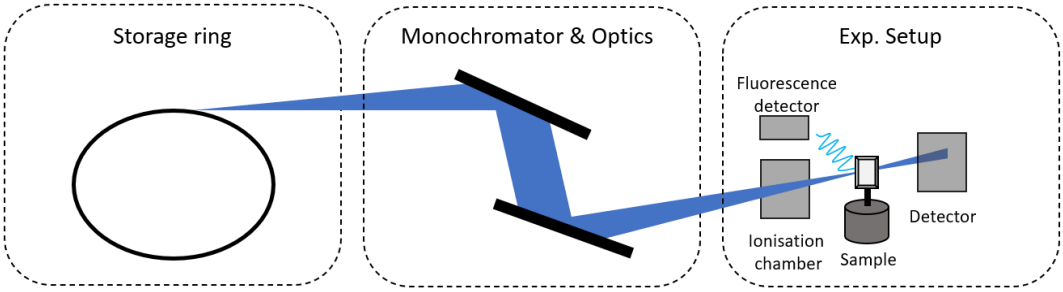

Figure 1.8: Setup for a beamline at a synchrotron storage ring to perform XAS experiments.

Besides measuring the transmission directly, it is common to measure the fluorescence of a sample containing heavier elements. The information on spectral features available from XAS depends on the energy range that is being scanned. They are subject to mainly two different types of X-ray absorption experiments.

1.4.1 XANES

X-ray absorption near edge spectroscopy (XANES) observes the absorbance below the absorption edge and up to 30–50 eV above. The most widely applied evaluation in XANES is about the electronic configuration of the atom of interest, e.g. its oxidation state. Fig. 1.9 shows the energies of the K, L_{III} and M_V absorption edges with increasing atomic number Z as well as the absorption edges for molybdenum and the respective electronic ground states corresponding to these absorption edges.

Note that the excitations follow the selection rules:

$$\Delta l = \pm 1;\ \Delta s = 0;\ \Delta j \pm 1, 0;\ \Delta m = 0. \tag{1.17}$$

The highest excitation level in terms of energy is the K edge, corresponding to an excitation of a 1s electron. L and M edges are corresponding to the 2s / 2p and 3s / 3d excitations, respectively. XANES mainly focuses on the K and L absorption edges.[56] The K edge is mostly used for 3d and 4d transition metals, like Fe, Co, Mo, Pd or Ru, while the L edge is subject to the investigation of 5d and 6p elements (e.g. Ir, Pt, Au or Bi).[59] Excitation occurs when core electrons are elevated into unoccupied states or into the continuum, which corresponds to ionization.

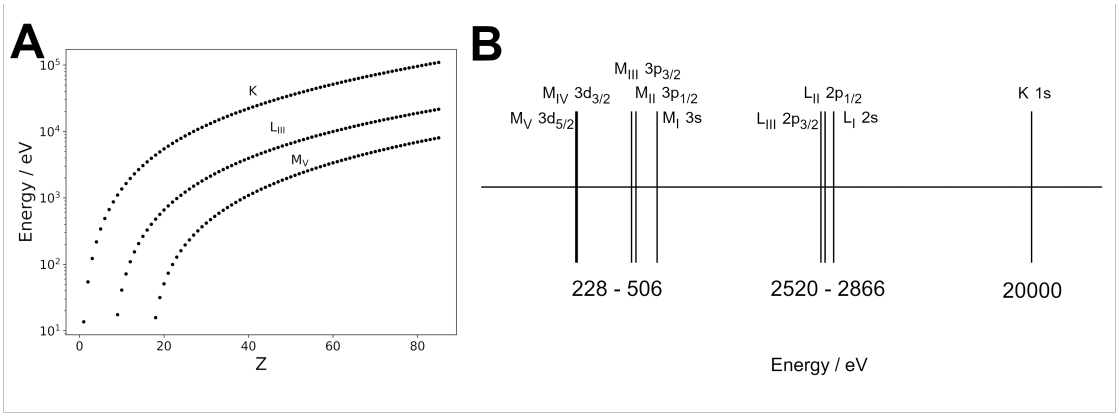

Figure 1.9: X-ray ionization energies for the K, L_{III} and M_V levels as a function of the atomic number Z (**A**) from NIST [58]. Ionization levels from K to M_V at their respective energy and ground state (**B**).[43] Logarithmic scales are applied for the energy axes.

Features of interest for XANES are the absorption edge as well as the pre-edge. For 3d metals, the pre-edge is mostly governed by the spin forbidden transition in the lowest unoccupied orbital (1s $\rightarrow$ 3d). For 4d metals, however, the situation is more complex and the various transitions giving rise to the pre-edge in these compounds are the subject of ongoing research.[60]

The exact position of an absorption edge is dependent on the definition. The maximum of the derivative of the spectrum is the most common convention to locate the edge energy. By comparison to different compounds containing the same element, a shift in absorption edge corresponding to a shift in oxidation state. The shift per charge into oxidation state is usually in the range of a few eV with a higher oxidation state is shifting the absorption edge to a higher excitation energy.[57] This increase originates from a higher electrostatic force on the atom's electrons due to a higher effective core charge.

1.4.2 EXAFS

The extended X-ray absorption fine structure (EXAFS) investigates the spectral range above the XANES region to an energy of around 1 keV above it.[56] It contains information on local structural features such as coordination numbers and interatomic distances.[61] Fig. 1.10 shows the EXAFS and XANES region at the example of a typical K absorption edge spectrum.

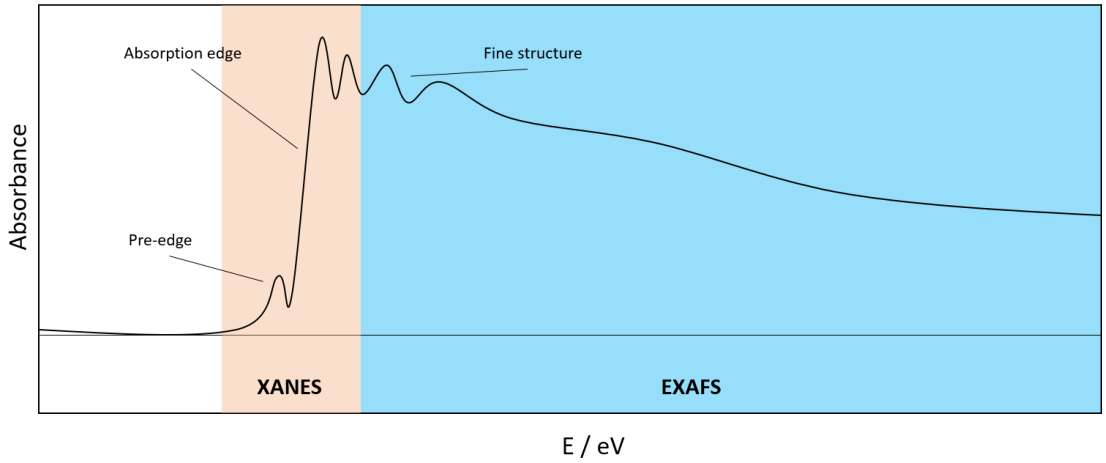

Figure 1.10: Schematic X-ray absorption spectrum with spectral features and XANES, EXAFS region highlighted, respectively.

EXAFS relies on the absorption of photons by an atom at an energy above the absorption edge. An electron in the atom's core is subsequently excited in such a way that it gets ejected from the atom. The kinetic energy of this photo-electron results from the difference between the photon energy and the core binding energy.[62] The photo-electron is then scattered by a neighboring atom, resulting in oscillated modulations of the absorption, observable in the absorption spectrum. It depends only on the photon energy and distance of atoms. Therefore, local information is obtained about the vicinity of an absorbing atom without the long-range order requirements of diffraction experiments. Hence, structural information of non-crystalline systems is also accessible through this method.

To consider the importance of X-ray absorption spectroscopy for dispersion parameters in X-ray diffraction methods, the following aspects are important: The imaginary part of the dispersion parameters f'' is directly related to the absorbance measured in X-ray absorption spectra. The real part f' can be calculated from f''. The exact position of an absorption edge depends on the chemical environment and most prominently the oxidation state of an atom. All tables for dispersion correction are calculated for elemental data and are validated against experimental spectra of the corresponding element. It is sensible to assume a significant shift of these absorption edges when these elements are embedded in a chemical environment. EXAFS experiments on the other hand show that up to 1 keV above an absorption edge significant oscillations according to local structural features can

be observed.

Both of these features are not and cannot be considered in any of the tabulated dispersion corrections as they have to be as general as possible. However, it is sensible to assume that dispersion correction is unique to the actual structure at hand – if the data set was measured in the vicinity of an absorption edge, which requires synchrotron radiation.

1.5 The least-squares refinement

From an analytical point of view, single crystal X-ray diffraction is an over-determined analytical method, which means that there are usually many more data points than parameters. Therefore, it is important to achieve a high precision of the collected data. The intensities measured in X-ray crystallography contain both random and systematic errors. Systematic errors have to be either corrected during the data reduction process or modelled by parametrisation. Random errors are reflected in the standard uncertainties of the experimental data obtained during integration and merging. A weighting scheme is employed to favour more accurately measured data over weaker data in the least-squares refinement.

Generally, the least-squares method assumes errors in the form of a Gaussian distribution. The method employs the equation for the structure factor (Eq. 1.14) to calculate model intensities which are optimized against the measured data. As this equation is very complex for even a simple molecule and therefore hard to illustrate, an example is given for a simple, linear least-squares problem.

1.5.1 Linear least-squares fitting

For a data-generating, two parameter function of first degree and five observations of the type $y = ax + b$ with the unknown parameters a,b and with Gaussian noise on the observations x, y, we find a situation similar to Fig. 1.11 A.

For each pair of observation, we can formulate a linear equation. This implies five separate linear equations of the form:

$$\begin{pmatrix} x_1 \\ x_2 \\ x_3 \\ x_4 \\ x_5 \end{pmatrix} = \begin{pmatrix} y_1 \\ y_2 \\ y_3 \\ y_4 \\ y_5 \end{pmatrix} \begin{pmatrix} a \\ b \end{pmatrix} \tag{1.18}$$

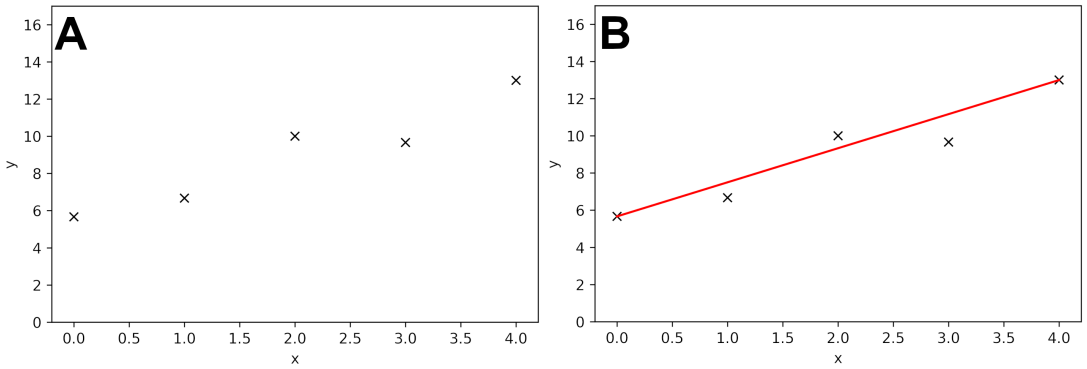

Figure 1.11: Data points generated with according to the formula $2x + 4.5$ with random noise added (**A**) and initial fit (**B**)

At best, two linear equations can be satisfied simultaneously arbitrarily choosing two observations (e.g. x_1, y_1 and x_5, y_5) to solve for values for a and b. The result is then an initial guess to the optimized fit, shown in Fig. 1.11 B.
The problem is that for every pair of observations the parameters a and b are different, but they are required to fit the data in the best possible way. The least-squares algorithm allows to obtain the smallest average squared deviation between the fit and the data. To do this, it is required to minimize equation 1.19:

$$S = \sum_i w_i(a_i x_i + b - y_i))^2 \tag{1.19}$$

This function (with weights w for each observation) is minimal when its partial derivatives with respect to each parameter are zero:

$$\frac{\partial S}{\partial a} = 2\sum_i x_i(ax_i + b - y_i) = 0 \tag{1.20}$$

$$\frac{\partial S}{\partial b} = 2\sum_i (ax_i + b - y_i) = 0 \tag{1.21}$$

Rearrangement gives two linear equations which are solveable for a and b for N observations:

$$a\sum_i^N x_i^2 + b\sum_i^N x_i = \sum_i^N x_i y_i \tag{1.22}$$

$$a\sum_{i}^{N} x_i + bN = \sum_{i}^{N} y_i \tag{1.23}$$

This way, the model is optimised to fit the parameters to the observations.

1.5.2 Least-squares in crystallography

For each atom in the asymmetric unit, the crystallographic independent atom model contains multiple parameters. These are the atom's coordinates x, y, z as well as its anisotropic displacement parameters U_{11}, U_{22}, U_{33}, U_{12}, U_{13} and U_{23}. Therefore, there are a total of nine parameters per atom if it is refined anisotropically. Some crystallographic programs also include the overall scaling factor directly into the least-squares refinement cycle.

The function that is minimized for crystallographic models is however similar to the linear example above:

$$S = \sum_{hkl} w_{hkl}(|F_{obs}(hkl)| - |F_{calc}(hkl)|)^2 \tag{1.24}$$

If we now introduce new parameters in the crystallographic model (f' and f'') to the least-squares algorithm, the refinement will approach a minimum of all $|F_{obs}|^2 - |F_{calc}|^2$ differences with respect to these parameters. It is very important to consider the resulting variance-covariance matrix and the resulting correlation matrix to check for unjustified correlations, especially with respect to newly introduced parameters.

2

Aims and objectives

This study aims to obtain anomalous dispersion parameters purely from diffraction data and compare them to the spectroscopic properties for the compounds under investigation. Because of the direct correlation between absorbance and the imaginary part of the dispersion correction f'', it is possible to extract f'' from X-ray absorption experiments. Using the Kramers-Kronig relation as a mathematical technique, the real part of the complex dispersion correction f' can be calculated from f''.

As a first approach, X-ray absorption spectra of small molecular compounds are measured and their spectral features are evaluated. The recorded spectra provide information about the electronic properties via their spectral features. These features are the pre-edge, the absorption edge, and the fine structure above the absorption edge. Differences in the spectral features between similar compounds give insight into the effects of chemical differences, for example the behavior of an interchanged ligand or different formal oxidation states.

The second approach to estimate values for these anomalous dispersion parameters is by X-ray diffraction experiments at energies, where spectral features have been determined. The values for dispersion correction in X-ray crystallography are generally interpolated from tabulated values and used as constants throughout the structure determination process. By introducing f' and f'' as free parame-

ters during the least-squares algorithm these parameters can be adjusted to values that yield the best least-squares fit for the model. The resulting quality parameters for the crystallographic models for refined and tabulated dispersion values give insight into how these perform at various energies near an absorption edge. Comparison of the values for f' and f'' from spectroscopy and diffraction experiments reveals to what extent the diffraction parameters follow the values obtained from spectroscopy. The method of dispersion refinement is tested for robustness and whether the additional parameters introduce unreasonable correlations in the crystallographic models. An investigation on "wrong atom type models" provides insight into how the method can potentially be exploited.

Differences in the resulting dispersion parameters for modified compounds are analysed. This shows, how varying dispersion parameters can indicate electronic and chemical differences between these compounds. Multipolar modelling gives insight into the experimental charge density distribution and thus the atomic charge distribution at the positions of interest. The method of refining dispersion parameters is then tested for data sets of literature compounds with similar, but not identical chemical contexts.

For this study, molybdenum has been chosen as the primary element for the example compounds. Molybdenum has its K absorption edge at exactly 20,000 eV and is readily available in different compounds of varying stability. Since a synchrotron beamline with precisely tunable optics is required for both X-ray diffraction and X-ray spectroscopy experiments, the Rossendorf beamline (ROBL), BM20, at the European Synchrotron Radiation Facility (ESRF) in Grenoble, France was chosen for this demanding task.[63] The special setup of ROBL allows for high-throughput measurements of both diffraction and spectroscopy experiments in an energy range around 20,000 eV. This way, the spectroscopic, and diffraction data can both be obtained from single crystals in a comparable experimental setup.

$Mo(CO)_6$ (molybdenum hexacarbonyle) is fairly stable at air and room temperature as well as easy to crystallize. It serves as the central compound to this study and is investigated using diffraction and spectroscopic experiments. $(MeCN)_3Mo(CO)_3$ (trisacetonitrile molybdenum tricarbonyle, MeCN = CH_3CN) provides a slight modification of $Mo(CO)_6$ in the same formal oxidation state and is therefore compared to $Mo(CO)_6$.

Spectroscopic studies were carried out on TMEDA(MeCN)$Mo(CO)_3$ (acetonitrile tetramethylethylendiamine molybdenum tricarbonyle) as well as (TACN)MoO_3 (1,4,7-triazocyclononane molybdenum(VI) oxide).

3

Results and discussion

3.1 Synthesis of sample compounds

3.1.1 Molybdenumhexacarbonyl – $Mo(CO)_6$

Commercially available $Mo(CO)_6$ (Fig. 3.1 **a**) was crystallised by sublimation. This way, approximately 0.10 x 0.10 x 0.10 mm^3 clear, colourless blocks of $Mo(CO)_6$ suitable for diffraction and spectroscopic experiments were obtained.

3.1.2 Tris(acetonitrile) tricarbonylmolybdenum – $(MeCN)_3Mo(CO)_3\times(MeCN)$

1 g of $Mo(CO)_6$ was left stirring at re-flux under exclusion of air and moisture over night in 50 mL of acetonitrile. Clear, orange-brown crystals of $(MeCN)_3Mo(CO)_3\times$ (MeCN) (Fig. 3.1 **b**) were obtained after storage for three hours at –4°C suitable for diffraction and spectroscopic experiments.

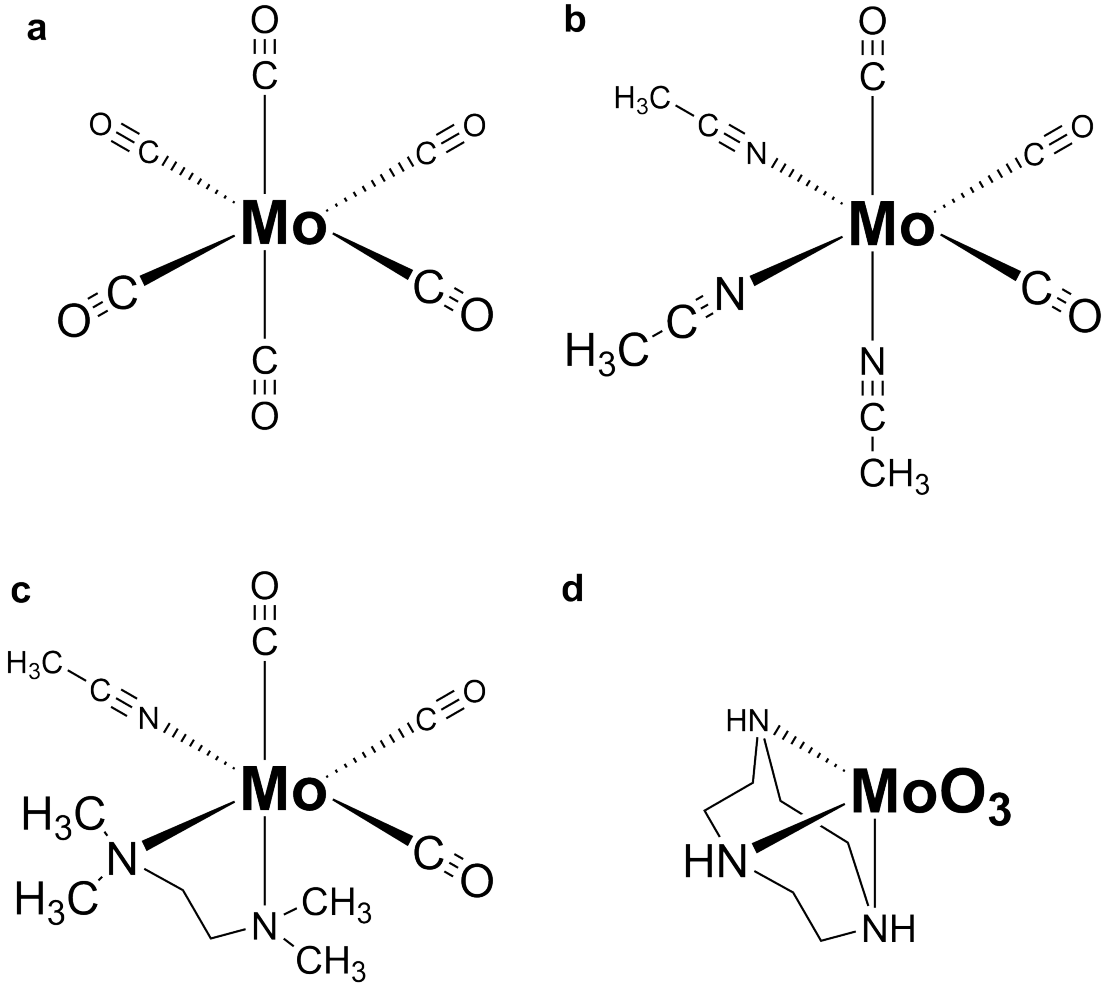

Figure 3.1: The four compounds which are subject to this work

3.1.3 1,4,7-Triazocyclononane molybdenum(VI)oxide – (TACN)MoO_3

1,4,7-triazacyclononane was added to a suspension of 1 g of MoO_3 in 25 mL of water with stirring and a clear, colourless solution was obtained upon heating to 75°C. This solution was cooled to room temperature and added to 100 mL of an ethanol-diethylether mixture (1:1). (TACN)MoO_3 (Fig. 3.1 **c**) formed as a white precipitate, was washed with ethanol and recrystallized from a water ethanol mixture over three weeks at 7°C.

3.1.4 Acetonitrile-tetramethylethylendiamine molybdenumtricarbonyle – (TMEDA)(MeCN)$Mo(CO)_3$

(TMEDA)$Mo(CO)_4$ was dissolved in 40 mL of acetonitrile. Storing at –9°C over several weeks golden-brown crystals of (TMEDA)(MeCN)$Mo(CO)_3$ (Fig. 3.1 **d**) were obtained suitable for spectroscopic experiments.

3.2 X-ray absorption spectra

3.2.1 General procedure

Each measurement was performed within the range of 19,900 eV – 20,100 eV. The energy was calibrated against the first inflection point of a K absorption edge spectrum of molybdenum metal foil at 20,000eV. All spectra were normalised so that the absorption was zero at 19,900 eV and converged to one at 20,100 eV.

The offset determined between the machine's calibrated energy and the edge determined from the maxima of the derivative of the absorbance spectrum was used to adjust the samples' X-ray absorption spectra. The deviations between the calibration metal foil spectrum and the sample spectra over three separate visits at the ESRF were in the range of 0.1 eV – 2.0 eV.

All spectra, except for the calibration spectrum, were performed on single crystals, but on different single crystals than the X-ray diffraction experiments were performed. This was because the quality of the crystals is of more importance for the diffraction experiments than it is for the spectroscopic experiments and therefore the diffraction experiments were repeated with different crystals. In addition, several crystals were measured until a suitable individual was found, since

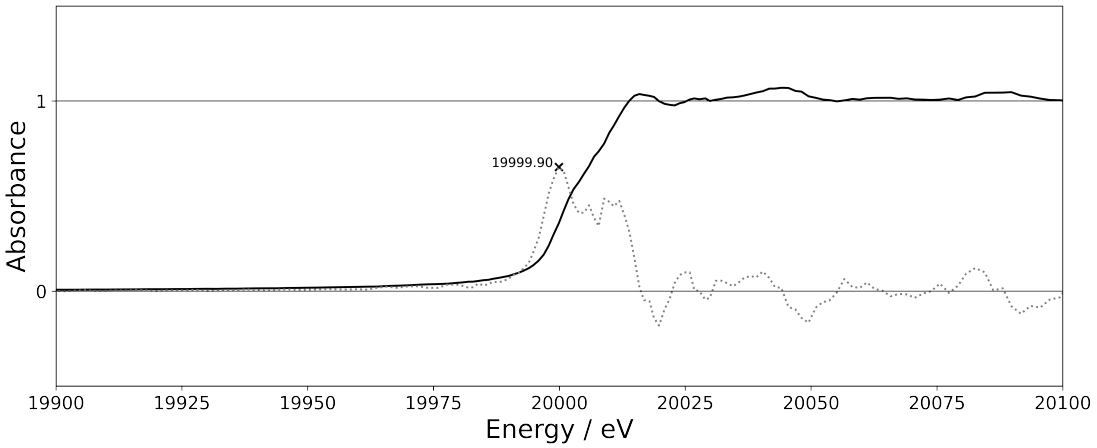

Figure 3.2: X-ray absorption spectrum for molybdenum metal foil (black line) and its derivative (dotted line). The K edge was determined at 19,999.90 eV.

indexing and possible twinning cannot be checked directly during measurements at a synchrotron beamline.

3.2.2 Calibration spectrum of molybdenum metal foil

Fig. 3.2 shows the calibration spectrum of molybdenum metal foil. The first maximum of the derivative defines the Mo K absorption edge and reveals an instrumental offset of 0.10 eV.

3.2.3 $Mo(CO)_6$

Fig. 3.3 shows the obtained X-ray absorption spectrum of $Mo(CO)_6$. After a pre-edge at 20,001 eV, the K absorption edge is shifted by 12 eV to 20,011.90 eV. Above the absorption edge, strong oscillations are observed in the near EXAFS region which correspond to the octahedral geometry of $Mo(CO)_6$.

The spectrum differs significantly from the calibration spectrum of molybdenum metal in all features including presence of the pre-edge, the shift of the absorption edge and a very defined fine structure region above the absorption edge. The deviation from the calibration spectrum is remarkable as the formal oxidation state of molybdenum in this organometallic complex is zero. However, considerations on the electronic properties in carbonyle compounds, which are known as strong π acceptor ligands provide a good explanation for such a significant shift

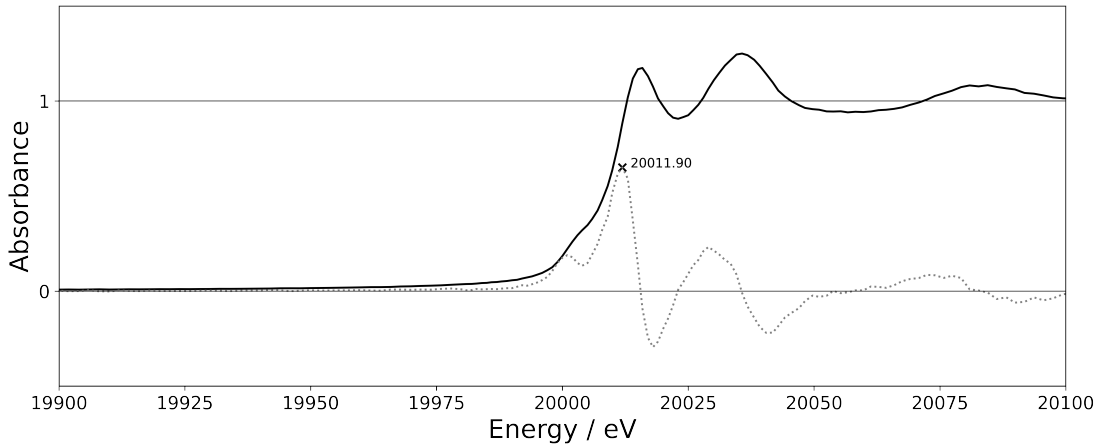

Figure 3.3: X-ray absorption spectrum for $Mo(CO)_6$ (black line) and its derivative (dotted line). The K edge was determined at 20,011.90 eV.

with respect to the molybdenum metal foil.[64] This is, of course, additional to the fundamental differences in electronic structure when chemical complexes are compared to metals.

Maxima and minima in the derivative are at 20,001 eV (pre-edge), 20,012 eV (global maximum, edge of Mo in $Mo(CO)_6$), 20,018 eV (global minimum), 20,029 eV (local maximum) and at 20,041 eV (local minimum) energy. The energies of these extrema serve as measurement energies for the X-ray diffraction experiments performed on this compound.

3.2.4 $(MeCN)_3Mo(CO)_3\times(MeCN)$

Fig. 3.4 shows the obtained XAS of $(MeCN)_3Mo(CO)_3\times(MeCN)$. After a pre-edge at 20,001 eV the K absorption edge is shifted by almost 10 eV. Above the absorption edge, some oscillations are observed in the near EXAFS region which correspond to the distorted $C3_v$ symmetry of $(MeCN)_3Mo(CO)_3\times(MeCN)$.

This downshift relative to $Mo(CO)_6$ is to be expected as three strong π acceptor ligands of carbonyl are exchanged for three weaker π acceptor ligands of acetonitrile.[64] The total shift in energy for the absorption edges is higher than expected. With a difference of about 2 eV with respect to $Mo(CO)_6$, this shift would correspond to a difference of at least one oxidation state at the molybdenum centre. However, there are reported cases in the literature where a shift of this magnitude is observed for a metal atom in the same formal oxidation state.

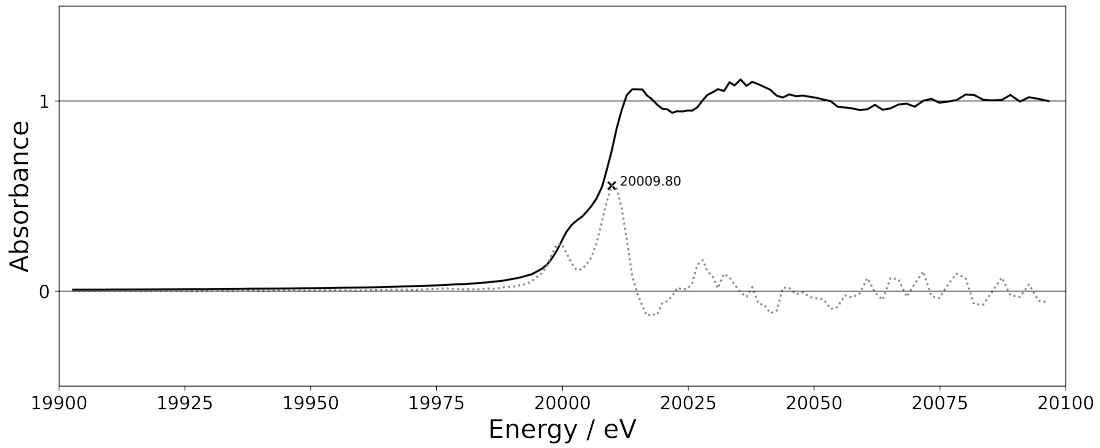

Figure 3.4: X-ray absorption spectrum for$(MeCN)_3Mo(CO)_3\times(MeCN)$ (black line) and its derivative (dotted line). The K edge was determined at 20,009.80 eV.

Shimizu *et al.* reported on the ligand field effect on the chemical shifts of absorption edges for copper(II) spectroscopy.[65] They observed a difference of up to 1.8 eV depending on the ligand and coordination geometry.

3.2.5 (TMEDA)(MeCN)Mo(CO)$_3$

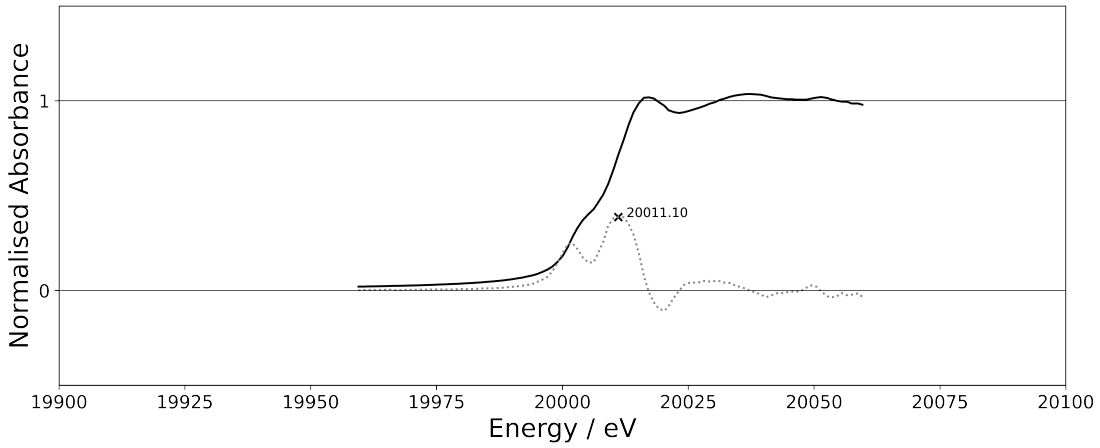

Figure 3.5: X-ray absorption spectrum for (TMEDA)(MeCN)$Mo(CO)_3$ (black line) and its derivative (dotted line). The K edge was determined at 20,011.10 eV.

Fig. 3.5 shows the obtained X-ray absorption spectrum of (TMEDA)(MeCN) $Mo(CO)_3$. After a pre-edge at 20,001 eV the K absorption edge is shifted by about 11 eV to 20,011.10 eV with respect to molybdenum metal. Above the absorption edge, some oscillations are observed in the near EXAFS region.

For the same reason as in the case of $(MeCN)_3Mo(CO)_3\times$ (MeCN), a downshift with respect to $Mo(CO)_6$ is observed.

3.2.6 $(TACN)MoO_3$

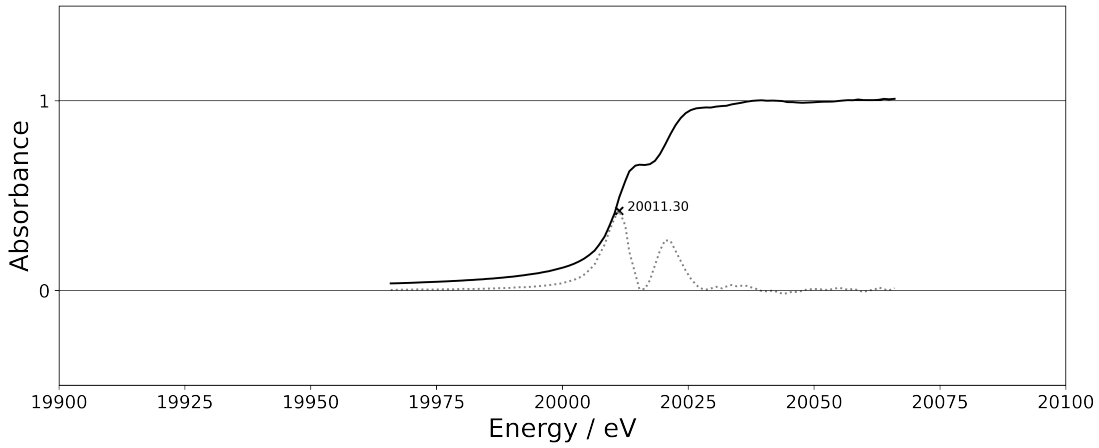

Figure 3.6: X-ray absorption spectrum for$(TACN)_3MoO_3$ (black line) and its derivative (dotted line). The K edge was determined at 20,014.10 eV.

Fig. 3.6 shows the obtained X-ray absorption spectrum of $(TACN)MoO_3$. After a prominent pre-edge at 20,003 eV the K absorption edge is shifted by about 14 eV to 20,014.10 eV relative to elemental metal. Above the absorption edge, no significant oscillations are observed in the near EXAFS region which correspond to the octahedral coordination geometry of $(TACN)_3Mo(CO)_3\times$ (MeCN).

A significant shift of the absorption edge with respect to $Mo(CO)_6$ is observed. Although this shift is not as pronounced as expected for a formal Mo(VI) atom, it is consistent with the higher oxidation state in $(TACN)MoO_3$ and therefore its upshifted K absorption edge.

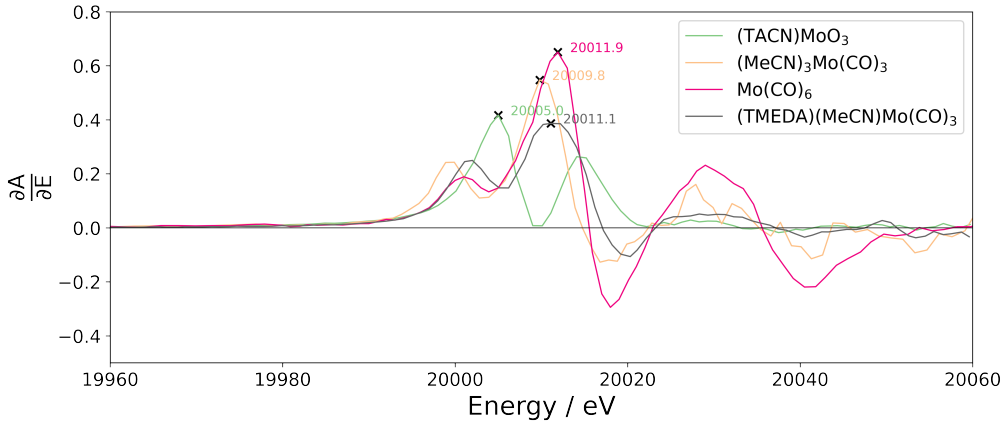

Figure 3.7: Comparison of the derivatives of the X-ray absorption spectra of the measured compounds. The energy above each plot denotes the K absorption edge for molybdenum determined for the respective compound.

3.2.7 Comparison

Fig. 3.7 compares the derivatives of the measured X-ray absorption spectra. The first maximum in the derivatives relates to the pre-edge. The second maximum reveals the K absorption edge of molybdenum in the respective compound.

$(MeCN)_3Mo(CO)_3\times(MeCN)$, $Mo(CO)_6$ and $(TACN)MoO_3$ follow their expected trends: $(TACN)MoO_3$ featuring molybdenum in a formal oxidation state of +VI reveals its edge shifted towards higher energy, whereas the other compounds feature a formal Mo(0) species. When $Mo(CO)_6$ and $(MeCN)_3Mo(CO)_3\times(MeCN)$ are compared, the latter possesses a different ligand-field as less π backbonding accepting ligand.[64] Therefore, the absorption edge of $Mo(CO)_6$ is also shifted towards higher energy relative to $(MeCN)_3Mo(CO)_3\times(MeCN)$. $(TMEDA)(MeCN)Mo(CO)_3$ states an exception to these considerations as its ligand-field is even less accepting towards π backbonding but its absorption edge lies at an energy in between $Mo(CO)_6$ and $(MeCN)_3Mo(CO)_3\times(MeCN)$.

However, this could be a result of differences in calibration since this spectrum was recorded on a different day than the other spectra. For the other compounds no spectra could be found in the literature, the absorption edge and pre-edge for $(TACN)MoO_3$ are consistent with measurements performed and calculated by DeBeer *et al.*.[60]

A large discrepancy is observed, when the obtained XAS of $Mo(CO)_6$ and the

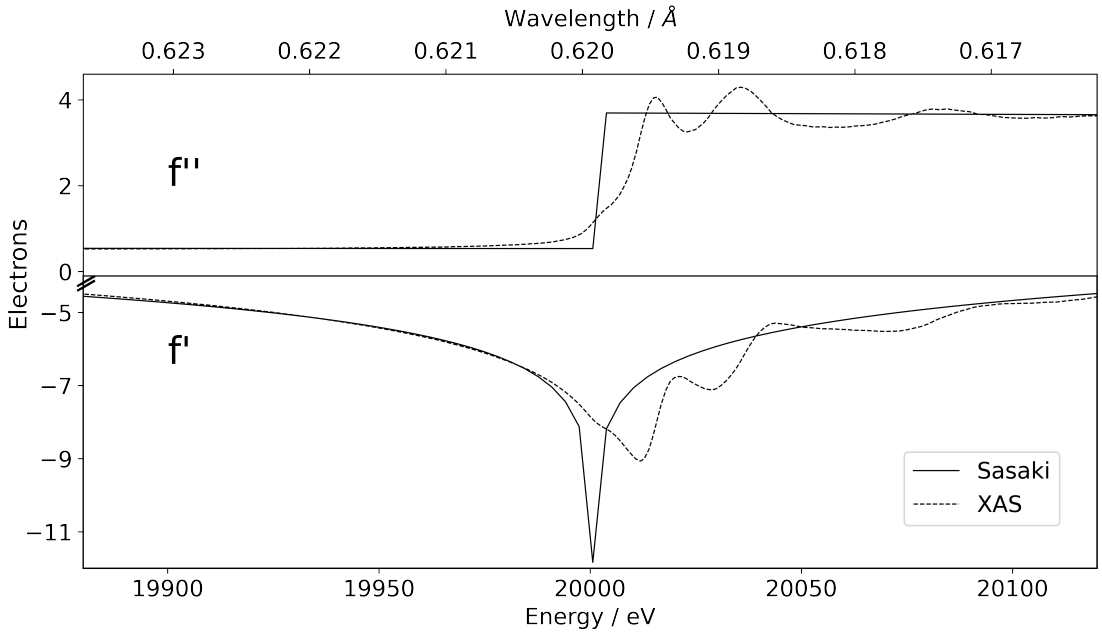

Figure 3.8: X-ray absorption spectrum of $Mo(CO)_6$ and the respective f' values according to the Kramers-Kronig relation in comparison to the vales tabulated for molybdenum according to Sasaki.[67, 53, 46]

calculated f' values are compared to the tabulated data by Sasaki (see Fig. 3.8). Already as much as 30 eV below the absorption edge, a deviation from the recorded spectrum and the tabulated values can be observed for f''. The absorption edge is clearly shifted relative to the tabulated values in both parameters f' and f''. Furthermore, both values show strong oscillations above the absorption edge. The deviation found here is in good agreement with the findings of Guss *et al.*[66]

3.3 X-ray diffraction data

3.3.1 General procedure

Synchrotron X-ray diffraction experiments were performed on the sample compounds $Mo(CO)_3$ and $(MeCN)_3Mo(CO)_3\times(MeCN)$. Diffraction data of the remaining two compounds have not been performed yet.

A suitable crystal of dimensions about 0.1 x 0.1 x 0.1 mm^{-3} for each samples was mounted on a SPECS synchrotron diffractometer at the beamline BM20 at the ESRF, Grenoble.[63] According to the K absorption edge of molybdenum determined from the X-ray absorption spectra, $Mo(CO)_6$ diffraction experiments were carried out at energies of 19,900 eV, 19,960 eV, 19990 eV, 19995 eV, 20,001 eV, 20,006 eV, 20,012 eV, 20,015 eV, 20,018 eV, 20,024 eV, 20,029 eV, 20,035 eV, 20,041 eV, 20,060 eV and 20,100 eV. $(MeCN)_3Mo(CO)_3\times(MeCN)$ diffraction data was acquired at energies of 19,900 eV, 19,960 eV, 19,995 eV, 20,001 eV, 20,005 eV, 20,010 eV, 20,014 eV, 20,018 eV, 20,022 eV, 20,040 eV and 20,100 eV. The diffraction pattern was collected using a DECTRIS PILATUS3 X 2M detector in 0.1° fine-slicing scan mode at a temperature of 100 K. Compression and transformation of the data was performed using the `SNBL Tool Box`.[68] Data procession, reduction and multi-scan absorption correction were performed using `CrysAlisPro`.[69] Further treatment and evaluation was conducted in the crystallographic software `Olex2` [42] employing the program `ShelXT` [70] for structure solution and `olex2.refine` [71] as refinement engine.

Three separate crystallographic models were created for each measurement and each compound with different anomalous dispersion parameters. Values from Sasaki[53], Henke[54] were employed as well as those obtained from refinement of f' and f'' for molybdenum as free parameters in the least-square refinement of the structures.

The structure model of $Mo(CO)_6$ was treated with Hirshfeld-Atom-Refinement to account for non-spherical bonding in this metal-organic complex using `NoSpherA2` [41]. Due to disordered solvent MeCN in $(MeCN)_3Mo(CO)_3\times(MeCN)$ across a mirror plane, a fully converged HAR model was not achieved for this compound. Instead, crystallographic models based on the independent atom model were compared for all three sets of dispersion correction parameters. The implication of this difference on the dispersion values between the HAR and IAM model is discussed below in section 3.3.4.

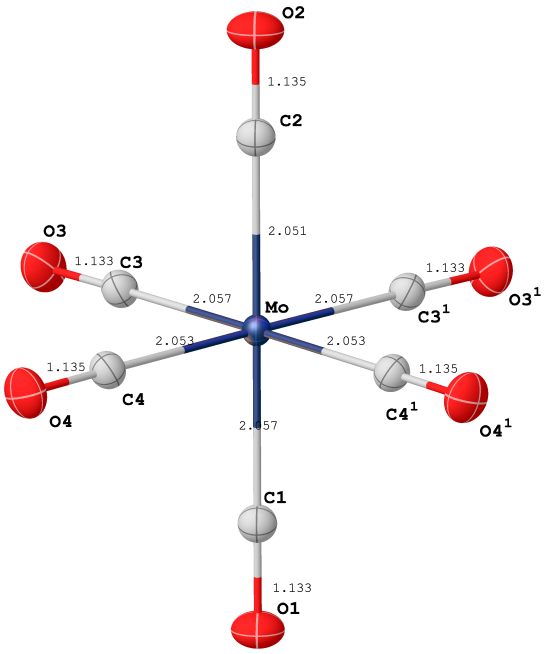

Figure 3.9: Structure of $Mo(CO)_6$ with all atoms labelled and bond lengths shown. X^1 denotes a symmetry generated atom. Ellipsoids for atomic displacement are shown at 50 % probability level.

3.3.2 $Mo(CO)_6$

$Mo(CO)_6$ crystallizes in the orthorhombic space group *Pnma* with unit cell constants a = 11.73370(11)Å, b = 11.21588(9)Å and c = 6.3449(5)Å and half a molecule in the asymmetric unit (Z = 4, Z' = 0.5). Fig. 3.9 shows the octahedral structure of $Mo(CO)_6$, which is completed from the asymmetric unit by a mirror plane through O2, C2, Mo, C1 and O1, which therefore are located on special positions. There are four distinct oxygen and carbon positions with additional two being symmetry generated by the mirror plane. Mo–C bond lengths are in the range of 2.051(1)–2.057(1) Å and C–O bonds are in the range of 1.133(1)–1.135(1) Å. Both Mo–C bond lengths as well as cell constants are in agreement with literature structures.[72]

Fig. 3.10 shows the dispersion parameters for the crystallographic models of $Mo(CO)_6$ using wavelengths of the aforementioned energies around the K absorption edge of molybdenum. Each plus sign (tabulated) or cross sign (refined) corresponds to a distinct crystallographic model with the source of dispersion parameters indicated by its colour. Small dots show the progression of the tabulated

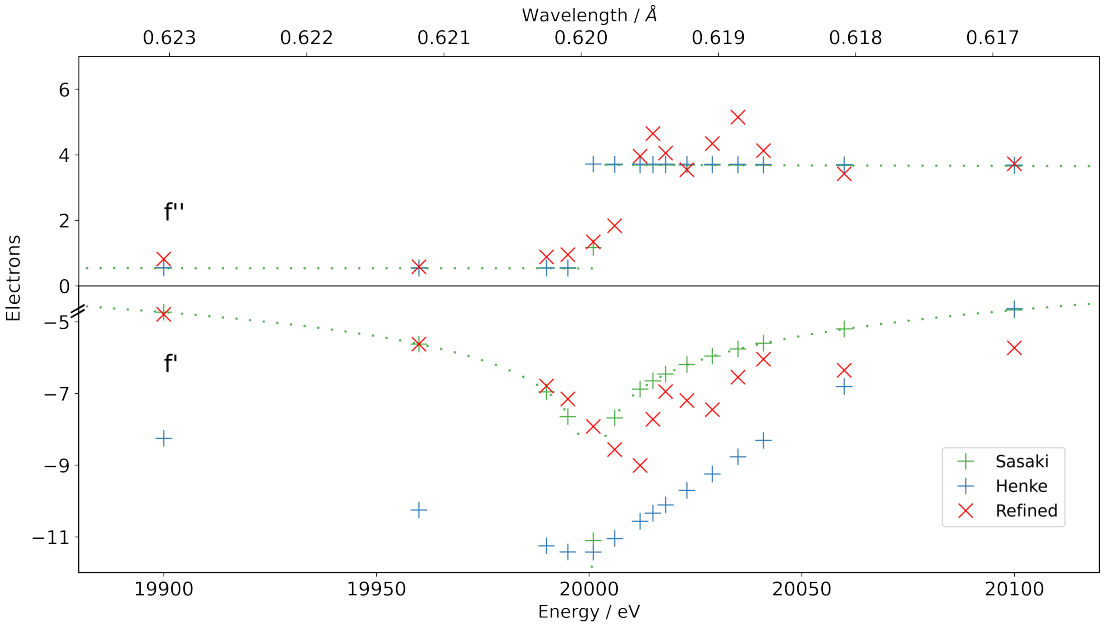

Figure 3.10: Dispersion parameters for the crystallographic models of $Mo(CO)_6$ at various energies.

values of the Sasaki table for orientation and comparison to Fig. 1.4.

Starting at 19,900 eV, the refined dispersion parameters are nearly identical to the values obtained from the Sasaki table. However, there is a significant offset between refined values and the Sasaki table: Refined f' values are systematically lower than their tabulated counterparts and f'' are systematically higher. On the contrary, the Henke table lacks more data points around this regime for f' and f'' and shows a drastic offset to both other sources of about 3.5 electrons.

This trend continues when approaching the absorption edge of molybdenum metal at 20,000 eV and results in the lowest values of f' for both sources at 20001 eV with a value of about –11 electrons. At this energy, the tabulated values for f'' jump from about 0.2 electrons to about 4 electrons. Different behavior was observed for the refined values: f' decreases further after 20,001 eV and reaches its lowest value at 20,012 eV. Above 20,012 eV, the refined values for f' substantially increase and are oscillating. The refined f'' does not reveal a sudden jump at 20,001 eV but rather shows a sigmoidal increase with its first peak at 20,012 eV and oscillation above this initial peak.

For comparison between the crystallographic models at each energy, the respective quality parameters R_1 and wR_2 are shown in Fig. 3.11. These R-factors

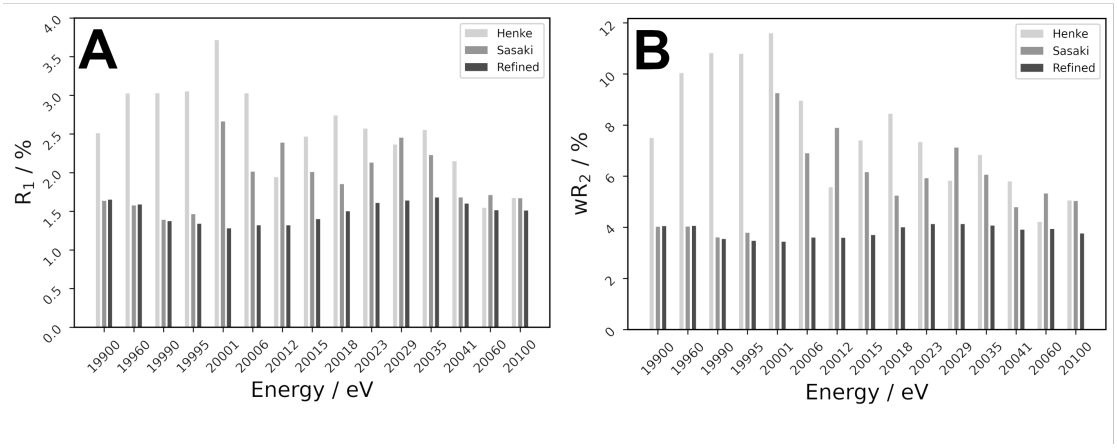

Figure 3.11: Quality indicators R_1 (**A**) and wR_2 (**B**) for the resulting crystallographic models for $Mo(CO)_6$

compare the measured structure factors to the calculated structure factors of the crystallographic model.

For every measurement, the R-factors are worse for the models relying on tabulated dispersion values. Additionally, these models vary strongly in their quality at the different energies. Despite the fact the same crystal was used during measurements and identical starting geometries were used for the refinements. The range of resulting residuals is worst for the models obtained by applying the Henke tables, yielding values between $1.94\ \% \leq R_1 \leq 3.71\ \%$ and $5.57\ \% \leq wR_2 \leq 11.6\ \%$. This strong fluctuation is a result of the linear interpolation between only few data points in the vicinity of the absorption edges. With more precisely tabulated data available in that area the Sasaki tabulated values lead to lower and less spread out quality indicators ($1.39\% \leq R_1 \leq 2.66\%$, $3.56\% \leq wR_2 \leq 9.25\%$). However, the lowest average R factors and the least deviating ones are obtained with refined anomalous dispersion parameters. In that case, a very narrow range of $1.28\% \leq R_1 \leq 1.68\%$ and $3.44\% \leq wR_2 \leq 4.13\%$ is achieved.

For energies at which the difference between the table and the refined values is the highest, for example at 20,001 eV and 20,029 eV, the Sasaki model performs worst. The latter of these energies shows the remarkable case that the linearly interpolated Henke table results in a value closer to the refined values than the Sasaki table. Consequently, this is the only energy where the Henke model performs better than the Sasaki model.

Consequently, the refinement of dispersion values is beneficial for the quality of

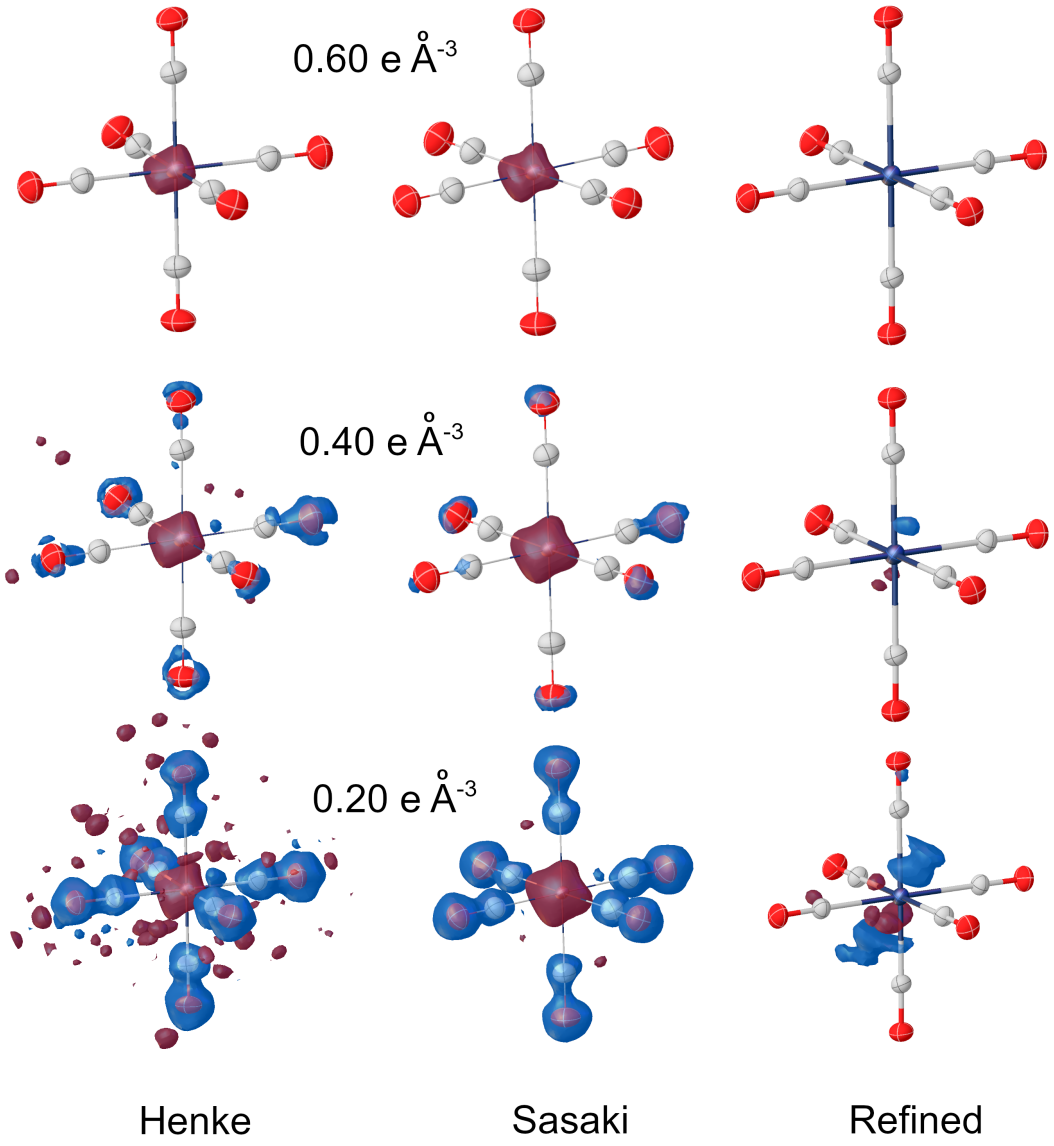

Figure 3.12: Residual electron density maps of the structures relying on Henke, Sasaki and refined dispersion correction at 20,001 eV. Atomic displacement ellipsoids are drawn at 50 % probability level. A red iso-surface indicates positive and a blue iso-surface negative residual electron density, respectively.

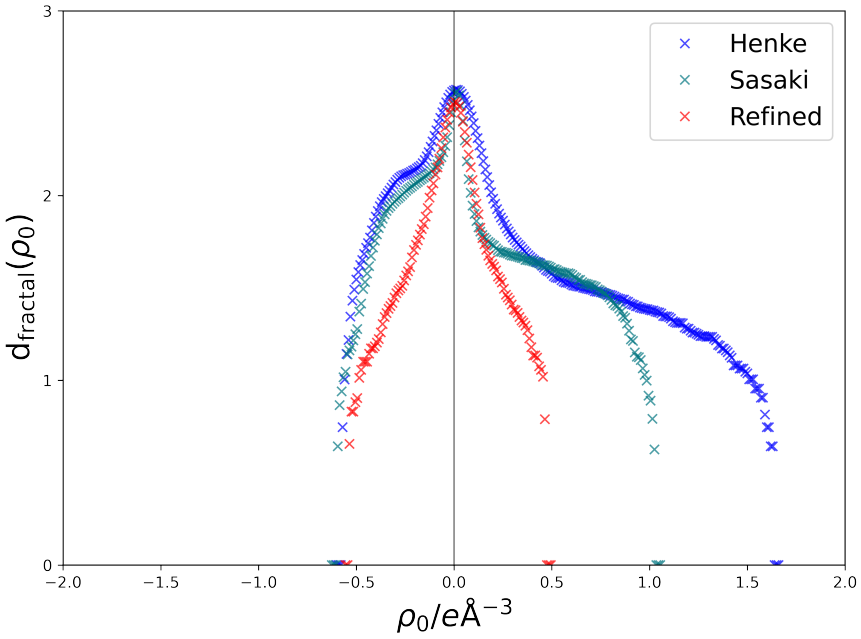

Figure 3.13: Fractal dimension plots for the crystallographic models based on the different dispersion values.[73]

the crystallographic model. This is also reflected in the residual electron density maps of the respective models. Fig. 3.12 compares the electron density maps for the three crystallographic models at 20,001 eV at different iso-surface-levels.

The model based on the Henke table, consistent with the resulting R-factors, shows the highest residual electron density for all iso-surface levels. Both, the Henke and Sasaki based models, show significant residual electron density in close vicinity of the central atom. As a consequence of this lack of electron density, their models do not account for all measured electron density near to the molybdenum atom. At lower iso-surface levels negative residual density is also found around the carbonyle ligands. This showcases the effect of the dispersion correction onto the entire structure factor, which according to equation 1.2 consists of a sum over all atomic form factors for each reflection. This effect is not observed for the models with refined dispersion correction. Instead residual density is observed along the crystallographic (010) direction at the lowest iso-level. This density cannot be explained with dispersion correction or crystallographic modeling but might originate from insufficient absorption correction.

The fractal dimension plots according to Meindl & Henn [73] in Fig. 3.13 of

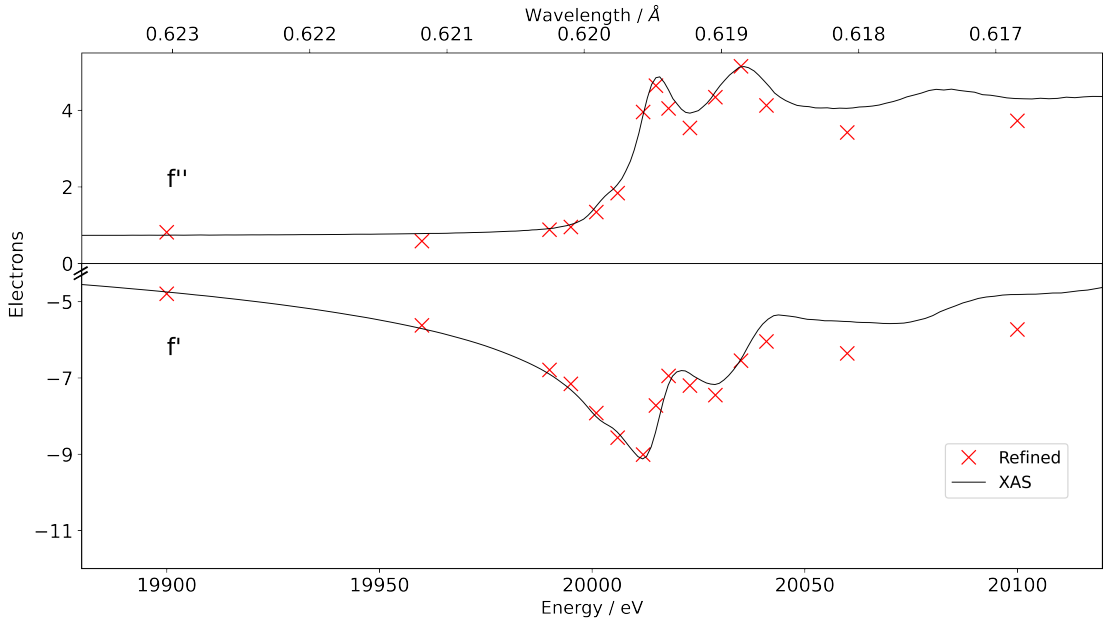

Figure 3.14: Comparison of X-ray absorption spectrum and refined dispersion parameters for $Mo(CO)_6$. Values for f' for the XAS were calculated using the kkcalc program [67]

the three models are also consistent with this trend. These show, how the residual density is distributed in the unit cell at different iso-levels. A deviation from two underlying statistical noise distributions indicates errors in the crystallographic model visible in the crystallographic model, where this deviation occurs. Both models based on tabulated dispersion corrections show strong shoulders towards positive residual density starting from about +0.2 e/Å^3 and a less pronounced shoulder at the negative side starting from –0.15 e/Å^3. The model with refined dispersion values shows neither of these artefacts.

Comparison to XAS

Fig. 3.14 shows the X-ray absorption spectrum of $Mo(CO)_6$ and the respective calculated values for f' according to the Kramers-Kronig relation (equation 1.13) together with the dispersion parameters refined from the diffraction data.

The refined dispersion parameters follow the observed absorption spectrum and the calculated values for f' across the whole spectral range. All spectral features such as the pre-edge, shift of absorption edge and the fine structure above the

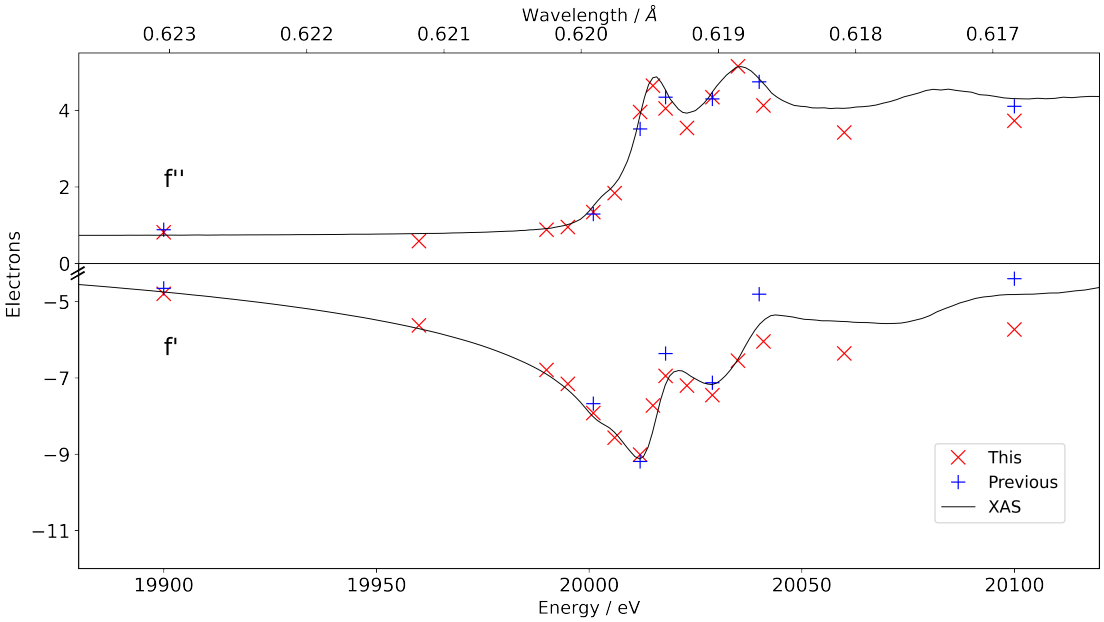

Figure 3.15: Comparison of the values shown in Tab. 3.1 and the XAS, as well as calculated spectral f' values.[67]

absorption edge are reflected in the refined parameters. Far above the absorption edge the refined values are both lower than the XAS or calculated f' values. The reason for this could be radiation damage as the crystal exhibited a change in colour from clear colourless to green-black.

During another visit of the ESRF seven measurements at similar energies were performed on crystals of $Mo(CO)_6$.[74] The obtained dispersion parameters from those experiments are compared in Tab. 3.1 and Fig. 3.15. Both data sets are compared at a resolution of 0.62 Å, as the setup of the detector was not identical for both visits: in the second visit the static detector was tilted by 40° angle in order to collect data up to a higher resolution.

The difference in obtained dispersion values is low at energies below the absorption edge and an identical progression is observed. On the contrary, the values above the edge differ more. In particular, at 20,040 eV f' is off by 1.240 electrons and f'' by 0.618 electrons. The least deviation is obtained at 20,001 eV with a difference of 0.246 electrons for f' and 0.052 electrons for f''. This was also the energy at which the tabulated dispersion values performed worst. The observed difference above the absorption edge is therefore a possible result of crystal damage in the experiment with more energies and hence more than twice the radiation

	f'			f"		
Energy	Previous	This	Δf'	Previous	This	Δf"
19,900	-4.65(5)	-4.79(5)	0.14	0.88(6)	0.81(5)	0.07
20,001	-7.66(3)	-7.92(4)	0.25	1.30(3)	1.34(4)	-0.04
20,012	-9.19(4)	-9.02(4)	-0.18	3.51(3)	3.95(3)	-0.44
20,018	-6.36(6)	-6.95(6)	0.59	4.34(4)	4.05(5)	0.29
20,029	-7.13(5)	-7.45(6)	0.32	4.30(3)	4.34(5)	-0.04
20,040	-4.81(6)	-6.05(6)	1.24	4.74(4)	4.12(5)	0.62
20,100	-4.40(6)	-5.72(6)	1.33	4.10(4)	3.72(5)	0.38

Table 3.1: Refined dispersion parameters obtained for two different crystals of $Mo(CO)_6$ on separate synchrotron shifts with different setup. Energies are given in eV.

dose.

Despite this, the general trend in the absorption spectrum and calculation is preserved for every pair of refined dispersion parameters. This shows that the spectral features impact the diffraction pattern in such a way that free refinement of the dispersion parameters is able to replicate these – without recording an absorption spectrum. This also explains the deviations from the tabulated dispersion parameters and the effects on the crystallographic models.

3.3.3 $(MeCN)_3Mo(CO)_3\times(MeCN)$

$(MeCN)_3Mo(CO)_3\times(MeCN)$ crystallizes as a MeCN solvate in the orthorhombic space group *Pbcm* with cell constants a = 8.1617(1)Å, b = 12.6157(1)Å and c = 14.6221Å and half a molecule in the asymmetric unit (Z = 4, Z' = 0.5). Fig. 3.16 shows the distorted octahedral structure of $(MeCN)_3Mo(CO)_3\times$ (MeCN). There are two distinct carbonyl positions and two distinct acetonitrile positions. An additional solvent molecule of acetonitrile is located at the mirror plane. The Mo–C bond lengths are in the range of 2.220(6)–2.213(1) Å for the acetonitrile ligands and in the range of 1.929(1)–1.933(1) Å for the carbonyl ligands. The C–O bonds are in the range of 1.160(1)–1.163(2) Å — slightly longer than in $Mo(CO)_6$, which indicates stronger π back–bonding from the metal into the ligand's anti–bonding $\pi^*_{x,y}$ orbitals.[64] The C–N bond lengths of the acetonitrile ligands are in the range of 1.133(1)–1.139(1) Å and thus slightly longer than in the solvent molecule, which has a C–N bond length of 1.132(2)Å. Cell constants and bond lengths are comparable but slightly shorter than in literature compounds.[75]

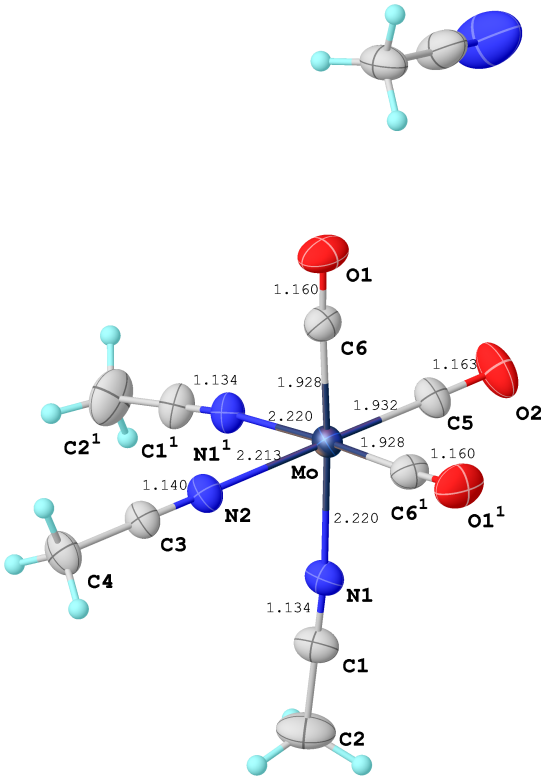

Figure 3.16: Structure of $(MeCN)_3Mo(CO)_3 \times (MeCN)$. X^1 denotes a symmetry generated atom. Ellipsoids are shown at 50 % probability level.

Fig. 3.17 shows the dispersion parameters for the IAMs of $(MeCN)_3Mo(CO)_3 \times (MeCN)$ at various energies around the K absorption edge of molybdenum. Each plus sign (tabulated) or cross sign (refined) corresponds to a distinct crystallographic model with its source for dispersion correction parameters indicated by its colour. Small dots show the progression of the tabulated values of the Sasaki table for orientation.

Just as in the case of $Mo(CO)_6$, the refined values deviate severely from the tabulated values. Especially for f'', an offset to higher values was constantly observed. The highest value for f'' was obtained at 20,040 eV with about 6.5 electrons. The lowest value for f' was –7.7 electrons and obtained at 20,010 eV, with no strong oscillation pattern at higher energies.

Comparison of the crystallographic R-factors in Fig. 3.18 shows a different pattern than in the case of $Mo(CO)_6$. Although still the lowest quality indicators were obtained for the models with refined dispersion parameters, the difference

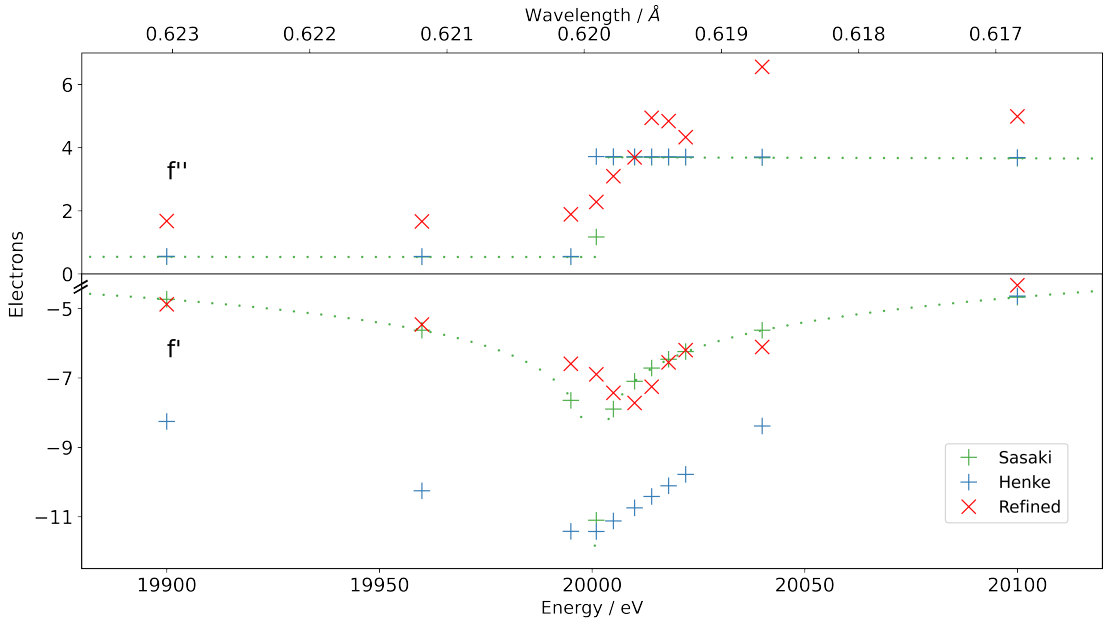

Figure 3.17: Anomalous dispersion parameters for the crystallographic models of $(MeCN)_3Mo(CO)_3\times(MeCN)$ at various energies.

is less pronounced. A general trend of increase in R-factors over the different measurements is observed. This indicates radiation damage over the duration of the consecutive measurements for this crystal. The Henke table yielded the worst performing crystallographic models while the Sasaki table yielded better agreement between measured and modeled intensities. The latter exhibits values generally close to the refined dispersion parameters in value and resulted in comparable R-factors.

The measurement at 20,040 eV, where the refined f'' had its highest value, shows the worst R-factors for all models and could therefore be treated as outlier to this study. A possible explanation for this outlier is that electrons were injected into the synchrotron storage ring shortly after the start of the experiment. This injection resulted in a strong discontinuity in the intensity of the beam and subsequent problems with the scaling of the data. The strongest difference between the Sasaki model and the model with refined dispersion parameters is obtained at 20,010 eV where the f' value had its lowest overall value.

The radiation damage to the crystal during the measurements makes a comparison of the residual electron density meaningless. During the measurements a colour change similar to the one of $Mo(CO)_6$ to a deep dark colour was observed.

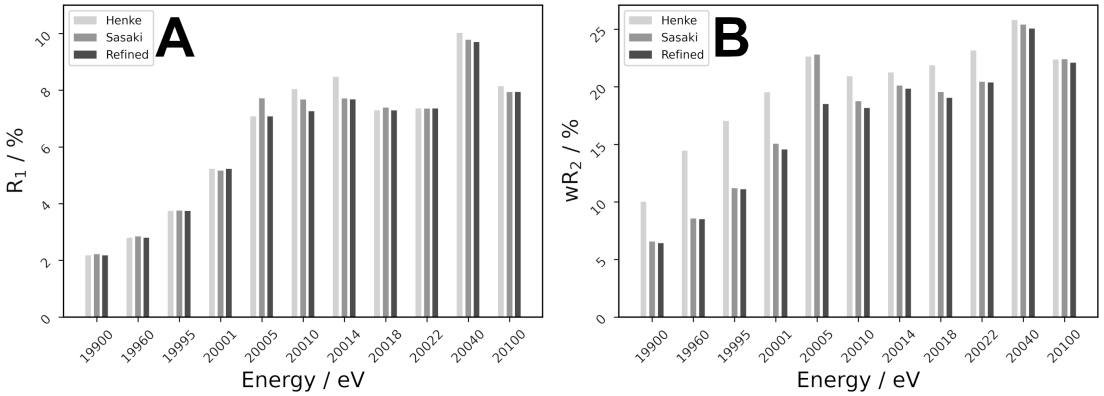

Figure 3.18: Quality indicators R_1 (**A**) and wR_2 (**B**) for the resulting crystallographic models for $(MeCN)_3Mo(CO)_3 \times (MeCN)$

With spherical residual electron density around the molybdenum atom for every model these maps do not give insight into the effect of dispersion refinement but rather show residual density that is not caused by dispersion effects.

Comparison to XAS

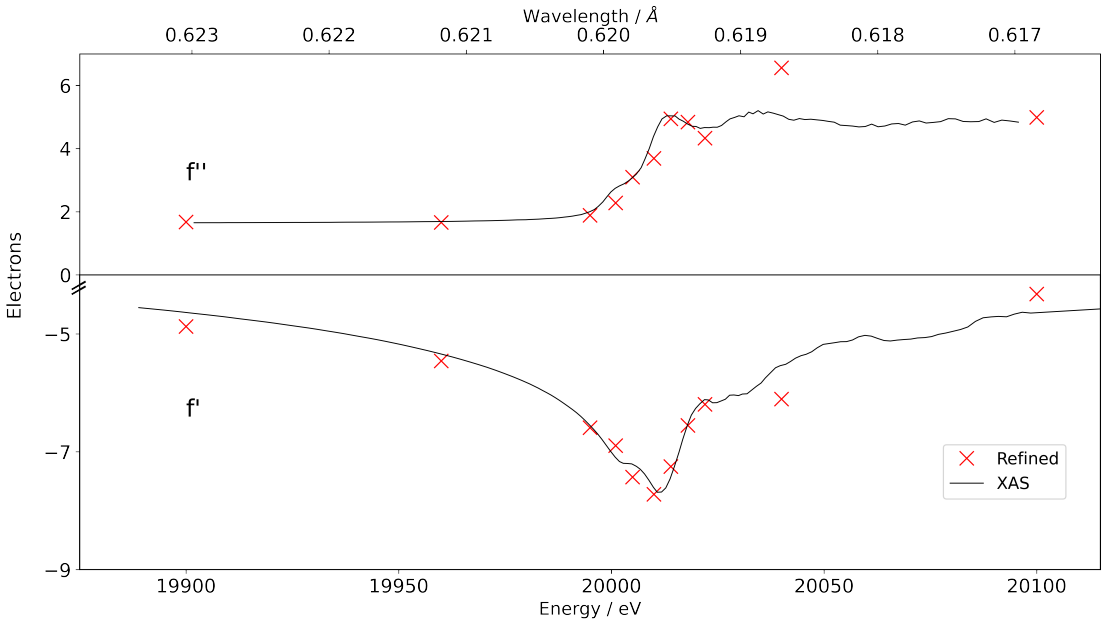

Figure 3.19: Comparison of the X-ray absorption spectrum and refined dispersion parameters for $(MeCN)_3Mo(CO)_3\times(MeCN)$. Values for f' for the XAS were calculated using the kkcalc program [67]

Fig. 3.19 shows the refined dispersion values compared to the recorded X-ray absorption spectrum of $(MeCN)_3Mo(CO)_3\times(MeCN)$. Despite the difficulties for the crystallographic models with crystal damage and independent atom model, the trends in the refined f' and f'' values largely follow the recorded absorption spectrum and calculations.

Especially the fine structure and absorption edge location are consistent to the spectrum. Below the absorption edge the values for f' are systematically lower than the ones calculated from the spectrum. One reason for this is the limited range of the X-ray absorption spectrum. The Kramers-Kronig relation (equation 1.13) employs an integral to calculate the real term f' from the imaginary term f'' or μ. To do this, the integral has to run over all frequencies. As there is only a limited range in which spectra were recorded, the software uses tabulated values outside of this range. As the transition is not necessarily smooth, the fitting can potentially introduce an offset to the calculated values.

3.3.4 Evaluation of the anomalous dispersion refinement

Both experiments have shown that the refinement of dispersion parameters can reproduce the features that are usually only observable in X-ray absorption spectra. In the case of $Mo(CO)_6$ this treatment resolves issues in the crystallographic model that are due to poor dispersion correction with tabulated values near an absorption edge. To determine, whether the refinement of dispersion parameters is reasonable, it is necessary to investigate the effect these parameters can have on the crystallographic model.

Correlations

Correlations in a crystallographic model indicate errors in the model such as a wrong space group and missing elements of symmetry. These correlations can be calculated from the variance–covariance matrix of the least–squares refinement. The covariance is a measure of variability of two variables and is described for a pair of variables (X, Y) with their values x_i and y_i and their respective mean values $\hat{x}$ and $\hat{y}$:

$$\mathrm{cov}(X,Y) = \frac{1}{N}\sum_{i=1}^{N}(x_i - \hat{x})(y_i - \hat{y}) \tag{3.1}$$

The variance is the same measure for only one variable. During the least-squares refinement a $N \times N$ matrix for all N variables is generated. The correlation coefficient for a pair of variables can then be calculated according to

$$\mathrm{corr}(X,Y) = \frac{\mathrm{cov}(X,Y)}{\sigma_X \sigma_Y} \tag{3.2}$$

with $\sigma_x = \sqrt{\mathrm{var}(x)}$ being the standard deviation. A correlation between two variables has a value between 0 and 1, where 0 means complete independence between the two variables and 1 a direct correlation.

The correlation matrices from all measurements of $Mo(CO)_6$ reveal significant correlations (> 0.50) between f' and f'' with all atomic parameters of molybdenum. There are strong correlations between dispersion parameters and the atomic displacement parameters with values up to 1.00 with an average of 0.915 for f' and 0.403 for f''. A strong correlation is also found for the positional parameters with values up to –0.999 and absolute average values of 0.529 for f' and 0.483 for f'' . There were no correlations > 0.50 with the dispersion parameters other than

the atomic ones of molybdenum. The correlation between the dispersion values and all parameters was on average 0.025 for f' and 0.018 for f''. Averaging for all values except the atomic parameters of molybdenum results in a correlation of 0.004 for f' and 0.003 for f''.

However, a correlation with those parameters of molybdenum is expected as both dispersion parameters and atomic displacement parameters model the electron density in the near vicinity of the metal atom. The anisotropic displacement parameters subsequently influence the positional parameters of molybdenum.

Despite the connection between f' and f'' via equation 1.13, no significant correlation was observed. The maximum value for their correlation was 0.259 with an average value of 0.189. The correlation calculated from the variance-covariance matrix is a measure for linear correlation only. As the relation between both dispersion parameters is more complex, a linear correlation is not specifically expected. However, it is still important to note that there was no significant linear correlation between f' and f''. The anomalous dispersion correction exhibited standard deviations in the order of 0.02 electrons for f' and f'' (see tables in 5.1).

Differences between HAR and IAM

Both dispersion refinement and the Hirshfeld-Atom-Refinement change the atomic scattering factor. While HAR changes the initial atomic form factor $f_{n,0}$ and accounts for non-spherical contribution based on DFT calculations, the dispersion correction adjusts the resulting overall scattering power.

Fig. 3.20 shows the difference between the dispersion parameters obtained from IAM and HAR models of $Mo(CO)_6$, respectively. The difference is more prominent for the real part of the dispersion parameters f' than for the imaginary part f''. In general, the obtained dispersion corrections are less correcting, for f' in a HAR model. On the contrary, they are more correcting for f'' in a HAR model. The overall progression of the refined dispersion parameters is identical, with an offset in the absolute value.

Comparing the obtained R-factors from IAM or HAR using either models based on tabulated or refined dispersion parameters gives insight how much each HAR or dispersion refinement benefits the accuracy of the models. The mean R-factors for the model based on the Sasaki table using the IAM were 2.47 % for R_1 and 7.38 % for wR_2. Employing HAR resulted in average R-factors of 1.92 % for R_1 and 5.67 % for wR_2. The mean R-factors for the models including the refinement of the anomalous dispersion values were $R_1 = 1.95\%$ and $wR_2 = 5.29\%$ in the

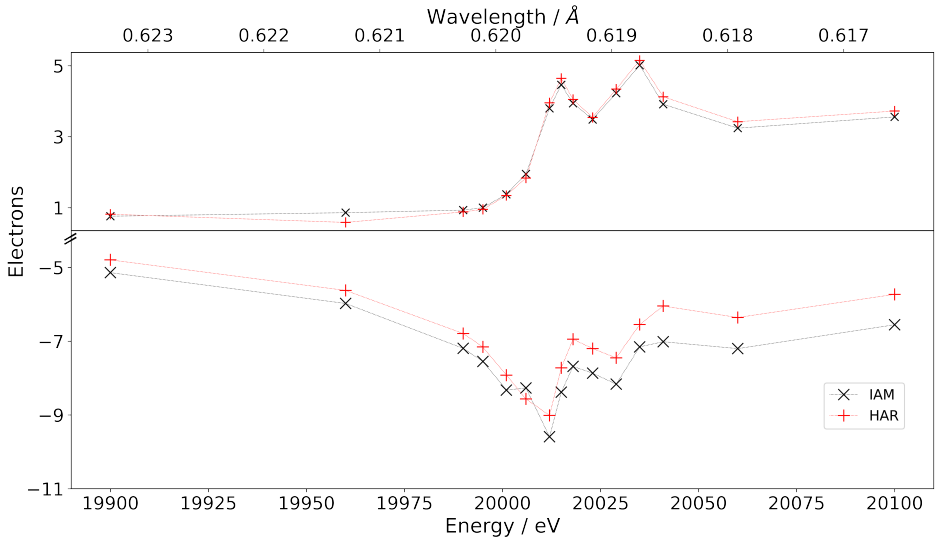

Figure 3.20: Progression of refined dispersion parameters for $Mo(CO)_6$ over the measured energies at the absorption edge of molybdenum.

IAM, but only $R_1 = 1.49\%$ and $wR_2 = 3.83\%$ for HAR. Therefore, a difference of 0.55 % in R_1 and 1.71 % in wR_2 can be attributed to the better performance of HAR above the IAM for the models with Sasaki's tabulated values. The further improvement of 0.43 % for R_1 and 1.84 % in wR_2 is a result of the refinement of the anomalous dispersion.

Hence, a similar improvement for the crystallographic models was achieved by both dispersion refinement and Hirshfeld-Atom-Refinement. It is worth mentioning that there is a proportion of electron density that can be described by both and that refinement of f' seems to account for this overlap. This means that there are minor differences between the HAR and IAM refined dispersion parameters and that HAR offers an overall better description of the crystallographic model. Therefore, a HAR should be performed in order to obtain accurate absolute values, especially for f'. The overall progression, however, is also valid in the IAM model and f'' progresses consistently with the XAS.

Resolution dependency

The IAM models with refined dispersion correction are also refined against data limited to various resolutions, as the HAR modelling of all data sets requires high computational effort. However, two reference models wer also compared for both

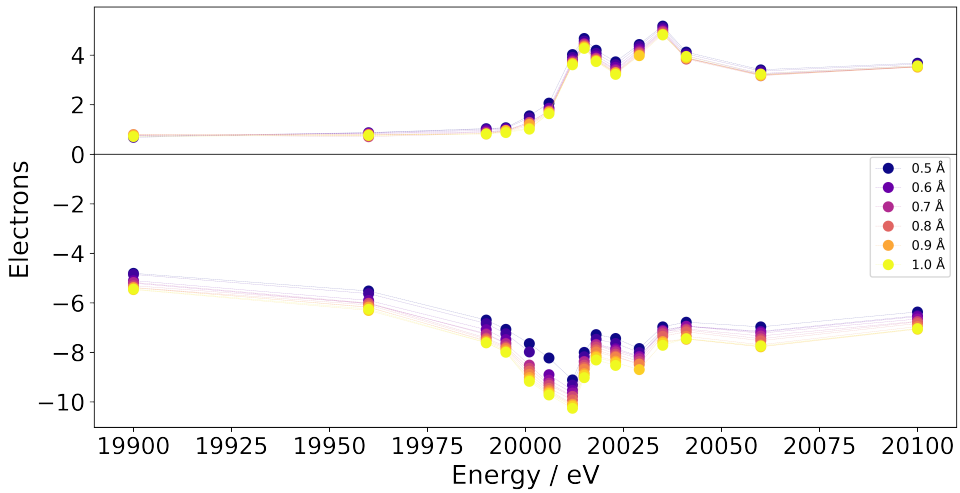

Figure 3.21: Resolution dependency for the refined dispersion models for $Mo(CO)_6$. The limited resolution data were obtained by omitting data of higher resolution directly in the refinement procedure.

HAR and IAM and no significant differences were found in trends regarding the resolution dependency.

Fig. 3.21 shows the refined dispersion parameters for models up to different resolutions. Similar to the comparison between HAR and IAM, f' and f'' are differently influenced by the resolution limit of the data. While f' decreases with increasing resolution, f'' is less affected, especially for the measurements far from theabsorption edge. However, the trend is opposite to that of f': The value of f'' increases together with the reduction of the resolution.

3.3.5 Wrong atom-type assignment

The crystallographic model of $Mo(CO)_6$ at 20,001 eV using tabulated dispersion values (see Fig. 3.12), exhibits negative electron density around the metal centre and comparably small anisotropic displacement parameters. This observation is usually indicating a wrongly assigned atom-type with less electrons, thus lower atomic number, compared to the current model. At 20.001 eV, the tabulated dispersion parameters appear to be above the absorption edge and therefore scale the scattering power of the modelled molybdenum atom more than it should be, since 20,001 eV is *below* the actual absorption edge of molybdenum in $Mo(CO)_6$.

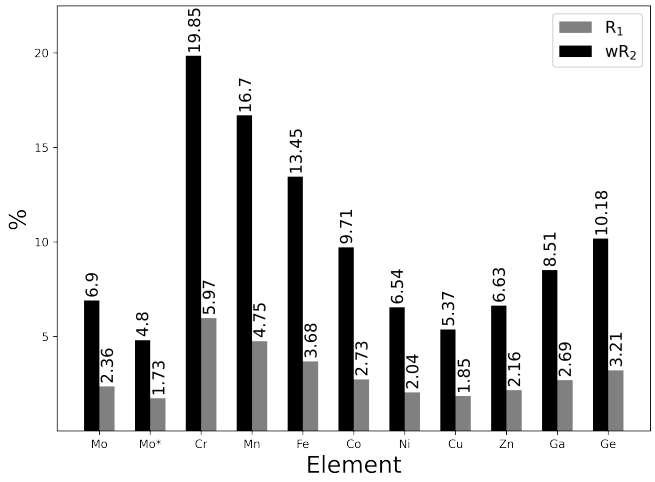

Figure 3.22: Quality indicators of the models for an IAM of $E(CO)_6$ (E = Mo, Cr–Ge) at 20,001 eV. Mo* denotes refined dispersion parameters. All other atoms were corrected for dispersion according to the Sasaki table.

Therefore, an excess of residual electron density remains in the immediate vicinity of the atom. Assigning a heavier atom to the metal position in $Mo(CO)_6$ results in worse quality indicators as is it provides more electron density and is almost uncorrected for dispersion. However, when lighter atoms than molybdenum are used, the R-factors indicate a merit for the crystallographic model.

As discussed in the introduction, at 20,000 eV the amplitude of the atomic form factors are almost identical for Mo and Ge due to the severe dispersion correction of molybdenum. However, as it can be seen from the absorption spectrum, the dispersion correction at 20,001 eV must be even stronger. Therefore, a "sweet-spot" for a wrong element–type is expected to be before germanium in the periodic table.

Fig. 3.22 shows the resulting R-factors when the metal centre in $Mo(CO)_6$ is modelled with the elements Cr–Ge. Especially Ni, Cu and Zn show better R-factors than the correct model with tabulated dispersion parameters for molybdenum. These corrupted models cannot be detected by standard structure checking algorithms like the Hirshfeld test, which determines wrong atom–types from the ratio of atomic displacement parameters.[76] Irrespective of this, the model based on refined dispersion parameters shows the lowest R-factors and indicates the best fit between observed and modelled intensities.

The good performance of the wrong models featuring Ni, Cu and Zn as central atoms can be explained by comparing their radial atomic form factors to the

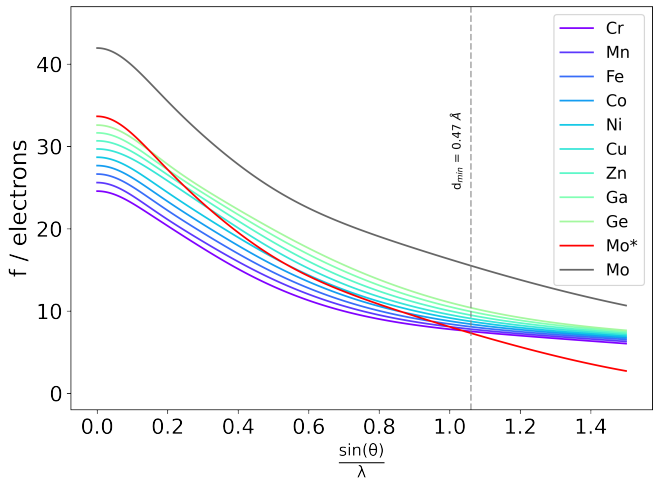

Figure 3.23: Comparison of the radial atomic form factors of the elements Cr–Ge, Mo (without dispersion correction) and Mo* (dispersion corrected with refined values). The grey line marks the maximum resolution of the diffraction experiments.

dispersion corrected one of molybdenum (see Fig. 3.23).

Looking at the differences between the corrected radial form factor of molybdenum to the ones for nickel, copper and zinc, the good fit can be explained (see Fig. 3.24). A mean difference of 1.1, 0.25 and –0.50 electrons are obtained for Ni, Cu and Zn, respectively. Therefore, the wrong atom–type model with the least deviation from the model with refined dispersion values yields the best agreement between observed and modelled intensities.

The question arises, whether dispersion refinement and Hirshfeld atom refinement are able to “fix” these intentionally wrong crystallographic models with incorrect atom types. For this reason, multiple models were compared using either dispersion refinement, HAR, or both. The resulting R-factors are shown in Fig. 3.25.

The dispersion-refined model sall have lower R-factors. In general, the dispersion refinement largely compensates for the effect of the wrong atom-type. On the contrary, the HAR even yielded worse crystallographic R-factors for the structures containing chromium and iron. Purely according to the quality indicators and in ignorance of the chemical aspects of these structures, one would have to choose the model with the central copper atom as best model when treating all candidates with dispersion refinement. Only when HAR is additionally applied, the correct candidate, Mo, also stands out in the R-factors, which emphasises the importance

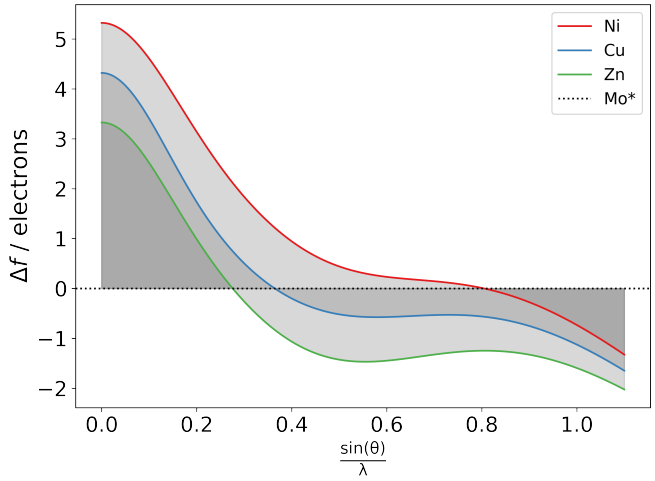

Figure 3.24: Difference plot between the radial atomic form factor of molybdenum and the for factors for Ni, Cu and Zn.

of HAR for refining the anomalous dispersion parameters. This is concerning as there are only minor differences to the molybdenum structure, but despite this, the refined dispersion parameters still give the lowest R-factors. Therefore, there should be a limitation on the dispersion refinement depending on the element and chosen wavelength. Of course, the dispersion correction parameters in the wrong atomic models are far from physically meaningful values, with values for f' ranging up to positive 6.1 electrons for chromium (see Tab. 3.2). However, if only molybdenum is treated with dispersion refinement because the energy of the X-rays is close to one of its absorption edges, there is no doubt, even if only the R-factors are considered.

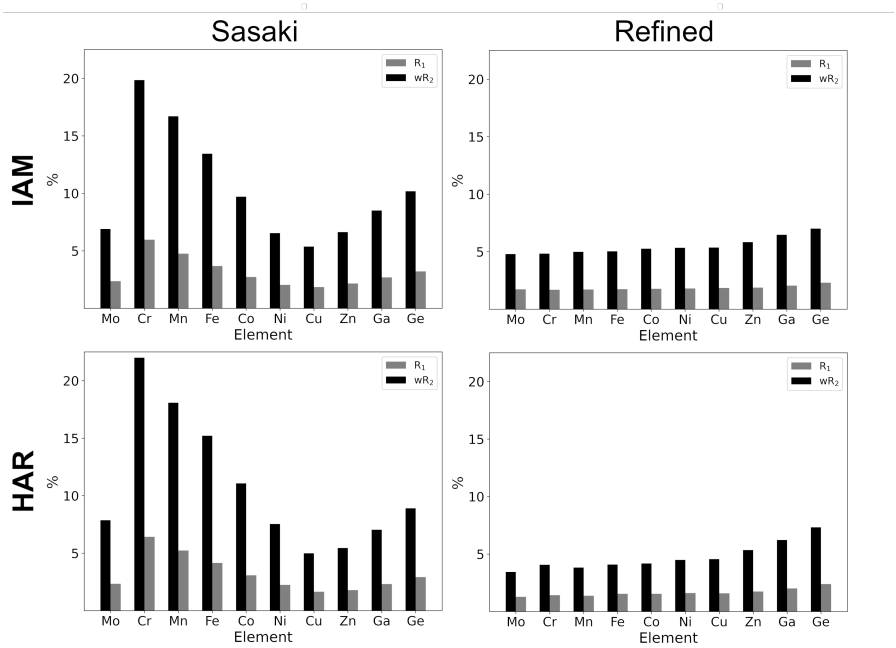

Figure 3.25: Comparison of the different combinations of modelling for the wrong atomic–type models against the data for $Mo(CO)_6$ at 20,001 eV. HARs were calculated using the DKH-PBE0 functional at x2c-TZVP level of theory. All fictional complexes were assumed to be low-spin complexes.

Element	Tab. $f'^{\dagger}$	Tab. $f''^{\dagger}$	Ref. f'	Ref. f''	$\Delta f'$	$\Delta f''$
Mo	-9.798	3.697	-9.372	1.019	-0.426	2.678
Cr	0.284	0.487	6.175	1.291	-5.890	-0.804
Mn	0.303	0.570	5.212	1.244	-4.909	-0.675
Fe	0.320	0.661	4.116	1.236	-3.796	-0.575
Co	0.332	0.763	2.943	1.200	-2.610	-0.437
Ni	0.337	0.874	1.759	1.169	-1.422	-0.295
Cu	0.338	0.996	0.294	1.117	0.044	-0.121
Zn	0.328	1.128	-0.714	1.086	1.042	0.043
Ga	0.311	1.273	-1.592	1.081	1.903	0.192
Ge	0.277	1.429	-2.346	1.099	2.623	0.330

Table 3.2: Differences between the tabulated and refined dispersion parameters for the HAR models of $E(CO)_6$ (E = Element). † according to [52].

3.3.6 Multipolar model of $Mo(CO)_6$

To gain insight into the electronic environment of molybdenum in the ligand-sphere, a multipole model was created from the data collected at 20,012 eV. The model was created with `MoPro`[77] on the basis of the Hansen-Coppens model.[31] Scaling factor, atomic coordinates, anisotropic displacement parameters were initially refined to create the IAM as basis for multipolar refinement. The valence populations, multipolar coefficients, expansion/contraction as well as anomalous dispersion correction parameters were then gradually included in the refinement. The quality of the model was evaluated using quantile-quantile plots according to Abraham and Keve [78] as well as residual density plots. Significant residual electron density of (+0.67 / –0.48 electrons) was observed which could not be resolved (see Fig. 3.26 **C**). As the chosen energy is located exactly at the absorption edge for molybdenum in $Mo(CO)_6$, insufficient absorption correction may be the reason for this issue: since no crystal movie is recorded at the synchrotron diffractometer, it was not possible to perform an analytical face-dependent absorption correction and only multi-scale absorption correction was applied. This residual density is similarly visible in the residual density plots for the HAR models (Fig. 3.12).

The question arises, how reasonable an absorption correction is at the exact energy of an absorption edge, as the value for μ is also calculated from tabulated f'' values. One could imagine an iterative process for the absorption correction at the end of the structure modelling to obtain new values for μ according to the refined dispersion parameters.

Nonetheless, the result allowed some insight into the charge density distribution in $Mo(CO)_6$. Fig. 3.26 **A** shows the 2D deformation density of the molybdenum atom in the cross section of the quadratic $Mo(CO)_6$ plane. An expected pattern for the 4d orbitals of molybdenum is visible. The deformation density of the entire cross section perpendicular to the one in **A** of the quadratic plane shows the ligand-metal interaction expected from carbonyl complexes (3.26 **B**) and the σ-bonding as well as the π-backbonding is described. Fig. 3.26 **D** shows the 3D electrostatic potential plot at the 0.5 electron total density iso-surface level. The central metal atom carries a positive charge that extends to the carbon atoms, while a respective negative charge is found at the oxygen atoms. This is consistent with the difference in electronegativity of the two atoms in the carbonyl ligand (3.44 for O and 2.55 for C according to Pauling[79]).

The charges determined through Bader partitioning in table 3.3 further validate this assumption.[80] Molybdenum carries a positive charge of 1.57 electrons, while

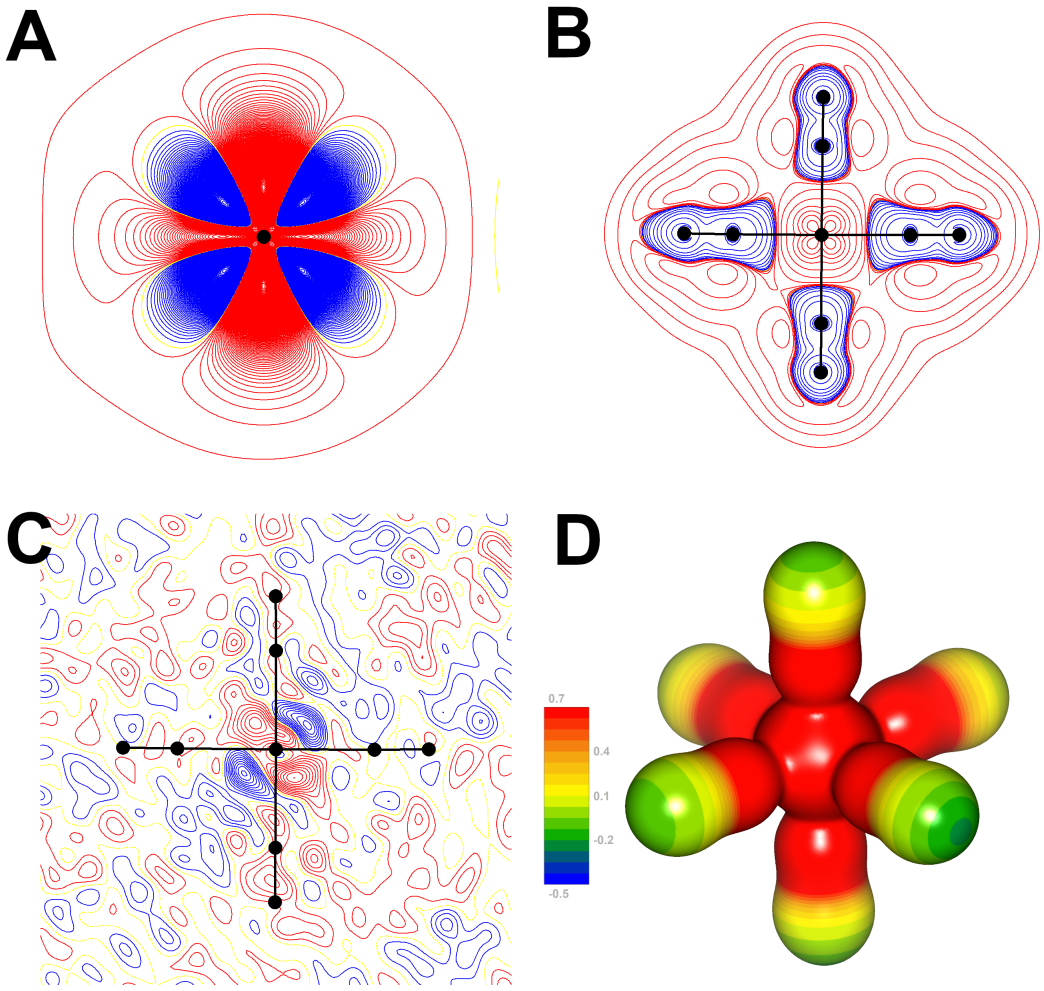

Figure 3.26: 2D deformation density of Mo **A** and logarithmic 2D deformation density of the quadratic $Mo(CO)_4$ plane **B**. Residual electron density of the quadratic $Mo(CO)_4$ plane **C**. Electrostatic potential at an total electron density level of 0.5 electrons **D**. **B** and **C** show only the asymmetric unit of $Mo(CO)_6$. Red color indicates positive, blue negative electron density.

Atom	Charge
Mo01	1.567
O002	-1.007
O003	-1.069
O004	-0.970
O005	-1.042
C006	0.610
C007	0.593
C008	0.874
C009	0.590
Total	0.146

Table 3.3: Atomic charges calculated from the $Mo(CO)_6$ multipolar model. Calculations are based on charge density integrations according to Bader.[80]

the carbonyl ligands are net negatively charged, with emphasis to the oxygen atom and a less pronounced positive charge at the carbon atom.

Overall, the multipole model reached the quality parameters $R_1 = 2.52$ % and $wR_2 = 3.03$ % with dispersion parameters $f' = -5.75$ and $f'' = 4.30$ electrons. Especially f' deviates strongly from the –9.01 electrons of the HAR model refinement. The f'' value however, is close to the 3.95 electrons of the HAR model. The reason for this deviation could lie in the parametric nature of the multipolar model. Deviations in the electron density could be also modelled by different parameters. Enforcing the dispersion values from the HAR model onto the multipolar model resulted in about 1 % worse quality parameters, indicating less consistency between measured and modelled data. Further studies on measurements with greater orientation towards multipole models will be needed to conclusively compare multipole modelling and HAR regarding dispersion refinement.

3.4 Application

3.4.1 Ionic molecular complexes containing cobalt

The refinement of anomalous dispersion parameters was beneficial to the quality of the structure in terms of quality parameters, bond-precision and displacement parameters. Therefore, the questions arises, how these differences affect the structures collected on standard laboratory diffractometers. In principle, it makes most

Cu K_α	8,041.1			**Cu K_β**	8,905.5		
Element	Edge	Energy	ΔE	Element	Edge	Energy	ΔE
Co	K	7,709	-332.1	Cu	K	8,979	73.5
Ni	K	8,333	291.9	Tb	L1	8,708	-197.5
Sm	L1	7,737	-304.1	Dy	L1	9,046	140.5
Eu	L1	8,052	10.9	Dy	L2	8,581	-324.5
Gd	L1	8,376	334.9	Ho	L2	8,918	12.5
Gd	L2	7,930	-111.1	Er	L2	9,264	358.5
Tb	L2	8,252	210.9	Tm	L3	8,648	-257.5
Dy	L3	7,790	-251.1	Yb	L3	8,944	38.5
Ho	L3	8,071	29.9	Lu	L3	9,244	338.5
Er	L3	8,358	316.9				
Mo K_α	17,444.6			**Ag K_α**	22,076.5		
Element	Edge	Energy	ΔE	Element	Edge	Energy	ΔE
At	L1	17,493	48.4	Ru	K	22,117	40.5
Rn	L2	17,337	-107.6	U	L1	21,757	-319.5
U	L3	17,166	-278.6	Np	L1	22,427	350.5
Np	L3	17,610	165.4	Pu	L2	22,266	189.5

Table 3.4: Elemental X-ray absorption edges and their energetic distance to standard laboratory X-ray sources energies. Data for emission lines and absorption edges are from references [58, 81]. All energies are in eV.

sense to investigate structures that have an element with an absorption edge close to the wavelength of the experiment. Table 3.4 shows which elements exhibit absorption edges relative to each distinct X-ray wavelength. Especially both copper emission energies have a variety of elements within a range of ±300 eV around their absorption edges. Therefore, the dispersion refinement of these elements with the respective X-ray source could reveal information on spectroscopic properties and provide better crystallographic models. Especially the late 3d-metals Cu, Ni and Co, which exhibit a rich redox chemistry in various oxidation states, could benefit from this method. Furthermore, the treatment of actinide structures or U and Ru compounds for Mo/Ag Kα could be of interest.

Cobalt is often applied in the transition metal chemistry towards the activation of main group elements such as phosphorus. For example, the Scheer *et al.* investigated element–element bond formation upon oxidation and reduction.[82] In this work, they reported among other things on the synthesis and properties of different cationic and anionic Co–complexes, which are coordinated by both P_4 and As_4 fragments. The diffraction data of these compounds are available online, and dispersion refinement could be employed for the cobalt atom as every measurement was performed using Cu Kα radiation. The Sasaki table corrects the scattering power of cobalt at an energy of 8,041 eV ($\lambda(\mathrm{CuK}\alpha_{1,2}) = 1.54187$Å with dispersion parameters of $f' = -2.44$ and $f'' = 3.620$.[53] Fig. 3.27 shows the resulting parameters after dispersion refinement for these structures.

The new values differ significantly form the tabulated values even though the K absorption edge of cobalt lies 332 eV below the excitation energy of Cu Kα radiation (see table 3.4). The two iso–electronic, dicationic structures of $(\mathrm{Cp'''Co})_2\mathrm{E}_4^{2+}$ (E = P, As; Cp''' = 1,2,4-triisobutyl-cyclopentadienyl) both show very similar refined dispersion parameters. On the other hand, the monoanionic species of $(\mathrm{Cp'''Co})_2\mathrm{As}_4^-$ reveal higher values for the refined dispersion parameters. These values give rise to the assumption that insights into electronic differences are possible. The resulting crystallographic models resulted in lower R_1 values in the range of 0.05—0.15 % to the original structures. Unfortunately, the iso–electronic structure to the anion, $(\mathrm{Cp'''Co})_2\mathrm{P}_4$, which was also described in this study, could not be compared as poor data quality made a dispersion refinement impossible.

Contrary to synchrotron beam-lines, which provide a high monochromatisation of the X-radiation, standard laboratory sources rely on an emission spectrum of the anode material. For Cu Kα radiation, the employed wavelength of $\lambda(\mathrm{CuK}\alpha) =$ 1.54187Å (8,041 eV) is actually comprised of the two wavelengths of $\lambda(\mathrm{CuK}\alpha_1) =$ 1.54059Å (8,048 eV) and $\lambda(\mathrm{CuK}\alpha_2) =$ 1.54443Å (8,029 eV) with an intensity

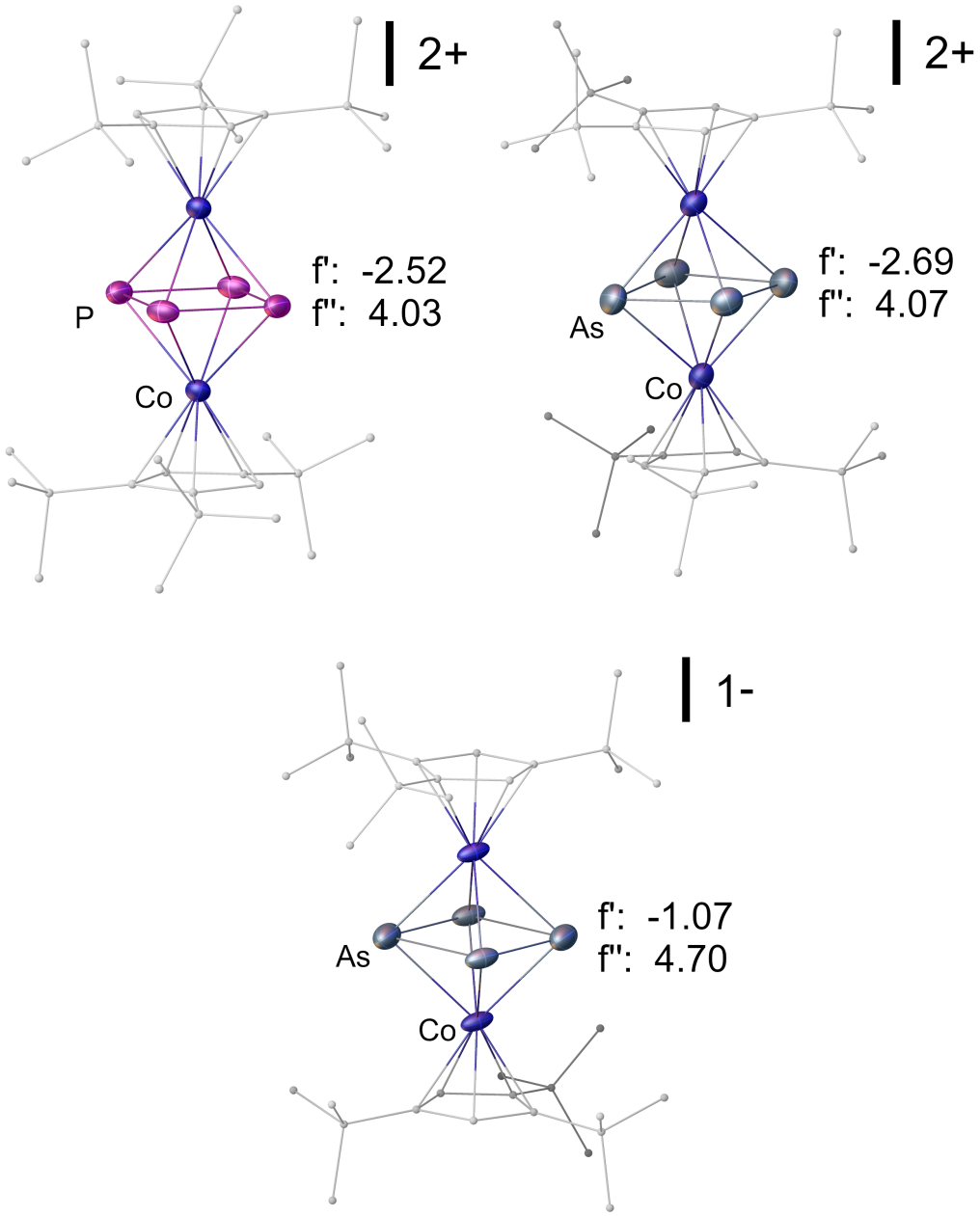

Figure 3.27: Structures of two cationic and one anionic organometallic Co–complexes with refined dispersion values for cobalt.

ratio of 2:1.[43] The two characteristic Cu Kα emission lines are about 20 eV apart from each other, which can potentially have severe effects when dispersion refinement is concerned. Contrary, the respective Kβ wavelength also consists of the two emission lines Cu Kβ_1 and Cu Kβ_3, which are not listed in literature as two separate lines, as they are very close to each other and thus not resolved.[43]

For Mo radiation, the effect of Kα splitting is even more pronounced. About 100 eV lie between the Mo Kα_1 (0.70933 Å, 17,479 eV) and Kα_2 (0.713618 Å, 17,374 eV) emission line.[43] This trend continues for even heavier anode materials like Ag, where the two Kα emission lines lie 173 eV apart from each other (Ag Kα_1 (0.55942 Å, 22,163 eV) and Kα_2 (0.56382 Å, 21990 eV). Further investigations are required for estimating this effect for dispersion refinement.

3.4.2 Multipole modelling of $Cp'''NiP_3$

Another example where refinement of dispersion parameters could be applied and tested is the multipole refinement of the complex $Cp'''NiP_3$. Measurements using both Mo Kα, which is the most commonly used wavelength for charge density experiments, and Cu Kβ radiation are compared and show a surprisingly good performance of the latter wavelength.[83] Usually, copper data sets with a limited resolution of 0.80 Å for Cu Kα radiation cannot be used for multipolar modelling as the limited resolution does not allow for separation of multipoles and thermal motion. Cu Kβ with a maximum resolution of 0.69 Å seems to resolve this problem with the additional gain of intensity when compared to Mo Kα radiation. Interestingly, the model based on Cu Kβ data converged to similar quality parameters as the Mo Kα model, but only after the refinement of anomalous dispersion values for molybdenum.

Fig. 3.28 shows some details of the multipole refinements with both wavelengths. Despite of the reduced accessible resolution compared to Mo Kα, Cu Kβ provides good results. Multipole refinements were performed using the program `MoPro`[77] and subsequently analysed with `MoProViewer`[85] and `VMoPro`.

In this refinement, one difficulty was to account for the anomalous dispersion for Ni in the model relying on Cu Kβ radiation, since the absorption edge of nickel (8,333 eV) is close to the emission energy of Cu Kβ radiation (8,906 eV). The program `MoPro` is also capable of dispersion refinement and the refined dispersion parameters were compared to the ones obtained from the same data but from a HAR model using `NoSpherA2`[41] in `olex2.refine`.[71]

The multipole model resulted in $f' = -1.732$ and $f'' = 3.388$ whearas the HAR

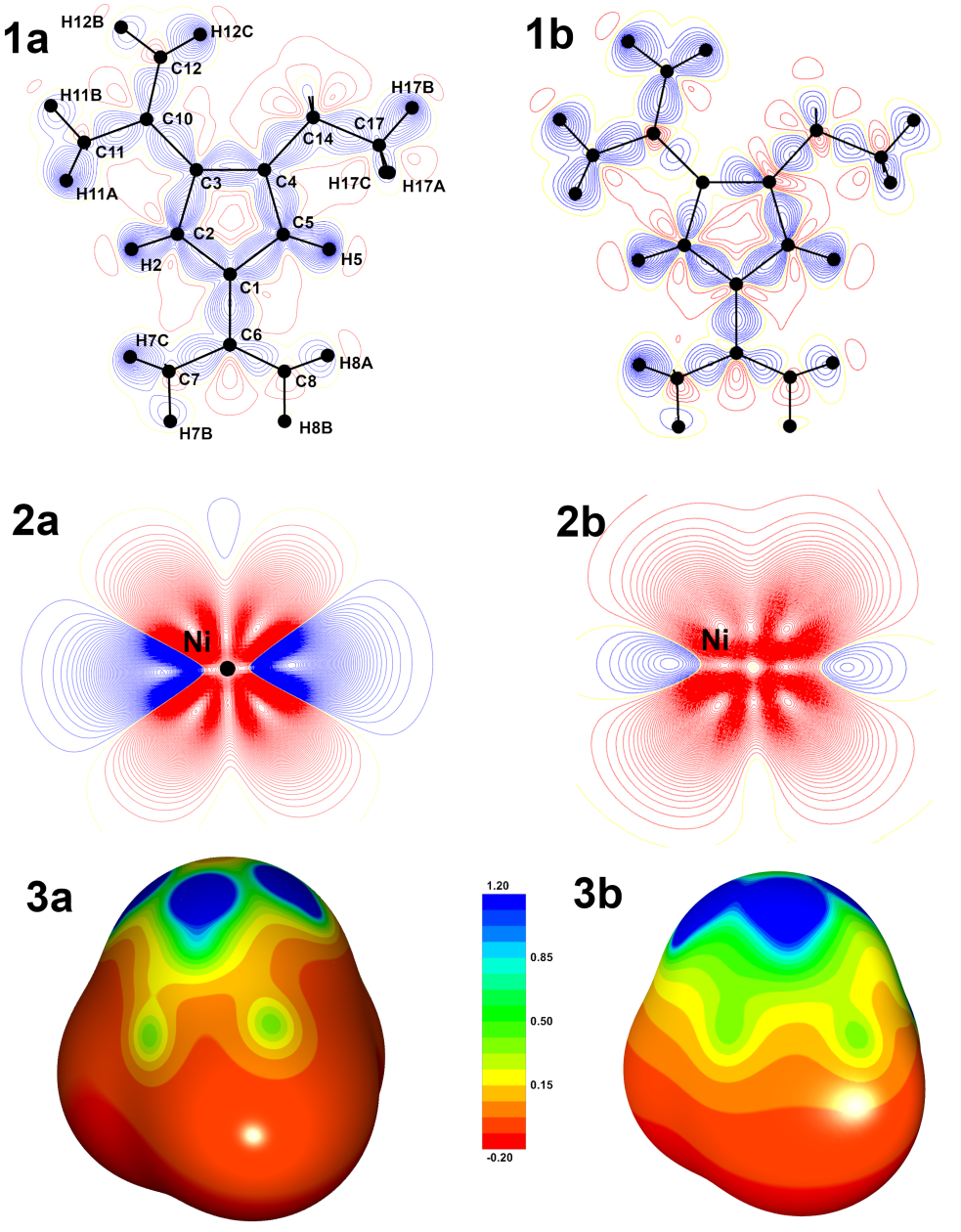

Figure 3.28: Results of the multipole refinement of Cp‴NiP_3 using Mo Kα (**a**) or Cu Kβ (**b**) radiation. **1** shows the deformation density distribution for the Cp‴–ligand. **2** shows the deformation density of the Ni–atom, both with 0.05 e lines. **3** shows the electrostatic potential distribution at 0.05 eÅ^{-3} density iso-surface for the NiP_3 fragment.[84]

model gave $f' = -1.820$ and $f'' = 3.614$. Tabulated values according to Sasaki are $f' = -1.885$ and $f'' = 3.481$.

This good agreement shows that dispersion refinement cannot be used to compensate for possible deficiencies in a high parametric model like the multipole model and still shows reasonable values in this refinement.

4

Conclusion and Outlook

In a total of 26 different synchrotron diffraction measurements on two different compounds, spectral features, such as the exact energies of K absorption (pre-)edges, were determined exclusively from diffraction data. These features are otherwise only accessible through X-ray absorption spectroscopy and give insight into a variety of electronic properties. The values above the absorption edge closely reproduced the oscillations found in the spectral fine structure. For the compound $Mo(CO)_6$, the crystallographic model featuring refined anomalous dispersion parameters provides consistently low R-factors. This proves a stable, good fit between measured and modelled data regardless of the excitation energy. The models based on tabulated dispersion values performed significantly worse and had clearly recognisable artefacts in the residual electron density maps.

Hence, the refinement of the dispersion parameters compensates the problems encountered in crystallographic models near an absorption edge when tabulated values were used. The models based on refined parameters had less residual density and greatly improved bond precision. Despite radiation damage occurring during the measurements of $(MeCN)_3Mo(CO)_3$, the overall trend of the anomalous dispersion parameters still agreed very well with the absorption spectrum.

The method was evaluated with respect to correlations in the least-squares refinement, the resolution dependence and the reproducibility over different mea-

surement setups. Apart from the expected closely related atomic parameters of molybdenum, no additional correlations for the dispersion correction were found. Neither the choice of crystallographic model (IAM or HAR) nor the resolution limit of the data influences the general trend of the refined parameters. However, they did influence the absolute values. In general, f' is more susceptible than f''. Despite a different detector setup, temperature and operating mode of the synchrotron, the values for $Mo(CO)_6$ determined during two separate visits to the ESRF proved to be very similar.

In contrast, a multipole model obtained from data of $Mo(CO)_6$ at the exact K absorption edge of molybdenum showed significantly deviating dispersion values especially in the case of f'. In the multipole model, however, significantly more parameters are refined, some of which also strongly modify the electron density in the vicinity of the molybdenum atom and can thus also affect the dispersion parameters. At least the f'' value determined from the multipole model agreed with that obtained from HAR. In contrast, a comparison using the example of the complex Cp‴NiP3, which was measured with a laboratory diffractometer with Cu Kβ radiation near the nickel K absorption edge, again shows good agreement between the refined dispersion values of MM and HAR. This allows the assumption that the refinement of the anomalous dispersion in the multipole model is also meaningful and reliable, provided that one does not measure exactly at the absorption edge.

A demonstration with deliberately incorrect atomic models showed that assigning a wrong element with an electron number in the range of the correct dispersion correction can give better quality parameters than the true element. Subsequent refinement of the dispersion parameters of false atom types masks differences in atomic form factor even more and leads to even better R-factors. In particular, using tabulated dispersion values in the IAM at 20,001 eV, the hypothetical compound "$Cu(CO)_6$" (R_1 = 1.86 %, wR_2 = 5.37 %) showed significantly better quality indicators in contrast to the real $Mo(CO)_6$ (R_1 = 2.36 %, wR_2 = 6.90 %). However, the best model was still obtained for the correct atom type if HAR and dispersion refinement are combined. In practical application, such a wrong element assignment is highly unlikely. After all, one knows the elements used and the scattering values would only be refined if the radiation energy used is in the range of the absorption edge of an element.

In the exemplary application of dispersion refinement to measurements at a single wavelength carried out with a laboratory diffractometer, it was shown that the new method can provide insights into the electronic differences of similar com-

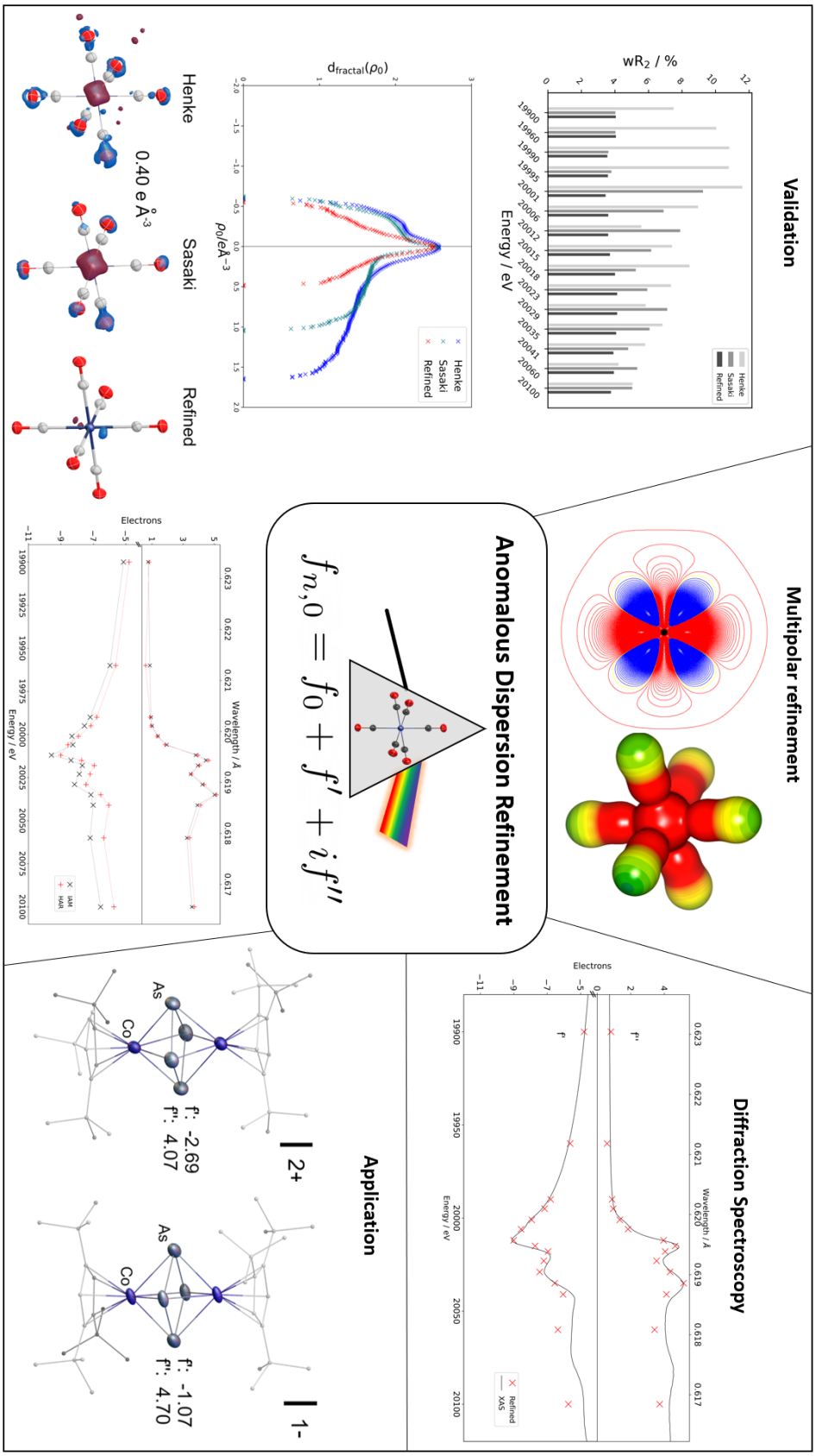

Figure 4.1: Graphical conclusion

pounds. Differently charged cobalt-containing organometallic complexes measured with copper Kα radiation also gave very different dispersion parameters, although the cobalt K absorption edge is a full 332 eV below the copper Kα emission energy. While the two dications $(Cp'''Co)_2E_4^{2+}$ (E = P, As) resulted in similar values for cobalt (P: $f' = -2.52$, $f'' = 4.03$; As: $f' = -2.69$, $f'' = 4.07$), quite different parameters were obtained for the monoanion $(Cp'''Co)_2As_4^-$ ($f' = -1.07$, $f'' = 4.70$). In this context an important aspect of laboratory diffractometers is the application of combined K$\alpha_{1,2}$ radiation with two distinct energies and therefore two different dispersion correction values. The conventional method uses a weighted average of the two energies, which is also used for the dispersion correction based on tabulated data. Depending on the anode material, the Kα energies are 20 (Cu), 105 (Mo) or even 173 eV (Ag) apart, which should be considered especially in the vicinity of an absorption edge.

The presented results show that the refinement of anomalous dispersion parameters offers several opportunities and advantages for X-ray crystallography. The method extends the scope of information obtained by diffraction experiments to the range that was previously only accessible to spectroscopy. Theoretical calculation of X-ray absorption spectra and fitting to support points can potentially provide the entire absorption information of a compound with data of only a few measurement energies. With a variety of differently available X-ray sources, this is even conceivable for laboratory diffractometers, so that X-ray absorption spectroscopy could become widely accessible without synchrotron radiation.

List of Figures

5 Appendices

5.1 Appendix A - Crystallographic data

The crystallographic information files (.cifs) are available at `https://www.dropbox.com/sh/j5ugjsacw5r7nle/AACgRLJns30CCF7GXRXKKVfya?dl=0`.

5.1.1 $Mo(CO)_6$

Energy / eV	19900			19900		
Wavelength / Å	0.62303			0.62116		
Empirical formula	MoC6O6			MoC6O6		
Formula weight / g mol^{-1}	263.995			263.995		
Crystal size / mm-3	0.1×0.1×0.1			0.1×0.1×0.1		
Temperature / K	100			100		
a / Å	11.7186(2)			11.7667(1)		
b / Å	11.2061(1)			11.2494(1)		
c / Å	6.3367(1)			6.36557(1)		
$\alpha = \beta = \gamma$ / °	90			90		
V / $Å^{-3}$	832.13(2)			842.744(12)		
ρ / g cm^{-3}	2.107			2.107		
μ / mm^{-1}	1.092			1.093		
θ-range / °	3.05 – 30.16			3.34 – 30.03		
Total reflections	45893			45893		
Unique reflections	1899			1899		
$I/\sigma(I)$	45.25			46.10		
Indices range	-24 ≤ h ≤ 24			-24 ≤ h ≤ 24		
	-23 ≤ k ≤ 23			-23 ≤ k ≤ 23		
	-13 ≤ l ≤ 13			-13 ≤ l ≤ 13		
Completeness	1.00000			1.00000		
Disp. Source	**Henke**	**Sasaki**	**Refined**	**Henke**	**Sasaki**	**Refined**
R_1, wR_2, Rint / %	2.51, 7.50, 8.11	1.64, 4.01, 8.11	1.63, 4.05, 8.11	3.02, 10.03, 6.96	1.58, 4.03, 6.96	1.56, 4.11, 6.96
GooF	1.013	1.024	1.038	1.009	1.011	1.017
Largest peak, hole / e $Å^{-3}$	0.5435, -0.5955	0.3456, -0.3186	0.3501, -3.223	0.9596, -0.6906	0.5021, -0.3929	0.6434, -0.4300
No. of restraints	0	0	0	0	0	0
No. of parameters	68	68	70	68	68	70
f' / electrons	-8.2545	-4.7345	-4.7953	-10.2529	-5.6236	-5.6236
f" / electrons	0.5562	0.5414	0.8154	0.5532	0.5384	0.5840
C-O bond prec. / Å	0.0016	0.0009	0.0007	0.0021	0.0009	0.0008

Energy / eV	19990			19995		
Wavelength / Å	0.62023			0.62007		
Empirical formula	MoC6O6			MoC6O6		
Formula weight / g mol^{-1}	263.995			263.995		
Crystal size / mm-3	0.1×0.1×0.1			0.1×0.1×0.1		
Temperature / K	100			100		
a / Å	11.7573(1)			11.7667(1)		
b / Å	11.2432(1)			11.2494(1)		
c / Å	6.3650(2)			6.36557(1)		
$\alpha = \beta = \gamma$ / °	90			90		
V / $Å^{-3}$	841.382(15)			842.744(12)		
ρ / g cm^{-3}	2.107			2.107		
μ / mm^{-1}	1.436			1.431		
θ-range / °	3.03 – 30.01			3.32 – 30.00		
Total reflections	48742			48659		
Unique reflections	4281			4290		
$I/\sigma(I)$	60.5			77.50		
Indices range	-24 ≤ h ≤ 24 -23 ≤ k ≤ 23 -13 ≤ l ≤ 13			-24 ≤ h ≤ 24 -23 ≤ k ≤ 23 -13 ≤ l ≤ 13		
Completeness	0.99260			1.00000		
Disp. Source	**Henke**	**Sasaki**	**Refined**	**Henke**	**Sasaki**	**Refined**
R_1, wR_2, Rint / %	3.03, 10.81, 5.49	1.39, -3.61, 5.49	1.34, 3.47, 5.49	3.05, 10.78, 4.12	1.46, 3.79, 4,12	1.40, 3.58, 4.12
GooF	1.039	1.090	1.065	1.060	1.031	1.047
Largest peak, hole / e $Å^{-3}$	1.0387, -06655	0.3068, -0.3291	0.2827, -0.3939	1.0595, -0.6471	0.4141, -0.3342	0.4038, -0.4316
No. of restraints	0	0	0	0	0	0
No. of parameters	68	68	70	68	68	70
f' / electrons	-11.2513	-6.9563	-6.7919	-11.4234	-7.6468	-7.1552
f" / electrons	0.5517	0.5369	0.8814	0.5514	0.5366	0.9514
C-O bond prec. / Å	0.0021	0.0008	0.0007	0.0020	0.0009	0.0007

Energy / eV	20001			20006		
Wavelength / Å	0.61988			0.61973		
Empirical formula	MoC6O6			MoC6O6		
Formula weight / g mol^{-1}	263.995			263.995		
Crystal size / mm-3	0.1×0.1×0.1			0.1×0.1×0.1		
Temperature / K	100			100		
a / Å	11.8030(2)			11.8071(2)		
b / Å	11.2897(1)			11.2936(2)		
c / Å	6.3952(7)			6.3976(1)		
$\alpha = \beta = \gamma$ / °	90			90		
V / $Å^{-3}$	852.184(18)			853.08(2)		
ρ / g cm^{-3}	2.107			2.107		
μ / mm^{-1}	8.121			8.106		
θ-range / °	3.31 – 29.98			3.32 – 30.00		
Total reflections	48654			48805		
Unique reflections	4313			4325		
$I/\sigma(I)$	86.20			73.00		
Indices range	-24 ≤ h ≤ 24			-24 ≤ h ≤ 24		
	-23 ≤ k ≤ 23			-23 ≤ k ≤ 23		
	-13 ≤ l ≤ 13			-13 ≤ l ≤ 13		
Completeness	1.00000			1.00000		
Disp. Source	**Henke**	**Sasaki**	**Refined**	**Henke**	**Sasaki**	**Refined**
R_1, wR_2, Rint / %	3.79, 11.51, 2.74	2.71, 9.25, 2.74	1.28, 3.44, 2.74	3.12, 8.88, 2.92	2.01, 6.79, 2.92	1.32, 3.60, 2.92
GooF	1.030	1.024	1.113	1.028	0.912	1.115
Largest peak, hole / e $Å^{-3}$	1.1577, -0.5444	0.8860, -0.5100	0.3361, -0.5311	0.7441, -0.4726	0.6318, -0.2348	0.4359, -0.3486
No. of restraints	0	0	0	0	0	0
No. of parameters	68	68	70	68	68	70
f' / electrons	-11.4284	-11.1028	-7.921	11.0489	-7.6834	-8.5661
f" / electrons	3.7149	1.168	1.3418	3.7135	3.6936	1.8348
C-O bond prec. / Å	0.0035	0.0018	0.0009	0.0025	0.0015	0.0009

Energy / eV	20012			20015		
Wavelength / Å	0.61954			0.61945		
Empirical formula	MoC6O6			MoC6O6		
Formula weight / g mol^{-1}	263.995			263.995		
Crystal size / mm-3	0.1×0.1×0.1			0.1×0.1×0.1		
Temperature / K	100			100		
a / Å	11.8133(2)			11.8175(2)		
b / Å	11.2989(2)			11.3017(2)		
c / Å	6.4015(1)			6.4038(1)		
$\alpha = \beta = \gamma$ / °	90			90		
V / $Å^{-3}$	852.184(18)			855.27(3)		
ρ / g cm^{-3}	2.107			2.107		
μ / mm^{-1}	8.068			8.054		
θ-range / °	3.30 – 29.96			3.30 – 29.97		
Total reflections	48675			48894		
Unique reflections	4319			4322		
$I/\sigma(I)$	50.80			44.20		
Indices range	-24 ≤ h ≤ 24			-24 ≤ h ≤ 24		
	-23 ≤ k ≤ 23			-23 ≤ k ≤ 23		
	-13 ≤ l ≤ 13			-13 ≤ l ≤ 13		
Completeness	1.00000			1.00000		
Disp. Source	**Henke**	**Sasaki**	**Refined**	**Henke**	**Sasaki**	**Refined**
R_1, wR_2, Rint / %	1.94, 5.48, 3.56	2.39, 7.72, 3.56	1.32, 3.54, 3.56	2.47, 7.25, 4.01	2.01, 6.00, 4.01	1.40, 3.70, 4.01
GooF	1.015	0.872	1.080	1.039	0.872	1.056
Largest peak, hole / e $Å^{-3}$	0.5150, -0.3156	0.6414, -0.5038	0.4779, -0.3806	0.7637, -0.4687	0.8167, -0.2780	0.6475, -0.3027
No. of restraints	0	0	0	0	0	0
No. of parameters	68	68	70	68	68	70
f' / electrons	-10.5678	-6.8798	-9.0114	10.3399	6.6487	-7.7222
f" / electrons	3.7117	3.6915	3.9549	3.7108	3.6905	3.6440
C-O bond prec. / Å	0.0015	0.0016	0.0010	0.0021	0.0017	0.0012

Energy / eV	20018			20023		
Wavelength / Å	0.61936			0.61920		
Empirical formula	MoC6O6			MoC6O6		
Formula weight / g mol^{-1}	263.995			263.995		
Crystal size / mm-3	0.1×0.1×0.1			0.1×0.1×0.1		
Temperature / K	100			100		
a / Å	11.8197(2)			11.8161(2)		
b / Å	11.3029(2)			11.2986(2)		
c / Å	6.4043(1)			6.4031(1)		
$\alpha = \beta = \gamma$ / °	90			90		
V / $Å^{-3}$	855.60(3)			854.85(3)		
ρ / g cm^{-3}	2.107			2.107		
μ / mm^{-1}	8.045			8.028		
θ-range / °	3.30 – 29.96			3.30 – 29.95		
Total reflections	49111			49812		
Unique reflections	4326			4325		
$I/\sigma(I)$	43.30			46.30		
Indices range	-24 ≤ h ≤ 24			-24 ≤ h ≤ 24		
	-23 ≤ k ≤ 23			-23 ≤ k ≤ 23		
	-13 ≤ l ≤ 13			-13 ≤ l ≤ 13		
Completeness	1.00000			1.00000		
Disp. Source	**Henke**	**Sasaki**	**Refined**	**Henke**	**Sasaki**	**Refined**
R_1, wR_2, Rint / %	2.74, 8.26, 4.04	1.85, 5.06, 4.04	1.50, 4.00, 4.04	2,57, 7.18, 4.00	2.13, 5.72, 4.00	1.61, 4.05, 4.00
GooF	1.065	0.884	1.060	1.093	0.902	1.052
Largest peak, hole / e $Å^{-3}$	0.7745, -0.5403	0.6950, -0.2647	0.5774, -0.4803	0.8231, -0.4588	1.0216, -0.1916	0.7642, -0.3296
No. of restraints	0	0	0	0	0	0
No. of parameters	68	68	70	68	68	70
f' / electrons	10.1118	-6.4606	-6.9469	-9.7063	-6.1918	-7.1993
f" / electrons	3.7100	3.6895	4.0493	3.7085	3.6877	3.5400
C-O bond prec. / Å	0.0025	0.0015	0.0013	0.0024	0.0015	0.0013

Energy / eV	20029			20035		
Wavelength / Å	0.61902			0.61883		
Empirical formula	MoC6O6			MoC6O6		
Formula weight / g mol^{-1}	263.995			263.995		
Crystal size / mm-3	0.1×0.1×0.1			0.1×0.1×0.1		
Temperature / K	100			100		
a / Å	11.8119(3)			11.7284(3)		
b / Å	11.2943(3)			11.3077(3)		
c / Å	6.4016(2)			6.4081(2)		
$\alpha = \beta = \gamma$ / °	90			90		
V / $Å^{-3}$	854.01(4)			857.10(4)		
ρ / g cm^{-3}	2.107			2.107		
μ / mm^{-1}	8.029			7.989		
θ-range / °	3.30 – 29.94			3.29 – 29.93		
Total reflections	48788			48801		
Unique reflections	4328			4328		
$I/\sigma(I)$	37.30			33.20		
Indices range	-24 ≤ h ≤ 24			-24 ≤ h ≤ 24		
	-23 ≤ k ≤ 23			-23 ≤ k ≤ 23		
	-13 ≤ l ≤ 13			-13 ≤ l ≤ 13		
Completeness	1.00000			1.00000		
Disp. Source	**Henke**	**Sasaki**	**Refined**	**Henke**	**Sasaki**	**Refined**
R_1, wR_2, Rint / %	2.36, 5.67. 4.86	2.45, 6.87, 4.86	1.64, 4.02, 4.86	2.55, 6.64, 5.35	2.23, 5.85, 5.35	1.68, 3.98, 5.35
GooF	1.101	0.937	1.053	1.086	0.942	1.083
Largest peak, hole / e $Å^{-3}$	0.7962, -0.4489	1.000, -0.3667	0.7699, -0.3193	0.7275, -0.5010	0.7473, -0.4045	0.6644, -0.4040
No. of restraints	0	0	0	0	0	0
No. of parameters	68	68	70	68	68	70
f' / electrons	-9.2498	-5.9592	-7.4529	-8.7677	-5.7590	-6.548
f" / electrons	3.7068	3.6857	4.3409	3.7050	3.6836	5.1478
C-O bond prec. / Å	0.0021	0.0021	0.0014	0.0025	0.0024	0.0016

Energy / eV	20041			20060		
Wavelength / Å	0.61865			0.61806		
Empirical formula	MoC6O6			MoC6O6		
Formula weight / g mol^{-1}	263.995			263.995		
Crystal size / mm-3	0.1×0.1×0.1			0.1×0.1×0.1		
Temperature / K	100			100		
a / Å	11.7284(3)			11.8220(3)		
b / Å	11.3077(3)			11.3007(3)		
c / Å	6.4081(2)			6.4060(2)		
$\alpha = \beta = \gamma$ / °	90			90		
V / $Å^{-3}$	857.10(4)			855.82(4)		
ρ / g cm^{-3}	2.107			2.107		
μ / mm^{-1}	7.98			7.901		
θ-range / °	3.29 – 29.93			3.29 – 29.89		
Total reflections	40624			41356		
Unique reflections	3367			3389		
$I/\sigma(I)$	31.00			35.30		
Indices range	-24 ≤ h ≤ 24			-24 ≤ h ≤ 24		
	-23 ≤ k ≤ 23			-23 ≤ k ≤ 23		
	-13 ≤ l ≤ 13			-13 ≤ l ≤ 13		
Completeness	1.00000			1.00000		
Disp. Source	**Henke**	**Sasaki**	**Refined**	**Henke**	**Sasaki**	**Refined**
R_1, wR_2, Rint / %	2.15, 5.66, 5.67	1.68, 4.61, 5.67	1.60, 3.81, 5.67	1.55, 4.05, 4.91	1.71, 5.10, 4.91	1.52, 3.70, 4.91
GooF	1.145	0.903	1.067	0.920	0.866	1.070
Largest peak, hole / e $Å^{-3}$	0.8003, -0.4170	0.7549, -0.5938	0.7094, -0.6071	0.6763, -0.5300	0.7393, -0.5921	0.6248, -0.6216
No. of restraints	0	0	0	0	0	0
No. of parameters	68	68	70	68	68	70
f' / electrons	-8.3106	-5.5995	-6.0462	-6.8107	-5.2014	-6.3576
f" / electrons	3.7033	3.6816	4.1247	3.6977	3.675	3.4211
C-O bond prec. / Å	0.0024	0.0017	0.0016	0.0015	0.0017	0.0014

Energy / eV	20100		
Wavelength / Å	0.61683		
Empirical formula	MoC6O6		
Formula weight / g mol^{-1}	263.995		
Crystal size / mm-3	0.1×0.1×0.1		
Temperature / K	100		
a / Å	11.8412(2)		
b / Å	11.3231(2)		
c / Å	6.463(1)		
$\alpha = \beta = \gamma$ / °	90		
V / $Å^{-3}$	860.30(3)		
ρ / g cm^{-3}	2.107		
μ / mm^{-1}	7.874		
θ-range / °	3.28 – 29.83		
Total reflections	40494		
Unique reflections	3367		
$I/\sigma(I)$	31.60		
Indices range	$-24 \leq h \leq 24$		
	$-23 \leq k \leq 23$		
	$-13 \leq l \leq 13$		
Completeness	1.00000		
Disp. Source	**Henke**	**Sasaki**	**Refined**
R_1, wR_2, Rint / %	1.67, 4.72,3.79	1.51, 3.73, 3.79	1.51, 3.60, 3.79
GooF	0.869	1.119	1.060
Largest peak, hole / e $Å^{-3}$	0.7848, -0.4915	1.0564, -0.4988	0.6855, -0.5067
No. of restraints	0	0	0
No. of parameters	68	68	70
f' / electrons	-4.6374	-4.6704	-5.7302
f" / electrons	3.6862	3.6613	3.7231
C-O bond prec. / Å	0.0017	0.0016	0.0016

5.1.2 $(MeCN)_3Mo(CO)_3$

Energy / eV	19900			19960		
Wavelength / Å	0.62306			0.62131		
Empirical formula	C11H12MoN4O3			C11H12MoN4O3		
Formula weight / g mol^{-1}	344.174			344.174		
Crystal size / mm-3	0.1×0.1×0.1			0.1×0.1×0.1		
Temperature / K	100			100		
a / Å	8.1962(1)			8.2062(1)		
b / Å	12.6687(1)			12.6864(2)		
c / Å	14.6866(2)			14.7188(2)		
$\alpha = \beta = \gamma$ / °	90			90		
V / $Å^{-3}$	1524.99(1)			1532.32(1)		
ρ / g cm^{-3}	1.518			1.518		
μ / mm^{-1}	0.614			0.608		
θ-range / °	2.19 – 30.16			2.17 – 30.03		
Total reflections	86146			86883		
Unique reflections	7575			7650		
$I/\sigma(I)$	90.80			52.60		
Indices range	-17 ≤ h ≤ 17			-17 ≤ h ≤ 17		
	-26 ≤ k ≤ 26			-26 ≤ k ≤ 26		
	-30 ≤ l ≤ 30			-30 ≤ l ≤ 30		
Completeness	1.00000			1.00000		
Disp. Source	**Henke**	**Sasaki**	**Refined**	**Henke**	**Sasaki**	**Refined**
R_1, wR_2, Rint / %	3.10, 9.97, 3.70	2.22, 6.53, 3.94	2.06, 5.99, 3.94	4.28, 14.4, 4.14	2.85, 8.53, 4.14	2.80, 8.46, 4.14
GooF	1.023	0.950	1.075	1.082	1.031	1.102
Largest peak, hole / e $Å^{-3}$	0.955, -0.562	0.950, -0.343	0.913, -0.342	1.082, -0.707	1.130, -0.295	1.1024, -0.305
No. of restraints	0	0	0	0	0	0
No. of parameters	101	101	103	101	101	103
f' / electrons	-0.0841	-4.6863	-4.8746	-10.0922	-5.5124	-5.4602
f" / electrons	0.5564	0.5416	1.6744	0.5534	0.5386	1.6626
C-C bond prec. / Å	0.0027	0.0019	0.0017	0.0040	0.0023	0.0023

Energy / eV	19995			20001		
Wavelength / Å	0.62023			0.62004		
Empirical formula	C11H12MoN4O3			C11H12MoN4O3		
Formula weight / g mol^{-1}	344.174			344.174		
Crystal size / mm-3	0.1×0.1×0.1			0.1×0.1×0.1		
Temperature / K	100			100		
a / Å	8.2125(1)			8.1989(1)		
b / Å	12.6926(2)			12.6706(2)		
c / Å	14.7408(2)			14.7227(2)		
$\alpha = \beta = \gamma$ / °	90			90		
V / $Å^{-3}$	1536.54(4)			1529.46(3)		
ρ / g cm^{-3}	1.518			1.518		
μ / mm^{-1}	0.604			0.605		
θ-range / °	2.17 – 30 01			2.17 –30.00		
Total reflections	87945			87446		
Unique reflections	7717			7688		
$I/\sigma(I)$	39.50			35.20		
Indices range	-17 ≤ h ≤ 17			-17 ≤ h ≤ 17		
	-26 ≤ k ≤ 26			-26 ≤ k ≤ 26		
	-30 ≤ l ≤ 30			-30 ≤ l ≤ 30		
Completeness	1.00000			1.00000		
Disp. Source	**Henke**	**Sasaki**	**Refined**	**Henke**	**Sasaki**	**Refined**
R_1, wR_2, Rint / %	4.97, 16.9, 4.88	3.76, 11.1, 4.88	3.79, 11.1, 4.88	5.94, 19.3, 4.35	5.16, 14.8, 4.35	5.23, 14.3, 4.35
GooF	1.021	1.022	1.020	1.023	1.024	1.019
Largest peak, hole / e $Å^{-3}$	1.323, -0.662	1.331, -0.268	1.403, -0.248	1.649, -0.544	1.642, -0.292	1.875, -0.306
No. of restraints	0	0	0	0	0	0
No. of parameters	101	101	103	101	101	103
f' / electrons	-11.2513	-6.9563	-6.5922	-11.4557	-7.851	-6.8956
f" / electrons	0.5517	0.5369	1.8844	0.5514	0.5366	2.2772
C-C bond prec. / Å	0.0040	0.0027	0.0027	0.0047	0.0033	0.0027

Energy / eV	20005			20010		
Wavelength / Å	0.61992			0.61976		
Empirical formula	C11H12MoN4O3			C11H12MoN4O3		
Formula weight / g mol^{-1}	344.174			344.174		
Crystal size / mm-3	0.1×0.1×0.1			0.1×0.1×0.1		
Temperature / K	100			100		
a / Å	8.2110(1)			8.2253(1)		
b / Å	12.6889(2)			12.7043(3)		
c / Å	14.7513(3)			14.7804(3)		
$\alpha = \beta = \gamma$ / °	90			90		
V / $Å^{-3}$	1536.93(2)			1544.50(6)		
ρ / g cm^{-3}	1.518			1.518		
μ / mm^{-1}	3.395			3.382		
θ-range / °	2.16 – 29.99			2.16 – 29.99		
Total reflections	87786			88031		
Unique reflections	7737			7757		
$I/\sigma(I)$	32.20			25.60		
Indices range	-17 ≤ h ≤ 17			-17 ≤ h ≤ 17		
	-26 ≤ k ≤ 26			-26 ≤ k ≤ 26		
	-30 ≤ l ≤ 30			-30 ≤ l ≤ 30		
Completeness	1.00000			1.00000		
Disp. Source	**Henke**	**Sasaki**	**Refined**	**Henke**	**Sasaki**	**Refined**
R_1, wR_2, Rint / %	7.63, 22.4, 5.17	7.68, 22.6, 5.17	7.30, 18.6, 5.17	7.25, 19.6, 6.67	7.67, 17.8, 6.67	6.94, 17.1, 6.67
GooF	1.021	0.991	1.021	1.006	0.975	0.957
Largest peak, hole / e $Å^{-3}$	2.789, -0.454	2.294, -0.467	2.808, -0.350	2.618, -0.398	2.878, -0.350	2.430, -0.509
No. of restraints	0	0	0	0	0	0
No. of parameters	101	101	103	101	101	103
f' / electrons	-11.5296	-11.0911	-7.4302	-11.1248	-7.8970	-7.7210
f" / electrons	3.7152	0.5364	3.0935	3.7137	3.6940	3.6910
C-C bond prec. / Å	0.0060	0.0050	0.0043	0.0050	0.0043	0.0040

Energy / eV	20014			20018		
Wavelength / Å	0.61964					
Empirical formula	C11H12MoN4O3			C11H12MoN4O3		
Formula weight / g mol^{-1}	344.174			344.174		
Crystal size / mm-3	0.1×0.1×0.1			0.1×0.1×0.1		
Temperature / K	100			100		
a / Å	8.2166(2)			8.2261(2)		
b / Å	12.6893(3)			12.7042(3)		
c / Å	14.7692(4)			14.7906(4)		
$\alpha = \beta = \gamma$ / °	90			90		
V / $Å^{-3}$	1539.87(6)			1545.71(4)		
ρ / g cm^{-3}	1.518			1.518		
μ / mm^{-1}	3.386			3.372		
θ-range / °	2.16 – 29.98			2.16 – 29.97		
Total reflections	88209			88228		
Unique reflections	7756			7763		
$I/\sigma(I)$	19.80			17.20		
Indices range	-17 ≤ h ≤ 17			-17 ≤ h ≤ 17		
	-26 ≤ k ≤ 26			-26 ≤ k ≤ 26		
	-30 ≤ l ≤ 30			-30 ≤ l ≤ 30		
Completeness	1.00000			1.00000		
Disp. Source	**Henke**	**Sasaki**	**Refined**	**Henke**	**Sasaki**	**Refined**
R_1, wR_2, Rint / %	7.52, 19.6, 8.81	7.71, 18.6, 8.81	7.68, 18.3, 8.81	7.48, 19.8, 10.37		7.29, 17.2, 10.4
GooF	1.013	0.994	1.008	1.025		0.991
Largest peak, hole / e $Å^{-3}$	2.461, -0.444	2.837, -0.437	3.007, -0.436	2.45, -0.564		2.820, -0.448
No. of restraints	0	0	0	0	0	0
No. of parameters	101	101	103	101	101	103
f' / electrons				-10.4918	-6.7918	-6.5528
f" / electrons				3.7114	3.6912	4.8360
C-C bond prec. / Å	0.0053	0.0050	0.0050	0.0067		0.0050

Energy / eV	20022			20040		
Wavelength / Å	0.61939			0.61883		
Empirical formula	C11H12MoN4O3			C11H12MoN4O3		
Formula weight / g mol^{-1}	344.174			344.174		
Crystal size / mm-3	0.1×0.1×0.1			0.1×0.1×0.1		
Temperature / K	100			100		
a / Å	8.2279(1)			8.2417(2)		
b / Å	12.7075(3)			12.7242(3)		
c / Å	14.7997(4)			14.8279(4)		
$\alpha = \beta = \gamma$ / °	90			90		
V / $Å^{-3}$	1547.41(6)			1554.99(7)		
ρ / g cm^{-3}	1.518			1.518		
μ / mm^{-1}	3.368			3.335		
θ-range / °	2.16 – 29.97			2.15 – 29.93		
Total reflections	88042			88266		
Unique reflections	7767			7802		
$I/\sigma(I)$	15.90			18.00		
Indices range	-17 ≤ h ≤ 17			-17 ≤ h ≤ 17		
	-26 ≤ k ≤ 26			-26 ≤ k ≤ 26		
	-30 ≤ l ≤ 30			-30 ≤ l ≤ 30		
Completeness	1.00000			0.99800		
Disp. Source	**Henke**	**Sasaki**	**Refined**	**Henke**	**Sasaki**	**Refined**
R_1, wR_2, Rint / %	7.48, 20.2, 11.6	7.35, 18.0, 11.6	7.38, 17.8, 11.6	9.69, 24.7, 13.9	9.78, 24.3, 13.9	8.99, 22.9, 13.9
GooF	1.027	1.001	0.998	1.047	1.043	1.053
Largest peak, hole / e $Å^{-3}$	2.432, -0.549	2.811, -0.479	2.918, -0.484	2.734, -0.917	3.045, 1.082	2.730, -1.324
No. of restraints	0	0	0	0	0	0
No. of parameters	101	101	103	101	101	103
f' / electrons	-10.1879	-6.5164	-6.1970	-8.7677	-5.7590	-6.1066
f" / electrons	3.7103	3.6899	4.3297	3.7050	3.6836	6.5533
C-C bond prec. / Å	0.0050	0.0067	0.0067	0.0103	0.0100	0.0097

Energy / eV	20100		
Wavelength / Å	0.61698		
Empirical formula	C11H12MoN4O3		
Formula weight / g mol^{-1}	344.174		
Crystal size / mm-3	0.1×0.1×0.1		
Temperature / K	100		
a / Å	8.2616(2)		
b / Å	12.7575(3)		
c / Å	14.8690(4)		
$\alpha = \beta = \gamma$ / °	90		
V / $Å^{-3}$	1567.16(6)		
ρ / g cm^{-3}	1.518		
μ / mm^{-1}	3.265		
θ-range / °	2.14 – 29.82		
Total reflections	89120		
Unique reflections	7862		
$I/\sigma(I)$	9.70		
Indices range	-17 ≤ h ≤ 17		
	-26 ≤ k ≤ 26		
	-30 ≤ l ≤ 30		
Completeness	1.00000		
Disp. Source	**Henke**	**Sasaki**	**Refined**
R_1, wR_2, Rint / %	7.94, 22.4, 19.8	7.94, 19.4, 19.8	7.92, 19.0, 19.8
GooF	1.005	1.004	0.997
Largest peak, hole / e $Å^{-3}$	2.847, -0.587	2.840, -0.583	3.008, -0.603
No. of restraints	0	0	0
No. of parameters	101	101	103
f' / electrons	-4.6620	-4.7225	-4.3255
f" / electrons	3.6876	3.6630	4.9886
C-C bond prec. / Å	0.0077	0.0077	0.0077

5.2 Appendix B - Code

Several scripts were created to enable the evaluation of over a TB of data. The primary data procession was conducted using the `SNBL tool box`[68] and `CrysalisPro` [69]. For further processing, a python module within the crystallographic program suite `Olex2`[42] was created. This module took an initial structure solution for a molecule and subsequently refined it against various datasets of reflections (.hkl files) at various energies and created three crystallographic models, each with a different source of dispersion parameters (Henke[54], Sasaki[53] and refined[71]). The dispersion parameters as well as quality parameters were then extracted by the module and stored in a .csv file. The code to this module can be found here: `https://github.com/FlorianMeurer/masterthesis`.

Bibliography

[1] W. C. Röntgen *Science*, vol. 3, no. 59, pp. 227–231, 1896.

[2] Bragg, W. H. and Bragg, W. L. *Proc. R. Soc. Lond. A*, p. 428–438, 1913.

[3] W. Friedrich, P. Knipping, and M. Laue *Ann. d. Phys.*, vol. 346, no. 10, pp. 971–988, 1913.

[4] A. M. Glazer, "Crystallography: A Very Short Introduction," 2016.

[5] G. Friedel *Comptes Rendus*, vol. 157, pp. 1533–1536, 1913.

[6] D. Coster, K. S. Knol, and J. A. Prins *Z. f. Phys.*, vol. 63, p. 345, 1930.

[7] J. M. Bijvoet *Proc. Kon. Ned. Akad. Wet*, vol. 52, p. 313, 1949.

[8] A. F. Peerdeman, A. J. von Bommen, and J. M. Bijvoet *Nature*, vol. 165, p. 271, 1951.

[9] J. M. Bijvoet *Nature*, vol. 173, p. 888, 1954.

[10] H. D. Flack *Acta Cryst. A*, vol. 39, no. 6, pp. 876–881, 1983.

[11] G. N. Ramachandran and S. Parthasarathy *Science*, vol. 150, no. 3693, pp. 212–214, 1965.

[12] G. N. Ramachandran and S. Raman *Acta Cryst. A*, vol. 12, no. 12, pp. 957–964, 1959.

[13] R. Pepinsky and Y. Okaya *PNAS*, vol. 42, no. 5, pp. 286–292, 1956.

[14] S. Caticha-Ellis *Acta Crystallographica*, vol. 15, no. 9, pp. 863–865, 1962.

[15] Y. Okaya and R. Pepinsky *Phys. Rev.*, vol. 103, pp. 1645–1647, 1956.

[16] D. H. Templeton and L. K. Templeton *Acta Cryst. A*, vol. 47, no. 4, pp. 414–420, 1991.

[17] A. P. Wilkinson, L. K. Templeton, and D. H. Templeton *J. Solid State Chem.*, vol. 118, no. 2, pp. 383–388, 1995.

[18] O. Einsle, S. L. A. Andrade, H. Dobbek, J. Meyer, and D. C. Rees *JACS*, vol. 129, no. 8, pp. 2210–2211, 2007.

[19] T. Spatzal, J. Schlesier, E. M. Burger, D. Sippel, L. Zhang, S. Andrade, D. Rees, and O. Einsle *Nat. Commun.*, vol. 10902, no. 7, 2016.

[20] D. Liberman, J. T. Waber, and D. T. Cromer *Phys. Rev.*, vol. 137, pp. A27–A34, 1965.

[21] W. Miller, *A Treatise on Crystallography.* Deighton, 1839.

[22] P. Coppens, "The structure factor," in *International Tables for Crystallography*, pp. 10–24, International Union of Crystallography, 2006.

[23] P. Coppens in *International Tables for Crystallography*, vol. III, International Union of Crystallography, 1952.

[24] J. M. Robertson *Nature*, vol. 138, no. 3493, pp. 627–627, 1936.

[25] C. Giacovazzo, "Direct methods," in *International Tables for Crystallography*, pp. 215–243, International Union of Crystallography, 2010.

[26] M. M. Woolfson *Rep. Prog. Phys.*, vol. 34, no. 2, pp. 369–434, 1971.

[27] A. H. Compton *Nature*, vol. 95, pp. 343–344, 1915.

[28] Wilson, A. C. J., *International Tables for Crystallography, Vol. C.* Dordrecht: Kluwer Academic Publishers, 1992.

[29] P. J. Brown, A. G. Fox, E. N. Maslen, M. A. O'Keefe, and B. T. M. Willis, "Intensity of diffracted intensities," in *International Tables for Crystallography*, pp. 554–595, International Union of Crystallography, 2006.

[30] B. Guillot, C. Jelsch, and P. Macchi, "10 multipole modeling with MoPro and XD," in *Complementary Bonding Analysis*, pp. 235–268, De Gruyter, 2021.

[31] N. K. Hansen and P. Coppens *Acta Cryst. A*, vol. 34, no. 6, pp. 909–921, 1978.

[32] F. Kleemiss, *Development of Quantum-Crystallographic Methods for Chemical and Biochemical Applications.* PhD thesis, 2021.

[33] D. Jayatilaka and B. Dittrich *Acta Cryst. A*, vol. 64, no. 3, pp. 383–393, 2008.

[34] J. Lübben, C. M. Wandtke, C. B. Hübschle, M. Ruf, G. M. Sheldrick, and B. Dittrich *Acta Cryst. A*, vol. 75, no. 1, pp. 50–62, 2019.

[35] D. R. Hartree *Math. Proc. Camb. Philos. Soc.*, vol. 24, no. 1, pp. 89–110, 1928.

[36] V. Fock, "Naeherungsmethode zur loeung des quantenmechanischen mehrkoerperproblems," *Zeit. f. Phys.*, vol. 61, no. 1-2, pp. 126–148, 1930.

[37] W. Kohn and L. J. Sham *Phys. Rev.*, vol. 140, pp. A1133–A1138, 1965.

[38] Szabo, A. and Ostlund, N. S. , *Modern quantum chemistry: Introduction to advanced electronic structure theory.* Dover Publications, 1996.

[39] F. L. Hirshfeld *Theor. Chim. Acta*, vol. 44, pp. 129–138, 1977.

[40] S. C. Capelli, H. Bürgi, B. Dittrich, S. Grabowsky, and D. Jayatilaka *IUCrJ*, vol. 1, no. 5, pp. 361–379, 2014.

[41] F. Kleemiss, O. V. Dolomanov, M. Bodensteiner, N. Peyerimhoff, L. Midgley, L. J. Bourhis, A. Genoni, L. A. Malaspina, D. Jayatilaka, J. L. Spencer, F. White, B. Grundkötter-Stock, S. Steinhauer, D. Lentz, H. Puschmann, and S. Grabowsky *Chem. Sci.*, vol. 12, pp. 1675–1692, 2021.

[42] O. V. Dolomanov, L. J. Bourhis, R. J. Gildea, J. A. K. Howard, and H. Puschmann vol. 42, no. 2, pp. 339–341, 2009.

[43] A. C. Thompson, J. Kirz, D. T. Attwood, E. M. Gullikson, M. R. Howells, J. B. Kortright, Y. Liu and A. L. Robinson, *X-ray Data Booklet, third Edition.* California: Lawrence Berkeley National Laboratory, 2009.

[44] Caticha-Ellis, S., *Anomalous Dispersion of X-rays in Crystallography.* 1981.

[45] James, R. W., *The optical principles of the diffraction of x-rays.* Ithaca, N.Y., Cornell University Press, 1965.

[46] R. L. Kronig *J. Opt. Soc. Am.*, vol. 12, no. 6, pp. 547–557, 1926.

[47] Hönl, H. *Ann. d. Phys.*, vol. 625, 1933.

[48] Hönl, H. *Zeit. f. Phys.*, vol. 11, 1933.

[49] H. Eisenlohr and G. L. J. Mueller *Zeit. f. Phys.*, vol. 136, 1954.

[50] Parratt, L. G. and Hempstead, C. F. *Phys. Rev.*, vol. 1593, 1954.

[51] Cromer, D. T. and Libermann, D. *J. Chem. Phys.*, vol. 1891, 1970.

[52] S. Brennan and P. L. Cowan *Rev. Sci. Instrum.*, vol. 63, no. 1, pp. 850–853, 1992.

[53] S. Sasaki *KEK–88-14*, 1989.

[54] B. Henke, E. Gullikson, and J. Davis *At. Data Nucl. Data*, vol. 54, no. 2, pp. 181–342, 1993.

[55] Creagh, D.C. and McAuley, W. *Int. Tab. Vol. C*, p. 206–222, 1992.

[56] P. Fornasini, "Introduction to x-ray absorption spectroscopy," 2015.

[57] J. Evans, *X-ray absorption spectroscopy for the chemical and materials sciences*. Nashville, TN: Wiley, 2017.

[58] A. Kramida, Y. Ralchenko, J. Reader, and and NIST ASD Team. NIST Atomic Spectra Database (ver. 5.9), [Online]. Available: `https://physics.nist.gov/asd` [2022, February 19]. National Institute of Standards and Technology, Gaithersburg, MD., 2021.

[59] M. Wang and Z. Feng *Curr. Opin. Electrochem.*, vol. 30, p. 100803, 2021.

[60] F. A. Lima, R. Bjornsson, T. Weyhermüller, P. Chandrasekaran, P. Glatzel, F. Neese, and S. DeBeer *Phys. Chem. Chem. Phys.*, vol. 15, pp. 20911–20920, 2013.

[61] Bunker, G., *Introduction to XAFS: A Practical Guide to X-ray Absorption Fine Structure Spectroscopy*. Cambridge University Press, 2010.

[62] Einstein, A. *Ann. d. Phys.*, vol. 322, no. 6, pp. 132–148, 1905.

[63] A. C. Scheinost, J. Claussner, J. Exner, M. Feig, S. Findeisen, C. Hennig, K. O. Kvashnina, D. Naudet, D. Prieur, A. Rossberg, M. Schmidt, C. Qiu, P. Colomp, C. Cohen, E. Dettona, V. Dyadkin, and T. Stumpf *J. Synchrotron Radiat.*, vol. 28, no. 1, pp. 333–349, 2021.

[64] C. Elschenbroich, *Organometallchemie.* Berlin Heidelberg New York: Springer-Verlag, 2009.

[65] K. Shimizu, H. Maeshima, H. Yoshida, A. Satsuma, and T. Hattori *Phys. Chem. Chem. Phys.*, vol. 3, pp. 862–866, 2001.

[66] Guss, J. M. and Merritt, E. A. and Phizackerley, R. P. and Hedman, B. and Muratam, M. and Hodgson, K. O. and Freeman, H. C. *Science*, vol. 241, no. 4867, pp. 806–811, 1988.

[67] Watts, B. *Opt. Express*, vol. 22, no. 19, pp. 23628–23639, 2014.

[68] V. Dyadkin, P. Pattison, V. Dmitriev, and D. Chernyshov *J. Synchrotron Radiat.*, vol. 23, no. 3, pp. 825–829, 2016.

[69] Rigaku Oxford Diffraction, "CrysAlisPro," 2022.

[70] G. M. Sheldrick *Acta Cryst. A*, vol. 71, no. 1, pp. 3–8, 2015.

[71] L. J. Bourhis, O. V. Dolomanov, R. J. Gildea, J. A. K. Howard, and H. Puschmann *Acta Cryst. A*, vol. 71, no. 1, pp. 59–75, 2015.

[72] M. Day, T. Trnka, and R. Grubbs, "Ccdc 191387: Experimental crystal structure determination," 2005.

[73] K. Meindl and J. Henn *Acta Cryts. A*, vol. 64, no. 3, pp. 404–418, 2008.

[74] F. Meurer, O. V. Dolomanov, C. Hennig, N. Peyerimhoff, F. Kleemiss, H. Puschmann, and M. Bodensteiner, "Refinement of dispersion correction parameters in single-crystal structure determinations," *submitted.*

[75] C. H. Sala, F. Belaj, and N. C. Mösch-Zanetti, 2018.

[76] F. L. Hirshfeld *Acta Cryst. A*, vol. 32, no. 2, pp. 239–244, 1976.

[77] C. Jelsch, B. Guillot, A. Lagoutte, and C. Lecomte *J. Appl. Cryst.*, vol. 38, no. 1, p. 38–54, 2005.

[78] S. C. Abrahams and E. T. Keve *Acta Cryst. A*, vol. 27, no. 2, pp. 157–165, 1971.

[79] R. David, *CRC Handbook of Chemistry and Physics*. Lide, 2010.

[80] W. Tang, E. Sanville, and G. Henkelman *J. Condens. Matter Phys.*, vol. 21, no. 8, p. 084204, 2009.

[81] S. D. Darren and M. Newville, "Xraydb," 2019.

[82] M. Piesch, C. Graßl, and M. Scheer *Angewandte Chemie International Edition*, vol. 59, no. 18, pp. 7154–7160, 2020.

[83] F. Meurer, V. Vukovic, C. Riesinger, and M. Bodensteiner, "Multipole studies using both Mo Kα and Cu Kβ radiation on Cp´´´NiP_3," *in preparation*.

[84] V. Vedran, *Calculs électrostatiques rapides dans l'analyse énergétique : Développement de la méthode, applications aux études de cristaux organiques et organométalliques et de complexes protéine/ligand*. PhD thesis, 2021.

[85] B. Guillot, E. Enrique, L. Huder, and C. Jelsch *Acta Cryst. A*, vol. 70, no. a1, p. C279–C279, 2014.

Erklärung

Ich bestätige, dass ich die Arbeit selbstständig verfasst und keine anderen als die von mir angegebenen Quellen und Hilfsmittel benutzt und die Arbeit nicht bereits an einer anderen Hochschule zur Erlangung eines akademischen Grades eingereicht habe. Ich bestätige außerdem, dass ich von den in §25 Abs. 6 vorgesehenen Rechtsfolgen Kenntnis habe.

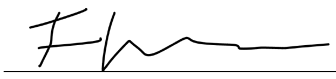

Florian Meurer